Effect of Thermal and Mechanical Loadings on the Degradation and Failure Modes of APS TBCs

Von der Fakultät für Georessourcen und Materialtechnik der
Rheinisch -Westfälischen Technischen Hochschule Aachen

zur Erlangung des akademischen Grades eines

Doktors der Ingenieurwissenschaften

genehmigte Dissertation

vorgelegt von

Dipl. –Ing. Olena Trunova

aus Kiew, Ukraine

Berichter: **Univ.-Prof. Jochen M. Schneider, Ph.D.**
Univ.-Prof. Dr.-Ing. Lorenz Singheiser

Tag der mündlichen Prüfung: 20.03.2006

Kurzfassung

Wärmedämmschichten werden als Schutz für thermisch hoch belastete Gasturbinenkomponenten eingesetzt. Dabei dienen sie zur Steigerung der Lebensdauer oder zur Verbesserung des thermischen Wirkungsgrads, der nur durch eine deutlich höhere Prozesstemperatur erreicht wird. Die Lebensdauer der beschichteten Komponenten hängt entscheidend vom Haftvermögen der keramischen Wärmedämmschicht ab. Platzt diese ab, ändern sich Eigenschaften der Oberfläche und die Ermüdungsfestigkeit singt. Das Versagen der Wärmedämmschicht hängt von einer ganzen Reihe von Prozessen und Parametern ab, wie beispielweise die Bond Coat Oxidation, Sintern der Keramikschicht, die Rauigkeit der Metall/Keramikgrenzfläche, Unterschiede in den thermischen Ausdehnungskoeffizienten der einzelnen Schichten sowie Kriech- und Relaxationsverhalten der Komponenten.
Die vorliegende Arbeit konzentriert sich daher auf Untersuchungen zur Korrelation zwischen Belastung und Art des Versagens sowie der Lebensdauer von beschichteten Komponeneten für Hpchtemperaturanwendungen. Zusätlich werden Untersuchungen zur Ermittlung der Hauptmechanismen und Parameter, die die Lebensdauer der Wärmedämmschicht bestimmen, durchgeführt und die Kinetik des Schädigungsverlaufs bestimmt. Der untersuchte Werkstoffverbund besteht aus einem hochwarmfesten Grundwerkstoff aus CMSX-4, der mit einer Haftvermittlerschicht aus einer NiCoCrAlY-Legierung (Bond-Coat) versehen ist. Auf diesen Bond-Coat wird die eigentliche Wärmedämmschicht mittels atmosphärischem Plasmagespritzte (APS) aufgebracht und besteht aus teilstabilisiertem Zirkondioxid (ZrO_2-7-8wt.%Y_2O_3).
Zur Untersuchung der genannten Eigenschaften wurden sechs unterschiedliche Typen von Experimente durchgeführt: (i) isotherme Oxidation, (ii) thermische Zyklierung, (iii) zyklische Oxidation, (iv) Zyklische Oxidation mit Temperaturgradient, (v)Thermomechanische Ermüdung, (vi) Thermomechanische Ermüdung mit Haltezeit bei hohen Temperaturen. Diese sechs Belastungstypen resultieren aus Kombinationen der vier grundsätzlichen Belastungsarten: (i) isotherme Auslagerung, (ii) thermische Zyklierung, (iii) Zyklieren der mechanischen Last und (iv) Auslagerung im Temperaturgradienten. Das Versagen der Wärmedämmschichten resultiert aus Rissbildung in der Wärmedämmschicht, in der TGO oder am Interface zwischen Wärmedämmschicht un TGO. Jede der unterschiedlichen Belastungen beeinflusst die Standzeit oder die Anzahl der möglichen Belastungszyklen bis zum Versagen und führt zu einem speziellen Schädigungstypen, die sich durch Ort und Art des Rissverlaufs unterscheiden lassen. Zur Beschreibung des Schädigungsverlaufs wir in der vorliegenden Arbeit eine Darstellungsmöglichkeit entwickelt, die im folgenden als Schädigungs-Mapping bezeichnet wird.
Zusätlich wurden Verformungsmechanismen und die zugehörige Änderung der Mikrostruktur von keramischen Dämmschichten untersucht. Dazu wurden freistehende Wärmedämmschichten, die mittels Plasmagespritzten (APS) worden sind, verwendet. Die Untersuchungen zeigen, dass die aus den Druckbelastungen resultierenden Spannungsrelaxationen bei APS-Wärmedämmschichten zu hohen Kriechraten führen.

Entsprechende Mikrostrukturuntersuchungen zeigen, dass die makroskopischen Kriechverformungen sowohl Rissbildung als auch Volumenverformungen einschließen.

Abstract

Thermal barrier coatings (TBCs) are applied for the thermal protection of hot section components of gas turbines to improve their life-time or to raise the power and thermal efficiency of the gas turbine by increasing the turbine inlet temperature. TBCs limit the lifetime of the coated component either by spallation or by affecting the surface properties of the component and therefore the fatigue resistance. The respective failure is influenced by a series of degradation parameters and processes such as bond coat oxidation, sintering of the ceramic coating, β-depletion in the bond coat, roughness of the metal/ceramic interface, mismatch of thermal expansion of the coatings and resulting stresses, creep and stress relaxation processes and so forth. These parameters promote the particular damage and failure modes differently and therefore, changes in the complex load scenario during service affect the failure mode and the lifetime of coated components.

The present work thus focuses on the correlation between the load scenario or type of loads and the resulting damage, failure modes and lifetime. Moreover, the kinetics of damage evolution and the major mechanisms and parameters, which control the durability of TBCs were investigated. A TBC system investigated consisted of air plasma-sprayed partially stabilized zirconia (ZrO_2-7-8wt.%Y_2O_3) with a NiCoCrAlY bond coat onto a CMSX-4 substrate and was subjected to six types of tests: (i) isothermal furnace tests, (ii) thermal cycling, (iii) cyclic oxidation, (iv) cyclic oxidation with temperature gradient, (v) thermomechanical fatigue, (vi) thermomechanical fatigue with a dwell time at high temperature in order to systematically analyze the influence of the type of the load profile on the damage and failure mode of the TBC composite, as well as on the time and number of cycles to failure.

Analysis of the damage and failure modes of thermal barrier coatings was based on the representation of these six test types or load profiles as a combination of four basic load components such as isothermal exposure, thermal cycling, mechanical cycling and temperature gradient. The activation of each of these load components was found to have a strong influence on the time and number of cycles to failure and the damage and failure modes, which were distinguished by the particular crack paths on which spallation of the coating had occurred and which were more or less activated by the respective load components. The corresponding damage mapping has been developed and is presented in this thesis.

The deformation mechanisms and corresponding microstructural changes of the ceramic top coat were additionally investigated on free-standing plasma-sprayed TBCs. Compressive deformation experiments revealed high creep rates and therefore high stress relaxation rates for APS-TBCs. Respective microstructural investigations displayed that macroscopic creep deformation comprises crack related as well as bulk related deformation.

Table of contents

1 Introduction and problem definition

According to the Energy Information Administration (EIA) prognosis, the world net electricity consumption is expected to increase at an average annual rate of 2.3% over the next two decades [1].

Coal will remain the main fossil fuel of electricity generation while a rise in the use of natural gas is expected (Figure 1.1). Thus, gas turbines will account for an increasing fraction of the base-load and peak-load generating capacity. Gas-fired systems with combined-cycle gas turbines have efficiencies of up to 58-60% and natural gas is also seen as a much cleaner fuel than any other.

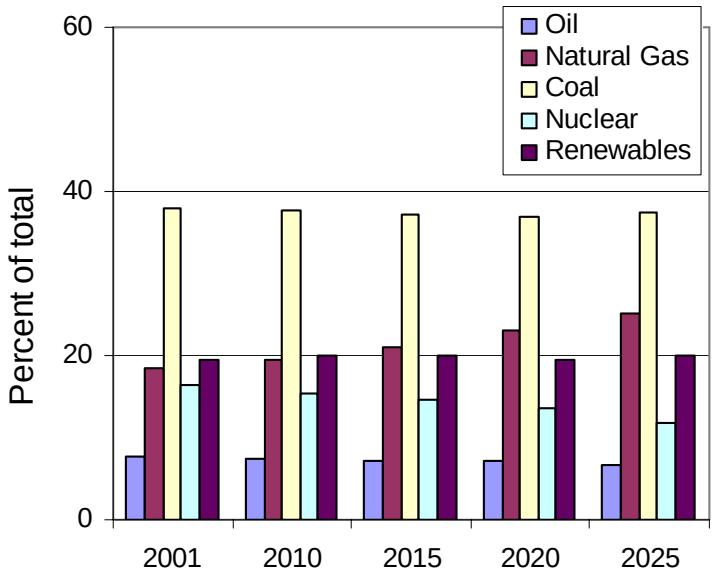

Figure 1.1 - Fuel shares of world electricity generation 2001-2005 [1]

Today, gas turbine alloys (Ni-base superalloys) are used for land-based gas turbines at temperatures up to 1000°C. Above this temperature, the superalloys have to be protected with thermal barrier coatings (TBCs) together with corrosion protective coatings, which increase their hot corrosion and oxidation resistance. Ceramic thermal barrier coatings (TBCs) are currently used on e.g. combustors, vanes and blades to provide thermal insulation as shown in Figure 1.2.

Two processes are used to apply thermal barrier coatings: air plasma spraying (APS) and electron beam physical vapor deposition (EB-PVD). Plasma spraying has been widely applied to produce TBCs on hot components like burner cans or combustion chambers. The EB-PVD process is particularly favoured for applications on more mechanically loaded parts, i.e. rotating parts like high-pressure turbine blades.

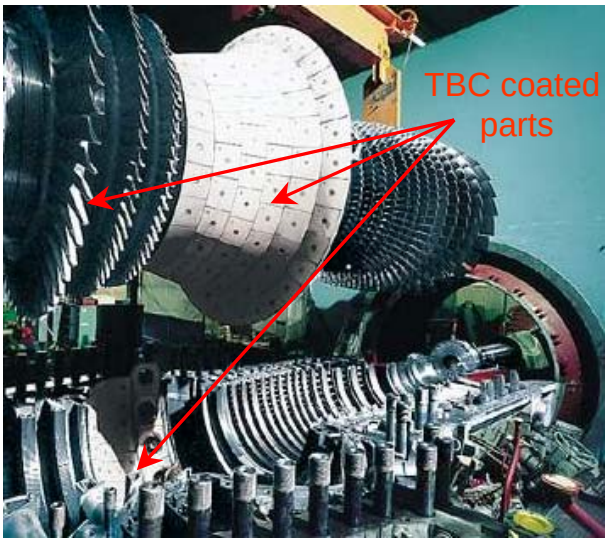

Figure 1.2 - Gas turbine with TBC coated parts

The highest thermal loads for materials in a turbine engine occur in the parts of combustion chamber and the first row of blades and vanes. The gas turbine inlet temperature (TIT) may reach 1350-1400°C in advanced turbine engines. Due to the special design of internal cooling and film cooling, reducing the temperature to below 1000°C at the superalloy surface is possible together with thermal barrier coatings (Figure 1.3). The temperature drops in proportion to the coating thickness, which is usually in the range from 50 to 300µm, and in inverse proportion to the thermal conductivity. Under service conditions, TBCs experience thermal and thermomechanical loadings, which lead to material degradation and spallation failure.

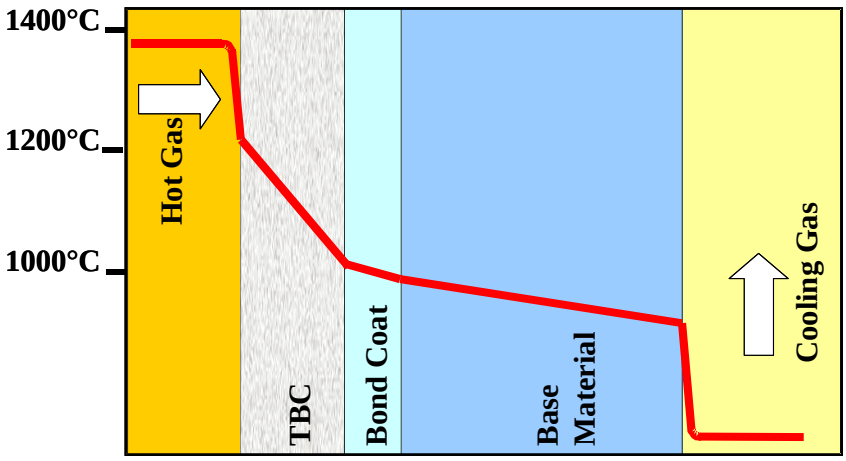

Figure 1.3 - Temperature gradients in TBC

There is significant potential for improving gas turbine power output and efficiency, as well as for reducing environmental emissions by increasing turbine inlet temperatures. However, it will be accompanied with further considerable increase of thermal and mechanical loads for the materials of hot gas components. In the course of this development, ceramic thermal barrier coatings will play an increasingly important role as an integral part of material designs. At the same time, the loss of coating can result in accelerated failure of the structural components due to increased alloy temperature, thus the development of prime reliant coatings is required. This must be accompanied with the development of lifetime models, which allow the reliable prediction of TBCs' durability.

TBC systems in service typically fail by spallation due to crack initiation and propagation at the TBC/BC interface region. In order to control and predict the service life of TBCs, the nature of the defects (cracks), their growth characteristic under thermal and thermomechanical loads and the underlying rate controlling mechanisms have to be comprehensively investigated.

The objective of the present work is to improve the understanding of APS TBC damage evolution and failure under different load profiles. Load profiles can be represented as a combination of four load components such as high temperature exposure, thermal cycling, mechanical cycling and temperature gradient. In the present investigation, the TBC system consisted of air plasma-sprayed partially stabilized zirconia (ZrO_2 - 7-8wt. %Y_2O_3) with a NiCoCrAlY bond coat onto CMSX-4 substrate which was subjected to the following load profiles (tests):

- one-component loading: isothermal oxidation and thermal cycling,
- two-component loading: cyclic oxidation (thermal exposure + thermal cycling) and thermomechanical fatigue (thermal cycling + mechanical cycling)
- three-component loading: cyclic oxidation with temperature gradient (thermal exposure + thermal cycling + thermal gradient) and TMF with dwell time (thermal cycling + mechanical cycling + temperature exposure)

The impact of respective load components on the activation of particular degradation mechanisms and failure modes, e.g. the crack propagation path, has been investigated and a respective map of crack paths and failure types has been developed.

Additionally damage behaviour and defect evolution in APS TBC systems were monitored using non-destructive methods such as acoustic emission and infrared thermography (thermal wave imaging).

In order to increase the experimental data basis and the understanding of deformation mechanisms and corresponding microstructural changes of plasma-sprayed TBCs, compressive deformation tests were carried out on a free-standing ZrO_2-7-8wt.%Y_2O_3 coatings together with extensive microstructural investigations.

2 Literature review

2.1 The thermal barrier coating system

Currently applied TBC composites consist of yttria partially stabilized zirconia ceramic topcoat and a metallic bond coat based either on MCrAlY-type compositions or on aluminides (simple or Pt-modified) deposited onto a superalloy substrate. Additionally, at high temperatures a thermally grown oxide scale (TGO) forms between the bond coat and the TBC [2,3,4,5,6].

To be effective, TBCs must exhibit low thermal conductivity and resist large thermally induced strains associated with thermal cycling. The porous and defect-rich microstructure of the TBC provides these highly desired properties [7].

Generally, two processes are used to apply thermal barrier coatings: air plasma spraying (APS) and electron beam physical vapor deposition (EB-PVD). The typical respective microstructures are shown in Figure 2.1.

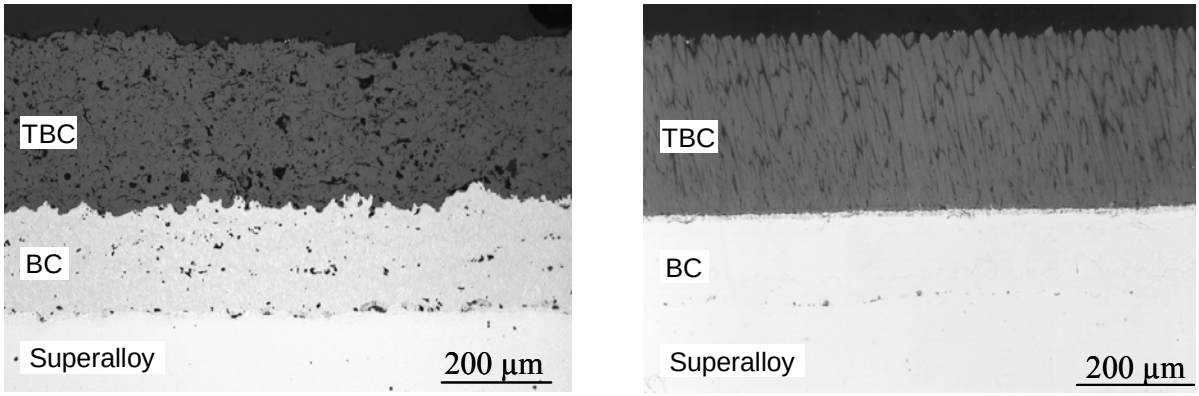

(a) (b)

Figure 2.1 – Typical microstructure of the TBC: a) APS, b) EB-PVD

A plasma-sprayed ceramic coating is built up by the successive impacts of semi-molten powder particles (splats) on a substrate. The structure and porosity of the resulting TBC depends mostly on particle velocity and temperature, which are controlled by spray parameters such as spraying distance and plasma power [8]. For crack network formation, substrate and coating temperatures during TBC deposition are of the great importance.

During EB-PVD processing, a high-energy electron beam melts and evaporates a ceramic source ingot in a vacuum chamber. The deposition conditions are designed to create a columnar grain structure with multiscale porosity that provides a good strain tolerance. The microstructure is mainly affected by such deposition parameters as substrate temperature, surface roughness, rotation rate of the component, and vapour flux from the evaporator [9].

The structure and properties of plasma-sprayed thermal barrier coatings will be reviewed in more detail.

2.1.1 Plasma-sprayed ceramic top coating

Zirconia is an outstanding material for thermal insulation because of its low thermal conductivity – around 2,5 W/mK for dense material and less than 1 W/mK for a plasma-sprayed coating. Another important property of the top coating material is the coefficient of thermal expansion (CTE). The CTE for the ceramic coating should be similar to that of the metallic substrate in order to decrease thermal stresses during thermal cycling. Zirconia has a relatively high coefficient of thermal expansion – about $10 \cdot 10^{-6}$ K^{-1} [10,11] – in comparison with other ceramic materials and is thus closer to the high metallic expansion coefficients.
Pure ZrO_2 exists in three crystallographic phases: a low-temperature monoclinic phase, an intermediate-temperature tetragonal phase, and a high-temperature cubic phase:

$$\text{monoclinic} \xleftrightarrow{1170°C} \text{tetragonal} \xleftrightarrow{2370°C} \text{cubic}$$

The tetragonal-to-monoclinic transformation is accompanied by significant volume expansion (approximately 3-5 vol.%) and can lead to cracking and failure of a TBC during thermal cycling. To suppress transformations the high-temperature phases of zirconia are stabilized by solid solution addition of one of several oxides (e.g. Y_2O_3, CeO_2, MgO). Currently used TBCs are partially stabilized zirconia (PSZ) with about 8 wt.% of yttria [7].
According to the equilibrium phase diagram [12] shown in Figure 2.2, the yttria partially stabilized zirconia (Y-PSZ) can be formed in range of 3-5 mol.% Y_2O_3 by diffusionless phase transformation from the high-temperature cubic phase to the metastable t′-phase due to rapid solidification during the plasma spray process. This phase differs from the low yttria tetragonal phase because it is stable with respect to the monoclinic transformation.

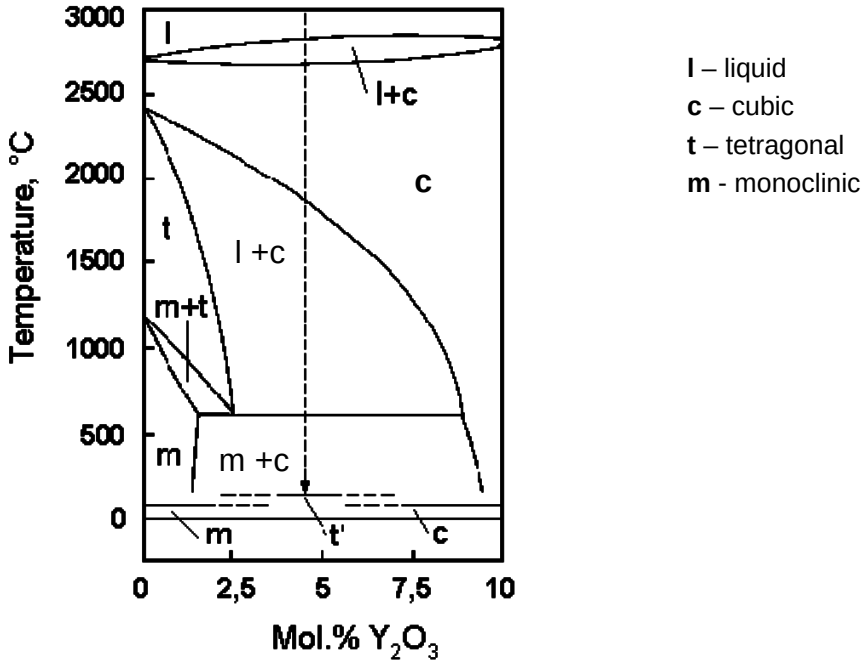

Figure 2.2 – Phase diagram of the ZrO_2 - Y_2O_3 system [12]

However, under high temperature exposure, the t´-phase is believed to decompose rather slowly to the equilibrium cubic and tetragonal phases, the last one transforming in the monoclinic phase during cooling to room temperature. This process strongly depends on temperature as well as on the cooling rate. Significant transformation of the tetragonal-to-monoclinic phase occurred after 400 hours of annealing. At 1400 °C the stability of the deposits was compromised after only 24 hours of annealing [13]. Thus the temperature limit for long-term use of yttria partially stabilized zirconia TBC is 1200°C.

A typical microstructure of APS TBCs [14] is shown in Figure 2.3. The coating consists of flat lamellar splats with lateral dimensions from 20µm to 100 µm and a thickness of about 10 µm. Cracks between splats (intersplat cracks) and pores can also be observed. Due to high cooling rates of deposited splats, tensile stresses arise within the splats and cause their segmentation, resulting in intergranular cracking (intrasplat cracks). Grains within splats are oriented parallel to the spray direction and have an elongated columnar shape. They can be characterised by an average diameter of roughly 0.5 µm and an aspect ratio of >10:1.

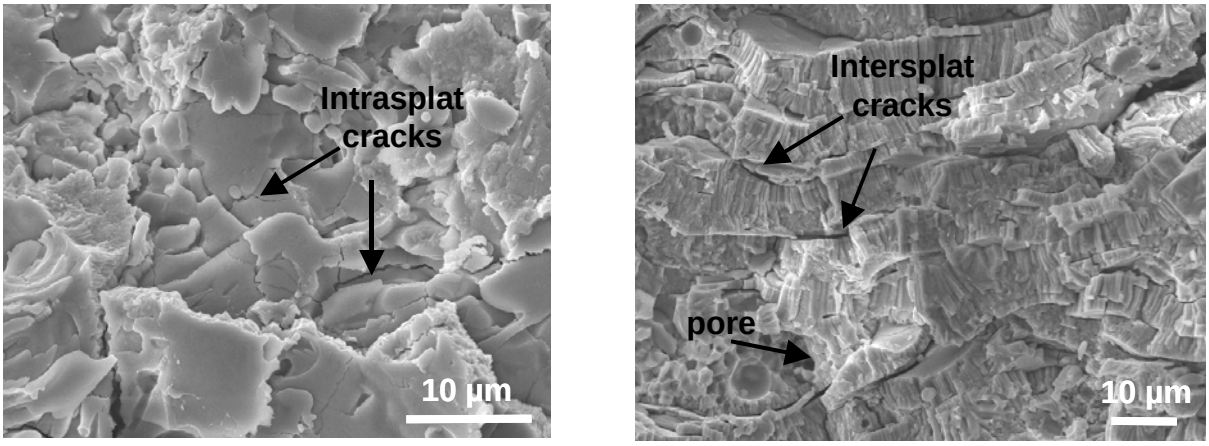

(a) (b)

Figure 2.3 – Fracture surface of APS YSZ: a) parallel to spraying splats, b) normal to spraying splats [14]

Small-angle neutron diffraction studies [15] have characterised the defect distributions in APS PSZ coatings and confirmed that both inter-splat pores and intra-splat microcracks are present in large numbers. Inter-splat cracks are oriented mostly parallel to the coating plane (perpendicular to the spray direction) whereas intra-splat cracks are oriented mainly perpendicular to the coating plane.

The degree of porosity as well as the size and orientation of cracks determines the physical and mechanical properties of plasma-sprayed coatings. For example, cracks parallel to the coating surface are responsible for the reduction of thermal diffusivity. The presence of defects also leads to the reduction of stiffness and an increase in strain tolerance [16].

In Figure 2.4 a selection of literature results with respect to the elastic modulus are displayed. These were determined by various mechanical elasticity measurements [17,18,19,20,21]. The data reveal the general trend of decreasing elastic modulus, or stiffness with increasing

porosity. A large scatter must be attributed to variations in the powder size, the spraying parameters and detailed defect structure, as well as to measuring techniques.

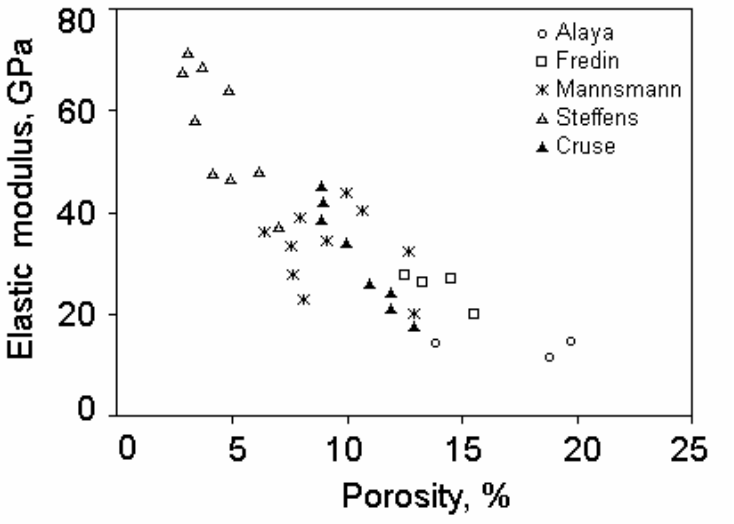

Figure 2.4 – Stiffness as a function of porosity [17,18,19,20,21]

The stiffness can be measured by a number of techniques, which are sensitive to global stiffness of the material (e.g. bending tests) or local stiffness (e.g. indentation methods). The stiffness values also depend on applied stresses (tensile, compressive), residual stresses (free-standing coating, bonded) and anisotropy of the spraying splats (normal / parallel to the spraying direction) [22,23,24].

In Figure 2.5, the temperature dependence of stiffness is represented [21,25,26,27]. All data are normalised to the respective values of as-sprayed material. As can be seen from Figure 2.5, the modulus values tend to decrease between room temperature and 1200°C by about 20-50%.

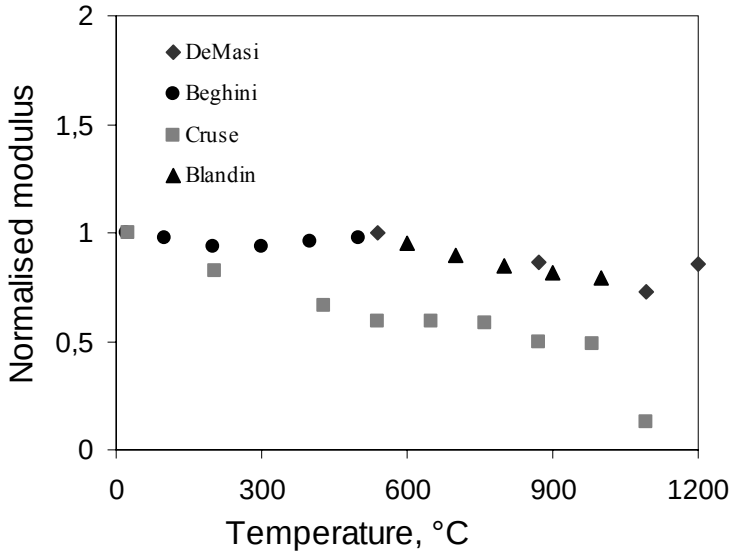

Figure 2.5 – Normalised stiffness as a function of temperature [21,25,26,27]

However, in gas turbines for energy applications the TBCs experience long exposure times at high temperatures, thus changes of stiffness during service become very important.
A continuous increase in stiffness has been observed above 1000°C by many investigators [28,29,30,31,32]. Underlying stiffening mechanisms are related to microstructural changes during heat exposure. The effect of heat treatment on the stiffness of APS zirconia is presented in Figure 2.6.

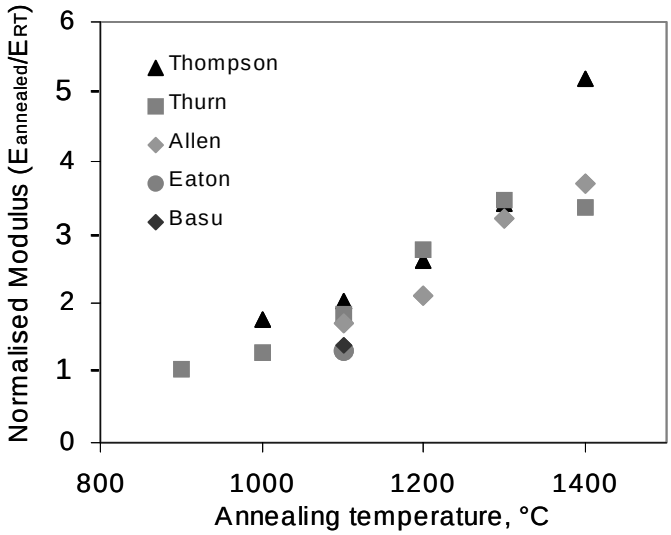

Figure 2.6 – Normalised stiffness as a function of annealing temperature [28,29,30,31,32] for exposure times up to 100 hours measured at room temperature

The two stages that can be distinguished in the stiffening process [33] are shown schematically in Figure 2.7. Above 1000°C grain growth and associated increase of microscopical material bonding occur across the splat boundaries, but the continued presence of microcracks ensures that stiffness remains relatively low. In contrast, samples aged at 1300°C show evidence of both increased intersplat bonding and microcrack healing due to sintering, which led to a fast and large increase in stiffness.

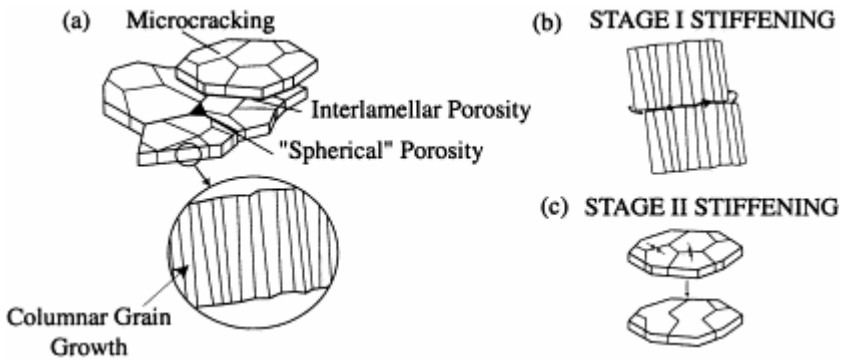

Figure 2.7 – Microstructural defects in plasma-sprayed coating (a) and two-stage stiffening during heat treatment (b, c) [33]

The time dependent properties of APS TBCs are complex and difficult to measure because of the porosity used to achieve strain tolerance. The primary creep stage is often observed for ceramic top coatings, with the strain rate continuously decreasing with time [34].
At lower temperatures, the relative boundary sliding of plasma-sprayed splats and grains, and the stress redistribution around the splats and microcracks are probably important mechanisms for ceramic creep deformation [35]. This stress dependent deformation will lead to coating shrinkage and thus stress relaxation at temperature under compressive stresses.
Under compressive deformation or compressive creep test, the plates are forced together, increasing the contact between plates temporarily. At high pressures and a temperature of 800°C, initial stage sintering occurs as a result of surface diffusion [36]. The increase in elastic modulus after compressive deformation as a function of temperature is shown in Figure 2.8.

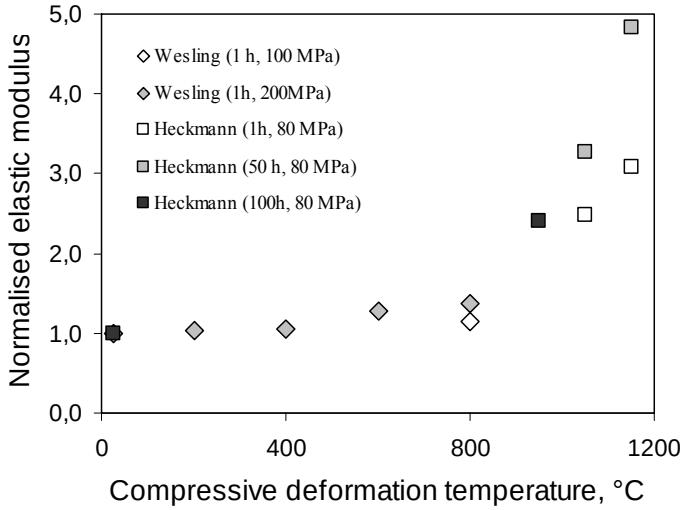

Figure 2.8 – Elastic moduli of TBC as a function of compressive deformation (permanent strain) at various temperatures [36,37]

At temperatures of 600° and 800°C, the elastic modulus significantly increases after 1 hour of 200 MPa compressive loading by 29% and 38%, respectively. The compressive stress of 100 MPa or greater must be applied at a temperature of 800°C for any significant increase in the subsequent room-temperature elastic modulus to occur. Compressive deformation in the temperature range of 950-1150°C leads to a much larger increase of elastic moduli [37].

2.1.2 Time dependent properties

Creep

The time dependent, nonrecoverable change in shape of materials due to an applied mechanical stress is called high temperature plasticity or creep. At high temperatures, plastic deformation can occur in the form of dislocation climb (dislocation creep), dynamic recrystallization and diffusion creep.
The effect of constant load σ on strain ε against time t is shown schematically in Figure 2.9.

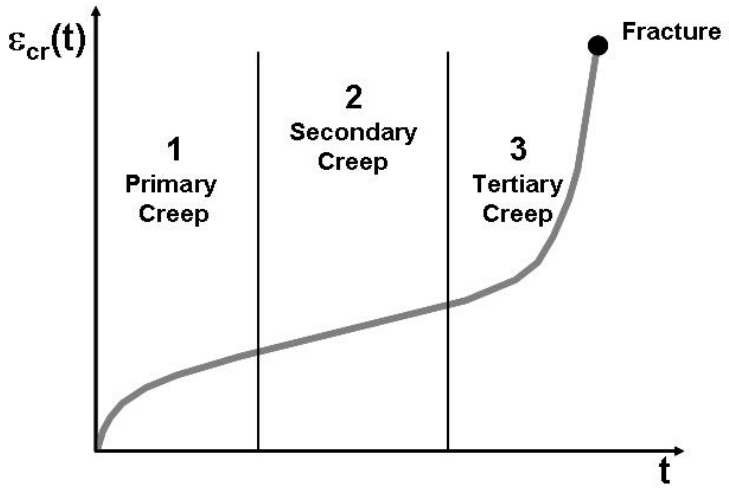

Figure 2.9 – Strain vs. time curve for a creep test

The initial strain $\varepsilon_i = \frac{\sigma_i}{E}$, is simply the elastic response to the applied load. The strain itself is usually calculated as the engineering strain, $\varepsilon = \frac{\Delta L}{L_0}$. The primary stage of the creep curve (1) is related to transient processes towards an equilibrium state of the microstructure and is often characterized by a decreasing creep strain rate ($\frac{d\varepsilon}{dt} = \dot{\varepsilon}$). The secondary stage (2) is characterized by a minimum and sometimes constant creep strain rate in which competing mechanisms of strain hardening and recovery may be present. The tertiary region (3) is characterized by an increasing creep strain rate in which necking or an increasing amount of micro damage occurs prior to failure of the material.

The diffusion creep may be controlled by lattice diffusion (Nabarro-Herring creep) or by grain boundary diffusion (Coble creep) depending on applied load, temperature and material grain size. The effect of increasing the temperature or increasing the stress is a raise in the levels and shapes of the strain time curves as shown in Figure 2.10.

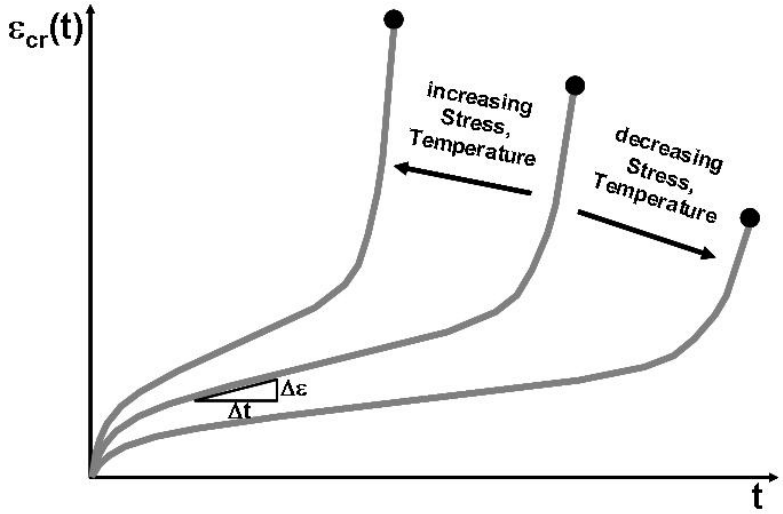

Figure 2.10 - Effect of stress and temperature on strain time creep curves

The strain rate in the secondary stage is the minimum strain rate, which is sometimes interpreted as steady state strain rate:

$$\dot{\varepsilon} = A_N \cdot \sigma^n \qquad \text{Eq. 2.1}$$

where n is the stress exponent, A_N is a temperature and structure dependent constant.

An Arrhenius-type rate model is frequently used to include the effect of temperature such as:

$$\dot{\varepsilon} = A \cdot \sigma^n \cdot e^{\left(-Q_c/RT\right)} \qquad \text{Eq. 2.2}$$

, where Qc is the activation energy for creep;

R is the universal gas constant and;

T is the absolute temperature.

Influence of temperature on creep rate is shown schematically in Figure 2.11.

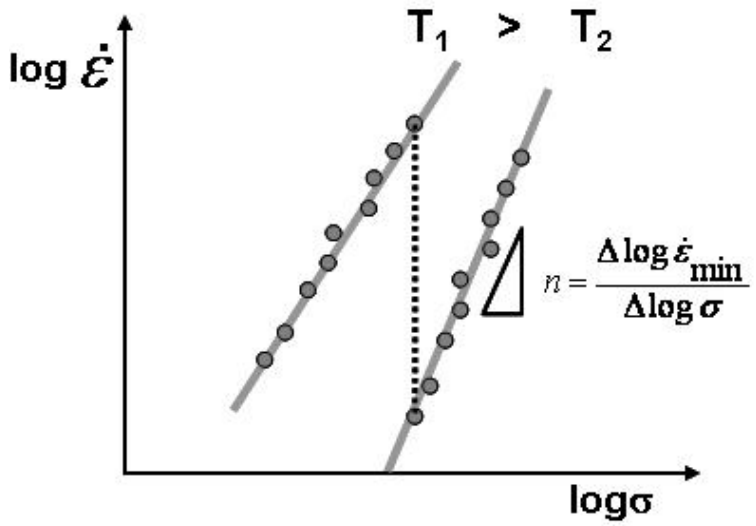

Figure 2.11 – Log-log plot of the minimum creep strain rate vs. stress as a function of temperature

Cyclic fatigue

Under cycling loading the fatigue damage evolution determines the fatigue life of the component. The fatigue process consists of (Figure 2.12):

- crack initiation;
- slip band crack growth (stage I crack propagation). These slip band cracks will grow in directions of maximum shear for only one or two grain diameters, when the crack begins growing in a direction of normal to maximum tensile stress;
- crack growth on planes of high tensile stresses (stage II crack propagation);
- ultimate failure (stage III).

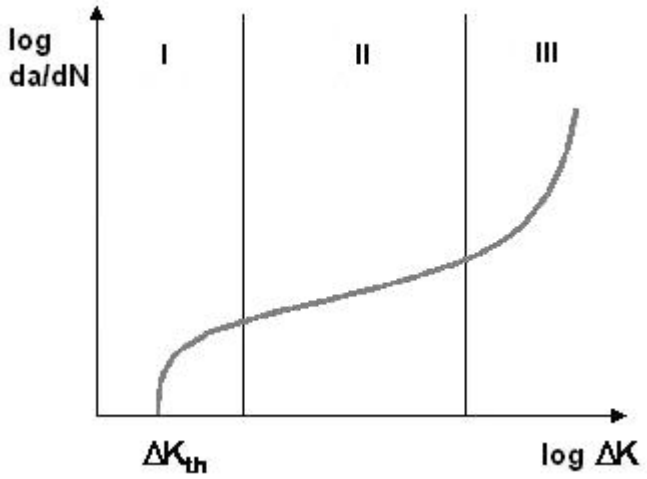

Figure 2.12 – The dependence of crack growth rate vs. stress intensity factor range

The crack formation begins frequently at a free surface, often at a point of high stress concentration. Once the crack is formed, it causes an area of even higher stress concentration (see also stress intensity factor), and it proceeds to propagate progressively with each application of load until the remaining stressed area finally becomes too small to support load statically and a sudden fracture results (Figure 2.13).

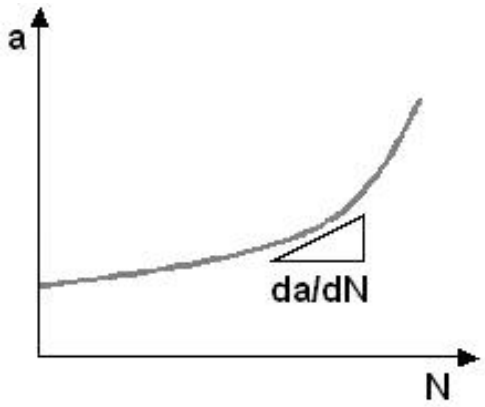

Figure 2.13 – The dependence of crack length vs. number of cycles

The mathematical description of the crack growth increase per load cycle vs. stress intensity factor is known as the Paris power law:

$$\frac{dA}{dN} = C(\Delta K)^m \qquad \text{Eq. 2.3}$$

, where

dA/dN is the crack propagation rate;

C and *n* are material constants**;**

$\Delta K = F(\Delta\sigma)\sqrt{\pi a}$, in which *F* is the geometry correction factor;

a is the crack length, and *C* and *m* are material costants.

There are three different crack modes: (i) opening mode, (ii) shearing mode and (iii) tearing mode with stress intensity factors K_I, K_{II} and K_{III}, respectively. Most cracks tend to propagate in opening mode under tensile stress.

2.1.3 MCrAlY-bond coat

The bond coat performs two main functions in a TBC system: (i) protection of base material from oxidation and corrosion attack during high temperature exposure and (ii) providing good adhesion to the ceramic top coat [38,39].

The presently applied bond coats for APS TBCs with typical composition MCrAlY (M=Ni, Co) form protective alumina scales under service conditions. Alumina is extremely stable at high temperatures, has a slow growth rate and adheres well to the bond coat. The main alloying element contents are in the range of 8-12% for Al, 15-22% for Cr and 10-30% for Co, whereas Y concentration is in the order of 0.2-0.5 wt.%. The addition of Y at low concentrations improves the adherence of the oxide scale [40].

The MCrAlY bond coats provide a rough surface for mechanical bonding of the ceramic top coat and for minimizing the effect of CTE mismatch between the substrate and ceramic top coat materials. The thermal expansion coefficient for bond coats is typically in the range of $14\text{-}16\times10^{-6}$/°C [39], similar to the superalloys.

Bond coats are frequently produced using vacuum or low pressure plasma spraying (VPS/LPPS), which allows more dense and more oxide free coatings (up to 99% dense) than air plasma spraying. The thickness of bond coat layers is typically between 50 and 300 μm, sometimes even more.

The microstructure and phase composition of NiCoCrAlY bond coats depend strongly on temperature, as shown in Figure 2.14. According to the ternary phase diagram of Ni-Cr-Al at 850°C, 3 phases may occur:

- the body-centred α-Cr phase;
- the ordered face-centred cubic β-NiAl phase with B2-structure;
- the face-centred cubic γ-Ni phase.

Additionally at 1000°C, the ordered intermetallic γ′-Ni_3Al phase with $L1_1$-structure may be present [41].

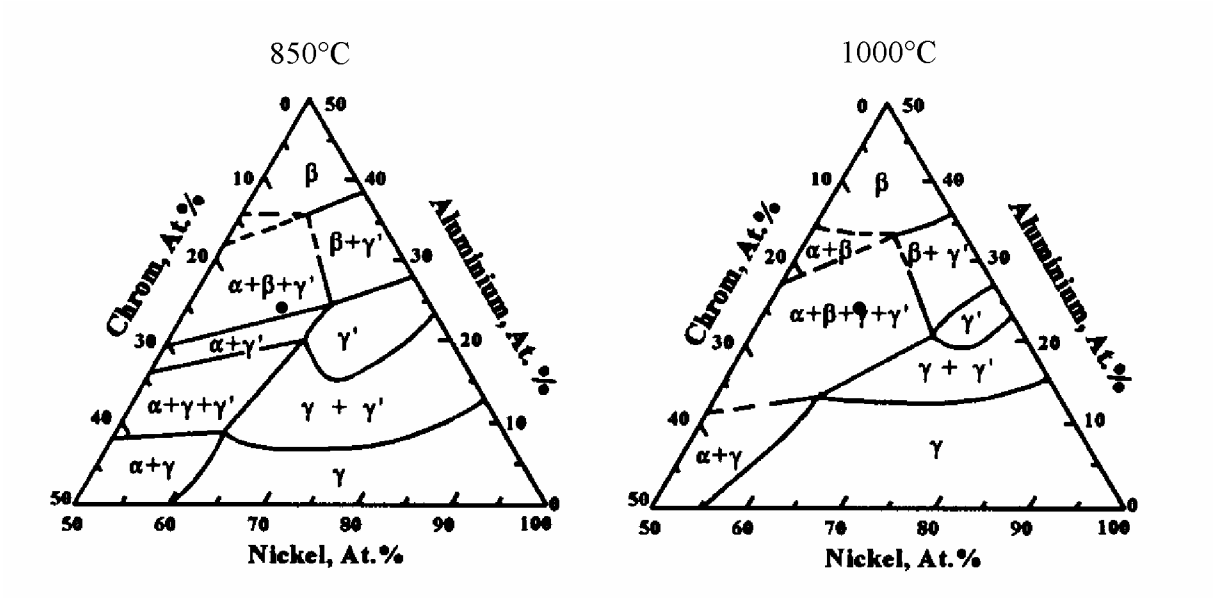

Figure 2.14 - Ni-Cr-Al tertiary phase diagrams for 850 and 1000°C [41]

Under service conditions in gas turbines at high temperatures, the microstructure of the MCrAlY bond coat is not stable (Figure 2.15). During thermal exposure, the β-NiAl transforms to γ because of the outward diffusion of aluminium, which forms Al_2O_3, as well as the interdiffusion between superalloy substrate and bond coat.

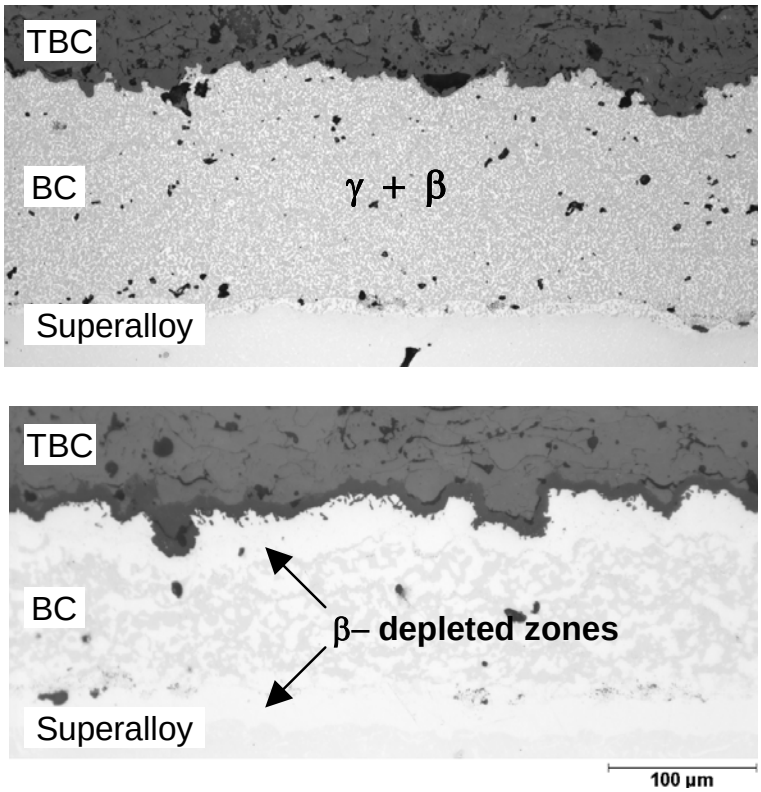

Figure 2.15 – Microstructure of the bond coat: a) as received and b) annealed at 1050°C for 670h

Two β-phase depletion zones develop, as illustrated in Fig. 2.14.b for a sample exposed for 670 h at 1050°C. One zone is located next to the TGO and the other adjacent to the substrate. For long exposure times the β-phase can disappear completely, leaving a single-phase γ-solid solution. The protective alumina scale can no longer be maintained and oxidation of other major alloying elements, i.e. Ni, Co, Cr occurs. Their oxides are not protective and rapid TBC spallation can result.

Other important factors for alumina scale adhesion are the mechanical properties of the bond coat. A weak material is better able to dissipate strain energy by plastic deformation and creep relaxation. The elastic properties between room temperature and 1000°C of three bond coat materials are shown in Figure 2.16.

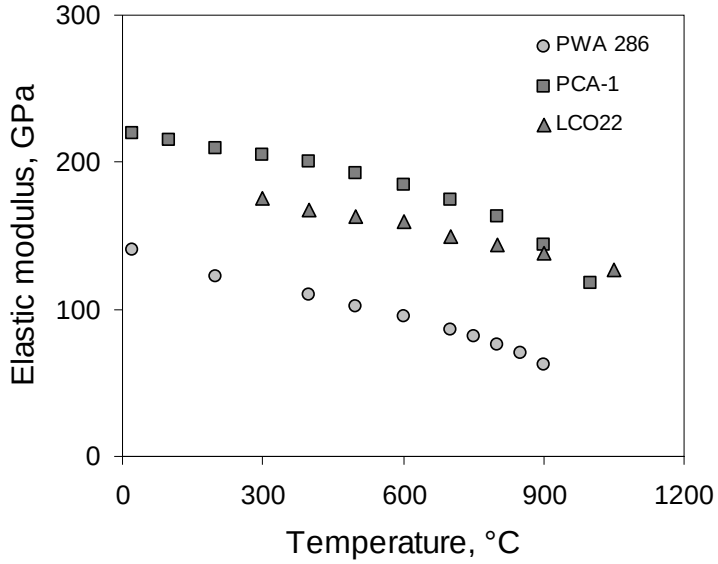

Figure 2.16 – Temperature dependence of elastic moduli for three MCrAlY bond coat alloys [42,43,44]

Many intermetallic phases show a distinct transition from a brittle to ductile behaviour as the temperature is increased. The change from brittle to ductile behaviour can occur gradually with increasing temperature or within a very limited temperature range of 100 C or less. In the latter case, a critical temperature, the brittle-to-ductile transition temperature (BDTT), can be defined. The BDTT is used to describe the ability of a coating to tolerate the strain [45,46,47]. It is affected by microstructure, composition of coating material and application process. The BDDT of MCrAlY is increased by increasing the Al content as shown in Figure 2.17 [45].

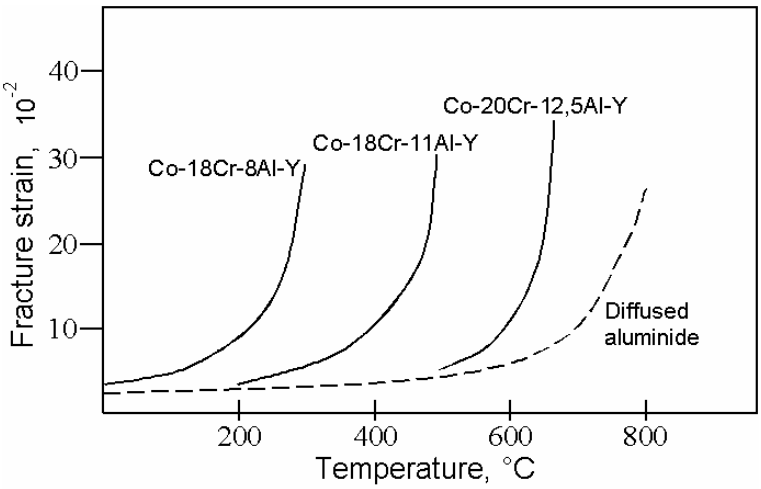

Figure 2.17 – Temperature dependence of strain to crack for several MCrAlY bond coat alloys [45]

Below the BDTT MCrAlY coatings exhibit high strength and low ductility, but above the BDTT the bond coat rapidly looses strength while the ductility increases dramatically, as it is shown in Figure 2.18 for a coating with 48.3% Ni, 20.3% Co, 17.3% Cr, 13.6% Al and 0.5 Y (PWA 276). At low temperatures the tensile elongation of coating material is about 0.5%. It increases sharply above about 520°C and becomes superplastic at higher temperatures [46].

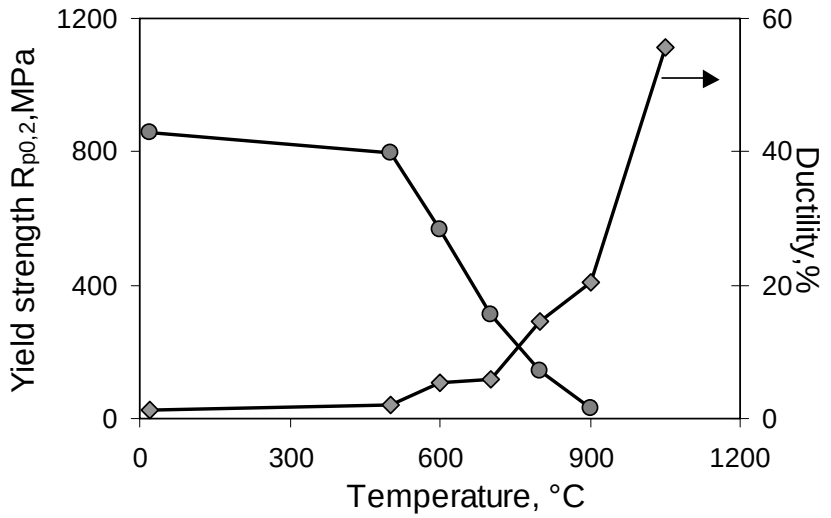

Figure 2.18 – Yield strength and ductility of free standing PWA 276 coating alloy [46]

The creep behaviour for three different MCrAlY coatings in a temperature range between 600°C and 1050°C is shown in Figure 2.19.

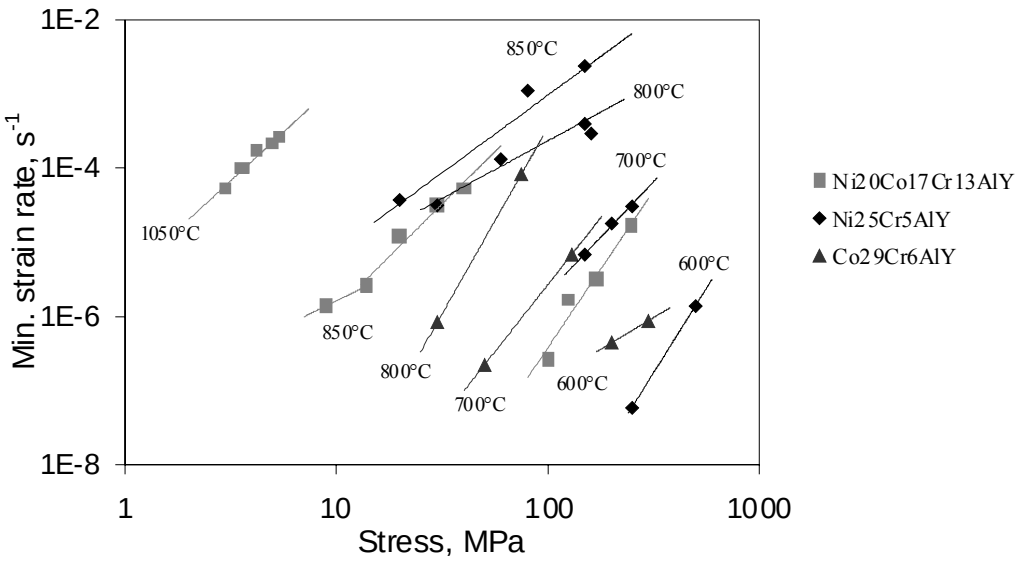

Figure 2.19 – Min. strain rate as a function of applied stress and temperature for three different MCrAlY coatings [42,44,46]

The creep resistance of MCrAlY coatings decreases sharply with temperature increase. The high creep rates up to 10^{-3} s^{-1} are observed already at 850°C for stress levels less than 100 MPa, which can lead to fast stress relaxation [48, 49].

2.1.4 Base material

The highly loaded components of gas turbines are mainly produced from Ni-base superalloys, which comprise an optimised combination of high temperature properties such as strength, creep resistance and fatigue strength. The high temperature strength of superalloys is based on the principle of a stable matrix combined with either precipitation strengthening and/or solid-solution hardening.

The major phases that may be present in Ni-base superalloy are [50]:

- γ -phase: the face-centred cubic Ni-base superalloy matrix that usually contains a high percentage of solid-solution elements such as Co, Cr, Mo and W.
- γ' -phase: ordered intermetallic compound $Ni_3(Al,Ti)$ with $L1_2$ structure
- carbide: MC, where M= Ti, Ta, W, Cr, Hf. At high temperatures other carbides can form : $MC + \gamma \rightarrow M_{23}C_6 + \gamma'$ or $MC + \gamma \rightarrow M_6C + \gamma'$
- TCP (topologically close packed) phase: precipitation of refractory elements W, Mo with hexagonal or tetragonal structure. For instance, σ-phase Ni(Cr,Mo) and μ-phase $Cr_7(Co,W)_6$

CMSX-4 or derivatives are single crystal (SC) Ni-base candidates for the highly stressed blades and vanes, which belongs to the second generation of SC superalloys. One of the main features of the second-generation alloys is the addition of rhenium (about 3 wt.%), which is known to strengthen the γ matrix and also to retard the coarsening of the γ' phase [51].

In the initial state, CMSX-4 shows a high volume fraction of approx. 70–75 % regularly cubic γ' particles, whereby their edges are oriented in the crystallographic <001> direction after appropriate heat treatment (Figure 2.19).

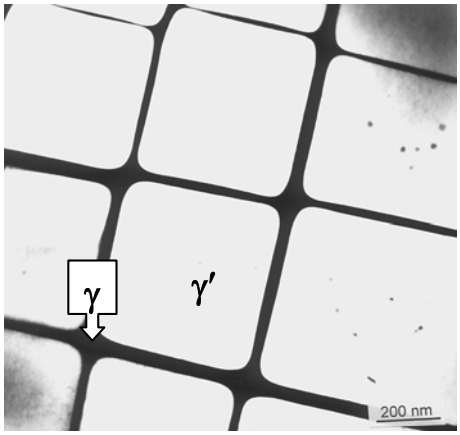

Figure 2.19 – An example of the single crystal Ni-base superalloy CMSX-4 microstructure in as received state showing γ' cubes separated by small γ channels

The introduction of single crystal technology provided significant reduction of carbides and other inclusions due to absence of grain boundaries. Moreover, the <001> crystal orientation, which is also the direction of natural growth, offers the best combination of the required mechanical properties [52].

The temperature dependence of elastic moduli for different orientations shows a nearly linear decrease up to about 900°C and more strong decrease between 900 and 1200°C, with the minimal values for <001> orientation (Figure 2.20).

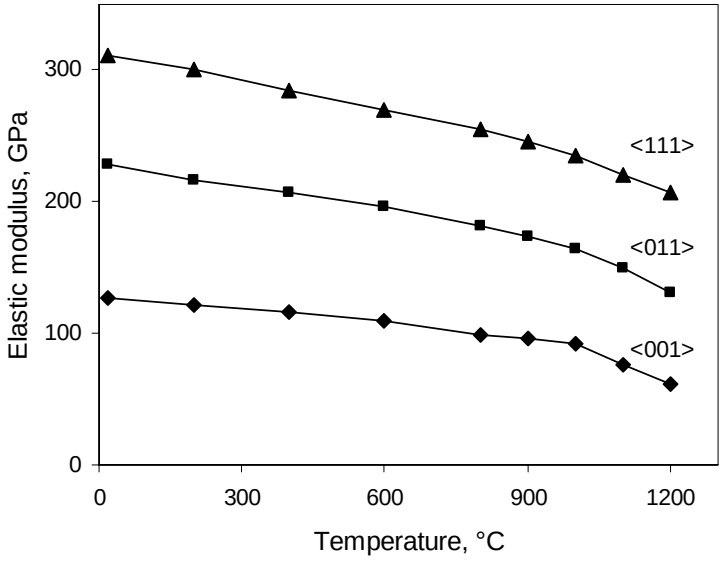

Figure 2.20 - Elastic moduli for different orientations of CMSX-4 as a function of temperature [53]

The yield strength of Ni-base superalloys, precipitation hardened with γ′, remains constant or even shows a slight increase as temperatures are increased up to about 750°C; at temperatures above 850°C, a steep decrease in strength occurs [54]. With increasing volume fraction of γ′ precipitates, the maximum yield strength increases.

The temperature dependence of the 0.2%-yield strength and the fracture strength may be represented as a superposition of the temperature dependencies of a pure γ phase, with a continuous decrease in strength with increasing temperature; and the anomalous behaviour of the intermetallic γ′ phase (in which yield strength increases with increasing temperature) [55], as shown in Figure 2.21. Therefore, the volume fraction of γ′ clearly influences alloy strength.

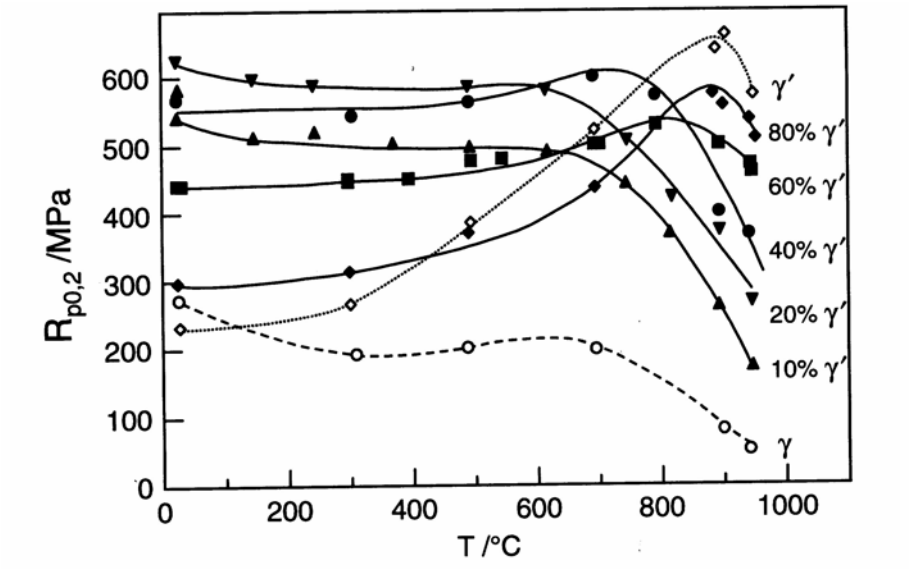

Figure 2.21 - Yield strength for different volume fraction of γ' phase in Ni-base superalloys as a function of temperature [55]

The choice of base material is usually based on its creep and fatigue strength for given operating conditions [56]. Besides the high volume fraction of γ′, the following are of further importance for the creep resistance:

- the absence of grain boundaries;
- the shape and distribution of the γ′ precipitates;
- the cast dendrite structure;
- the amount of eutectic regions.

The creep resistance at high temperatures is to a large extend due to the strengthening effect of the ordered γ′ particles, which act as effective obstacles against dislocation motion.

The most important time dependent property of Ni-base superalloys is fatigue life, which is related to crack initiation and propagation [57]. For CMSX-4 superalloy, LCF lifetime shows a strong decrease with increasing temperature (Figure 2.22). This effect is more pronounced at low total strain ranges, whereas the fatigue lives are close at high strain range [51].

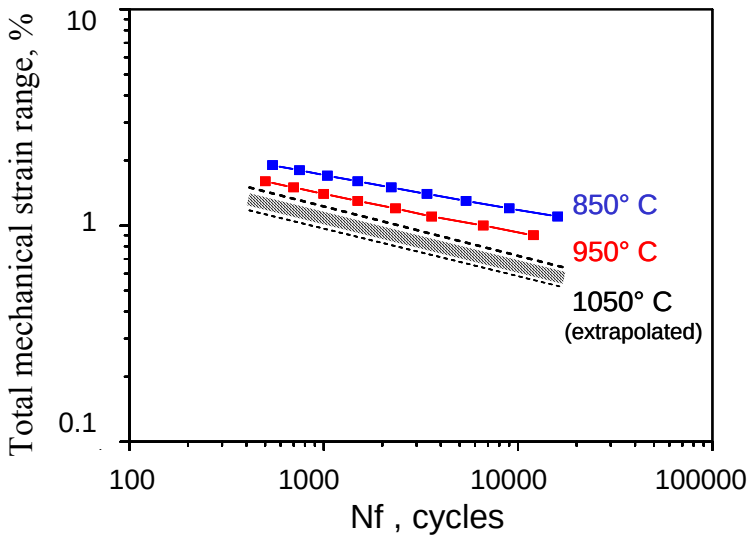

Figure 2.22 – Effect of temperature on low cyclic fatigue lifetime for CMSX-4 Ni-base superalloy [51]

2.2 Degradation of APS TBCs

The degradation processes in APS TBCs under service conditions depend strongly on the material constituents and properties, as well as on the particular loading profile. The major difference in the loading profile of TBCs is the thermal cycle characteristic: thermal cycles of stationary gas turbines last from several hours for peak-load operation up to times of the order of a year in base-load operation. In addition to the high temperatures, the blades are also subjected to mechanical strains. Finally, fatigue cycles occurred from each turbine start-up and shutdown as the load changes from zero to maximum and back to zero. Turbine components thus experience thermomechanical loading, which leads in most cases to the ceramic top coat spallation near the TBC/bond coat interface [58,59,60,61].

The complex process of degradation is affected by:

- growth of the TGO and oxidation-related processes at the interface;
- thermal-expansion mismatch strains and stresses at the metal-ceramic interface;
- sintering processes in the TBC, which affect stiffness, thermal conductivity and crack resistance;
- diffusion of elements from the base material and bond coat to the interface;
- cyclic plastic and time dependent deformation, as well as stress relaxation;
- temperature gradient across the TBC;
- transient factors caused by high heating and cooling rates, etc.

Besides the above-mentioned degradation mechanisms, the lifetime of the TBC systems at high temperatures is controlled by time dependent deformation, i.e. creep and cyclic fatigue, while in service, the thermomechanical fatigue is a major lifetime limiting factor.

2.2.1 Oxidation of MCrAlY alloys

At high temperatures bond coat oxidation leads to the formation and growth of oxide scales (TGO) at the bond coat / TBC interface. The characteristics of this process such as the growth mechanism, growth rate and TGO microstructure, as well as its adherence to the BC and TBC, are critical factors that affect the durability of TBC systems [62,63].

For NiCrAlY alloys, it is the aluminium oxide, which is the most stable oxide at 1000°C compared to the oxides of other major alloying elements as shown in Figure 2.23.

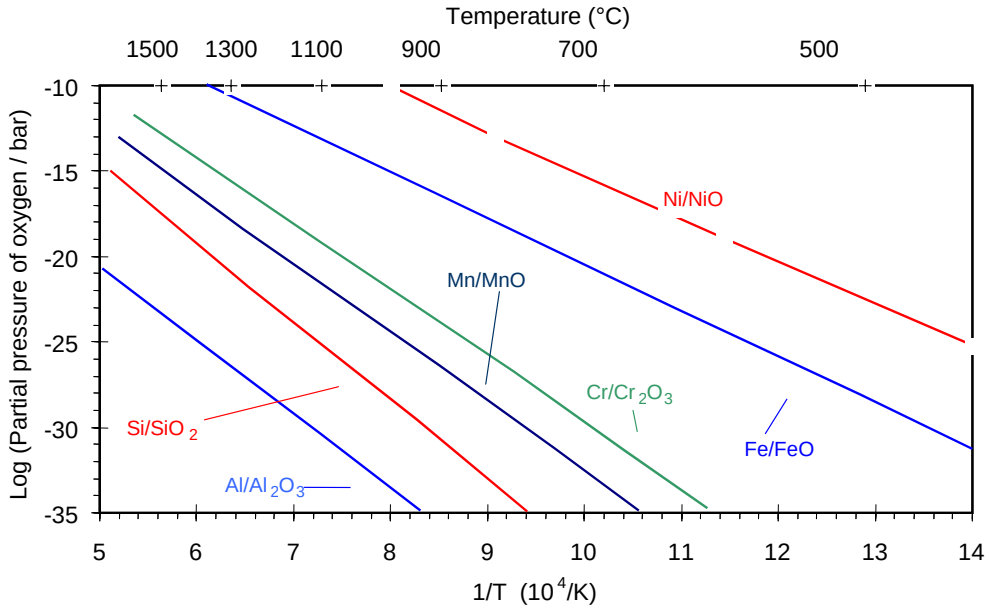

Figure 2.23 - Temperature dependence of oxygen partial pressure at the metal/scale interface [64]

Formation of more than one oxide type during the initial stage of oxidation is known as transient oxidation, but the more thermodynamically stable oxide scale formation usually predominates. However, kinetic factors also come into play at this stage and determine whether a continuous scale of more thermodynamically stable oxides can be established or not [65].

The contribution made by transient oxides and spinels to the failure of TBC systems can be related to the lower mechanical strength of these mixed oxides compared to alumina, as well as volumetric changes associated with the transformation of transient oxides to more thermodynamically stable phases with continued exposure.

If depletion of the scale-forming element, i.e. Al, occurs during oxidation, then its activity decreases with exposure time. It leads to an increase in oxygen partial pressure at the scale / alloy interface. After critical Al-depletion, the oxygen partial pressure can reach a value, which is sufficiently high for the next stable oxide (chromia) to form. The respective oxidation map is shown in Figure 2.24.

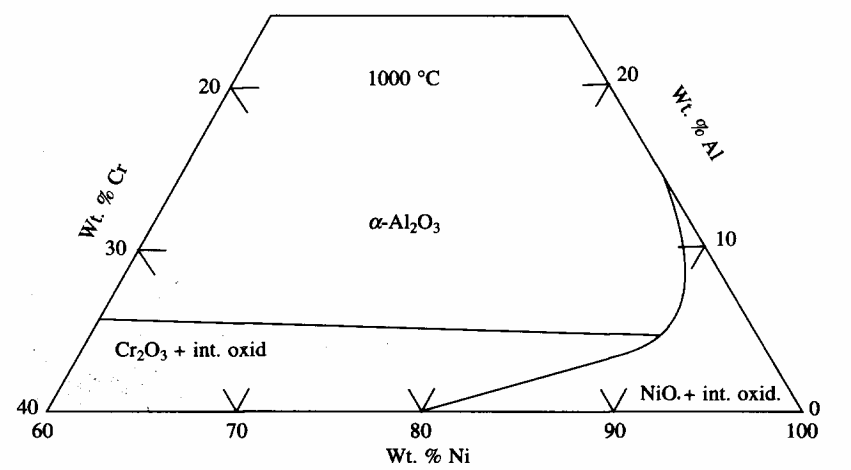

Figure 2.24 - Oxidation map for the oxidation of Ni-Cr-Al alloys at 1000°C [66]

Formation of less stable oxides such as α-chromia or (Co, Ni)(Cr, Al) spinel is undesirable because they are not as protective as alumina due to their high growth rates and other factors. For instance, as suggested in [67], the TBC/spinel and TBC/Cr_2O_3 interfaces have lower interfacial fracture resistance compared to TBC/Al_2O_3 interface and conversion of Al_2O_3 into other mixed oxides as a result of aluminium depletion in the bond coat causes these systems to fail.

During the formation of alumina scales, the aluminium and/or oxygen diffusion through the scale determines the oxide growth. As a result, gradients in metal activity and oxygen partial pressure are established across the scale. The scale thickness is generally and roughly proportional to the square root of exposure time [68]:

$$x = k_P \cdot t^{1/2}, \qquad \text{Eq. 2.4}$$

where $k_P = \left[2D_i \frac{\mu_i' - \mu_i''}{const} \right]^{1/2}$ is the parabolic rate constant,

D_i – ionic diffusion coefficient;

μ_i – chemical potential

The examples of parabolic rates constants in the temperature range between 1200°C and 1400°C for the growth of different oxides are represented in Figure 2. 25.

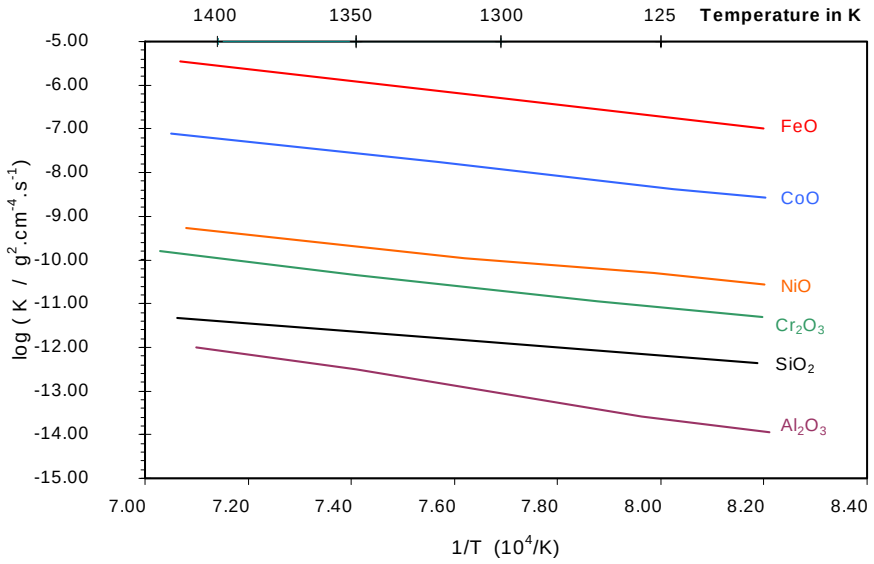

Figure 2.25 - Parabolic rate constants for the growth of different oxides [64]

The oxidation kinetics of MCrAlY alloys is significantly affected by the presence of minor additions such as Y, Zr, or trace elements like Si, Ti etc. They improve scale adherence, decrease growth rate, and enhance selective oxidation in the yttria-containing alloys [38]. However, the mechanisms responsible for the beneficial effects of RE are not clear and there are still controversial ideas on the proposed mechanisms. It has been also reported that the amount and distribution of RE has a significant effect on the performance of MCrAlY coatings [69,70].

In some cases, the initial alumina that forms is not the stable α-Al_2O_3 but metastable phases. The temperature and the surface condition are important factors that affect the development of metastable aluminium oxides [71]. The aluminium oxide has several different crystal structures, including γ-, δ-, θ- and α-Al_2O_3. It should also be taken into consideration that it is not only one Al_2O_3 modification that grows, but also simultaneous nucleation and transformation sequences, leading to both local expansion and shrinkage phenomena. Phase transformations are responsible for local shrinkage and pore formation, which explains why a TGO constrained macroscopically to high stresses contains voids and microcracks. Compared to a very dense oxide layer, the formation of small defects might be advantageous in reducing local maximum stresses by quasi-plastic deformations [72].

2.2.2 Sintering

During high temperature exposure, a sintering process in ceramic top coating may occur, primarily due to surface diffusion. In particular, phenomena involved in microcrack healing and shape changes are reported to take place at temperatures as low as 900 C, while the pore system seems to be affected by sintering only at temperatures higher than 1200–1300 C [73].

Sintering occurs depending on the impurity content (powder composition), especially the silica, which lowers sintering temperatures and increases the sintering behaviour of the YSZ

ceramics. The presence of elements such as Al or Ce can suppress sintering because they diffuse to the grain boundary and prevent the sintering process [74].
Sintering densification processes can result in both an increase of coating elastic modulus or shrinkage, both of which are detrimental for coating performance [75].

2.2.3 Interdiffusion

Interdiffusion processes at the bond coat/substrate interface and the bond coat / TGO occur already during the coating process and become significant during high temperature exposure. An inward diffusion of aluminium leads to the formation of a oxide layer (preferably alumina) on the surface of the bond coat. Microstructural changes on the BC/substrate interface are influenced by the presence of various elements in the coating and substrate.
For TBC systems consisting of CMSX-4 substrate material coated with EB-PVD NiCoCrAlY bond coat and an EB-PVD top coat, growth of the diffusion zone at BC/substrate interface during 1100°C heat treatment was mainly directed into the γ/γ′substrate alloy where γ phase and also β phase was formed at the expense of γ′. The formation of TCP-rich interdiffusion zone after heat treatment of between 10 and 50 hours at 1100°C suggested that diffusion of the refractory elements into the bond coat was initially hindered by an inward growth of the γ/β diffusion front. With an increasing time of exposure, the TCP phases were re-dissolved and assumed to diffuse into the bond coat [76].
The diffusion of refractory elements into the coating can also degrade the oxidation resistance of the coating [77]. However, the diffusion of Re into the aluminide coating might improve the performance of the coating at high temperatures since a considerably reduced oxidation rate and markedly improved thermal cycle fatigue behaviour have been found in a Re-containing overlay coating [78]. Czech et al have compared the oxidation rate of two kinds of overlay coatings, one with 3 at.% Re and another free of Re at 950 C. They found that the oxidation rate of the former was much slower than the latter.
The microstructure of a Pt-aluminide coating on a Ni-base single crystal CMSX-4 superalloy before and after TMF testing has been characterised in [79]. Tungsten-structured precipitates were observed in the outer coating layer and μ phase precipitates in the inner coating layer. After TMF the original substrate adjacent to the original interface transformed into a mixture of β/γ′ phases with a new μ phase precipitating along β grain boundaries. Just over the interface, many needle-like σ phases precipitated on the substrate. It appeared that the precipitation of tungsten, μ and σ phases was associated with the presence of platinum and rhenium and the interdiffusion of elements at high temperature. No microcracking in the coating due to the presence of TCP phases was found [79].
A recent study on the influence of long-term ageing heat treatments on the tensile behaviour of single crystal MC2 nickel-based superalloys has revealed that the precipitation of brittle particles of a tungsten-rich μ phase did not induce any deleterious effect on the tensile strength or ductility [80]. The decrease in yield strength and the increase in ductility were

attributed to the coarsening of the γ′ strengthening particles, which promotes passing the precipitates by matrix dislocations.
However, since TCP phases contain high refractory element contents, and their precipitation can weaken the strength of the substrate even when they are present in a blocky shape, the presence of these TCP phases should be avoided.

2.2.4 Stresses in TBC

The TGO formed during high temperature exposure are subjected to stresses, which arise from the oxide growth process itself or as a consequence of stresses acting on the material. Under thermal cyclic loading, the oxide scale is subjected to compressive stresses upon cooling due to mismatched thermal expansion coefficients (Figure 2.26).

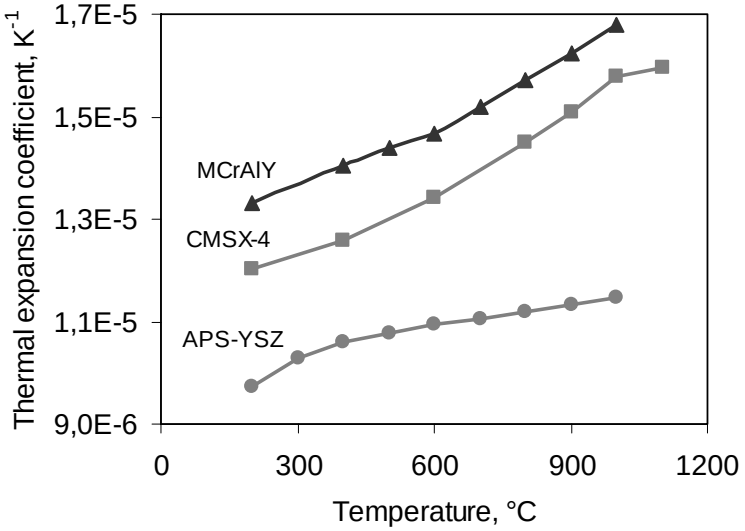

Figure 2.26 - Temperature dependence of thermal expansion coefficients in TBC system [37]

The stress, which arises from the different thermal expansion coefficients for a temperature range ΔT can be estimated for thin scales on thick substrates as follows [62]:

$$\sigma_{ox} = \frac{-\mathrm{E}_{ox}\Delta T(\alpha_{met} - \alpha_{ox})}{1-\nu} \qquad \text{Eq. 2.5}$$

, where

$\mathbf{E}_{ox}$ is the elastic modul of the oxide;

ν is Poisson's ratio (assumed to be the same for metal and oxide);

α_{met} and α_{ox} are the thermal expansion coefficients of the metal and the oxide, respectively.

The thermal expansion mismatch between the top coat and the bond coat puts the top-coat in overall compression at room temperature. However, these stresses are an order of magnitude

lower than the residual stresses in the TGO, primarily because the porous and cracked top-coat is much more compliant in relation to the TGO, and it has a relatively lower thermal expansion-coefficient mismatch with the bond-coat [81].
Due to the highly undulating nature of the metal/ceramic interface, out-of-plane stresses result in the vicinity of the TGO/top-coat interface: tension at the crests and compression at the troughs. Furthermore, redistribution of these stresses might occur at high temperatures due to BC and/or TGO creep and stress relaxation.

2.2.5 Low cyclic fatigue

Low cyclic fatigue (LCF) tests can capture a couple of the important damage mechanisms under isothermal conditions in the temperature range of actual component cycles [82, 83].
The isothermal LCF lifetime of single crystal Ni-base superalloys depended on ductility, decreasing with temperature from 1050°C to 650°C, as shown in Figure 2.27. For coated superalloys, the lifetime was similar at higher temperatures, but at 650°C (below BDTT), where the coating has little ductility [84, 85], cracks initiating in the coating reduced lifetime in the low plastic strain range regime (see Figure 2.27). Coating cracks are promoted in areas cycled into tension at lower temperatures and propagated into the superalloy causing its failure.

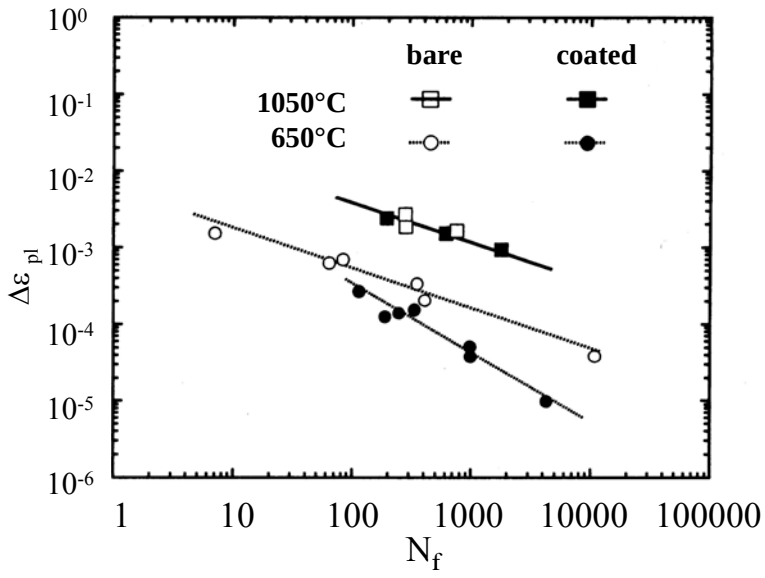

Figure 2.27 – The dependence of cyclic life of bare single crystal Ni-base superalloy PWA 1480 and with NiCoCrAlY- bond coat vs. plastic strain range under isothermal LCF [86]

Under high heat flux thermal cycling conditions, the failure mechanism associated with LCF is closely related to ceramic coating sintering and creep at high temperatures [87]. It was found that surface cracks in the ceramic coating initiate and propagate continuously under complex thermal low cyclic fatigue stresses. Due to the ceramic/bond coat elastic mismatch,

these vertical cracks can deflect along the ceramic/bond coat interface, thus eventually leading to coating delamination under subsequent LCF loading. The creep strains developed at high temperatures induce tensile stresses in the ceramic coating during cooling, and thus provide the major driving force for the crack growth under LCF conditions.
However, isothermal tests may not capture many of the important damage micromechanisms under varying temperature conditions. Recently, considerable effort has been devoted to developing TMF tests for the simulation of the behaviour of the materials undergoing thermomechanical fatigue.

2.2.6 Thermomechanical fatigue (TMF)

In TMF tests, a specimen is subjected to a desired temperature and mechanical strain path with different phase relations. Four different TMF test types with fully compensated thermal expansion and symmetrical total strain amplitude can be distinguished [88, 89].
There are two general types: in-phase (IP), with the maximum tensile strain at the maximum temperature and the maximum compressive strain at the minimum temperature, and out-of-phase (OP), with inverse behaviour. They are capable of reproducing many of the relevant damage mechanisms, which are observed under TMF conditions. Another two types are clockwise-diamond (CD) and counter-clockwise-diamond (CCD), the intermediate temperatures being reached at the largest tensile and compressive strains, respectively and the highest and lowest temperatures at zero strain.

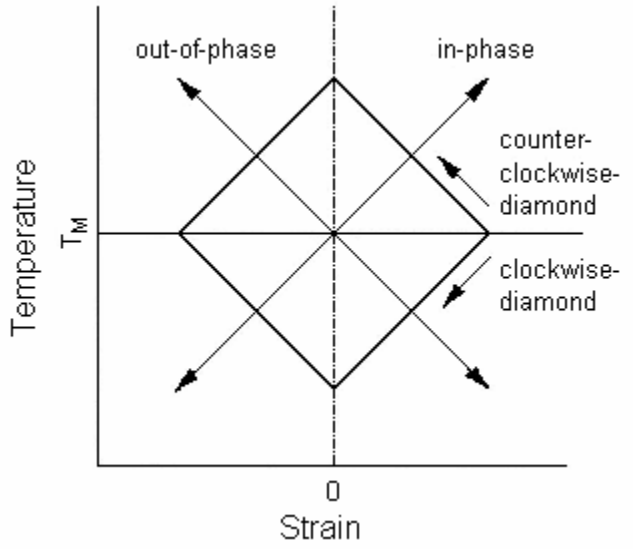

Figure 2.28 - Temperature – strain cycles for different TMF tests [89]

The mechanical strain (ε_{mech}) is the sum of the elastic and inelastic strain components, while the total strain (ε_{tot}) is the sum of thermal and mechanical strain components:

$$\varepsilon_{tot} = \varepsilon_{th} + \varepsilon_{mech} = (T-T_0)\cdot\alpha + \varepsilon_{mech} \quad \text{Eq. 2.6}$$

where $_{th}$ is the thermal strain;

T_0 is the reference temperature where the test starts;

T is the test temperature;

α is the coefficient of thermal expansion.

The most damaging cycle is OP TMF when the high tensile stresses applied at low temperatures lead to earlier crack initiation and the failure of base material. Cracks developed perpendicular to the loading direction starting at the TBC/bond coat interface and growing into the bond coat. One of these cracks eventually penetrated into the substrate and led to failure of the TMF specimen [90,91].

Studies on TMF behaviour reported in the literature are limited for TBC systems, moreover, the difference in experimental procedure makes the comparison of published results very difficult. Both the failure by spallation of TBC and the fatigue failure of bond coat and base material have been reported [92,93]. It was shown by [93] that annealing treatment before TMF testing had a strong impact on the damage behaviour of the TBC system. Presence of TGO with a certain thickness activated oxidation related damage mechanisms and led to the delamination failure of the TBC.

2.3 Failure mechanisms, lifetime models

Failure of plasma-sprayed TBCs typically occurred by ceramic topcoat spallation because of the formation and growth of microcracks at the bond coat/ topcoat interface. It has been suggested that different crack paths depend not only on TBC composition but also on variations in the exposure conditions.

For isothermal exposure, it was reported [94] that the fracture progressed primarily along the TGO/bond coat interface with excursions into the TGO. This behaviour has been described in [95] and explained as fracture initiating at defects, such as transient oxides or RE rich internal oxidation but then propagating along the interface to release all of the elastic energy in the TGO.

In another study, the TGO thickness was taken as a critical parameter. Once this critical TGO thickness was reached (5.5 μm), cracks where observed to initiate at large undulations in the interface and they propagated in the TBC as well as through the TGO and along the interfaces [63].

Under thermal cycling operation, TBC systems often fail by crack initiation and propagation close to the bond coat–top coat interface. This failure is attributed to stresses arising from TGO formation on the rough bond coat surface as well as thermal expansion mismatch [96]. The actual stress situation is rather complex due to the fact that many factors contribute to the failure of TBC systems. They can be taken into account by using a finite element method (FEM) to calculate stress development during thermal and/or thermomechanical loading.

Furthermore, it is generally agreed that spallation occurs through the eventual linkage of microcracks rather than the rapid propagation of a single crack. The description of the entire process requires a model of local failure modes on a microscopic level [97]

Over the past few years, different approaches for the numerical simulation of the stress response at the BC/TBC interface have been reported [98,99,100,101,102,103,104,105].

The combination of oxidation, top coat creep and bond coat creep yields a stress distribution in time and in location along the interface that is unachievable by any one mechanism acting alone. The overall picture of the failure mechanism resulting from this evolution of residual stresses is as follows [99]: (1) Early cracking at bond coat peaks, driven by tensile peak stresses generated due to creep processes. (2) Cracks generated early in life do not propagate due to creep generated compressive stress regions over the valleys. (3) At increased numbers of cycles, and therefore increased oxide thickness, stresses over the valleys become increasingly tensile and the size of the tensile region increases. (4) The tensile region over the valley is then capable of sustaining crack growth, which leads to the near-peak cracks generated during early cycling being linked. This description of failure is supported by qualitative observations of cracking progression. The progression of cracking deduced from stresses predicted in the current model also support the failure progression proposed by Chang et al [98].

A model based on microstructural mechanisms for describing the crack growth and failure of thermally cycled APS thermal barrier coatings was developed by Vassen et al [100]. The model contains the most important elements in the failure of APS-TBCs, i.e. bondcoat roughness, TGO growth, substrate curvature, creep effects. Further elements, e.g. sintering, can be introduced easily. The model is able to explain most of the results found for thermally cycled specimens at least in a qualitative way.

Potentially failure relevant parameters were further evaluated in [103,104] by taking into consideration TGO creep. The influence of the creep properties of the TBC and the TGO on the stress state was studied through the example of a thin TGO layer. Although failure occurs at low temperatures, where creep is unimportant, creep during the high temperature phase can cause the stresses to relax because of the growing TGO layer and can thus result in a stress-free state at the end of hot time exposure. It was shown that without creep in the TGO, very large tensile stresses would occur in the TBC and the above-mentioned shift of the tensile region from the peak to the valley of the asperity will take place. If, on the other hand, creep in the TGO is much faster than in the TBC, growth stresses are relaxed almost entirely, and the stress state will not differ much from that without TGO as long as the TGO layer is not too thick. Thus, stress relaxation during hot time is an important factor in the determination of the stress state. It is expected to prolong TBC life compared to a situation where relaxation by creep is insignificant.

In FE calculations in Herzog et al [105], experimentally determined creep data for a plasma-sprayed thermal barrier coating as well as for a NiCoCrAlY bond coat were implemented into the FE package and used for the calculations. The stress response under cyclic oxidation loading was then investigated by successive and stepwise consideration of continuous TGO

growth, TBC creep, BC creep, lateral TGO growth and TGO creep. The results were compared to experimental studies on crack formation and growth, which revealed various crack patterns in APS-TBC. However, one crack type was reported more often, i.e. crack formation at the BC/TGO interface at peak regions of undulations. These types of cracks are reported to propagate through the TGO at the flanks of undulations and penetrate into the TBC over valleys. The current simulation results are compared to these experimental findings in particular. It can be concluded that the most accurate life prediction system would be the one for which failure mechanisms are known for a specific TBC under its relevant operating conditions.

3 Experimental

3.1 Materials

In the present work, the thermal barrier coating system consisted of the single crystal Ni-base superalloy CMSX-4, a NiCoCrAlY bond coat (PWA 286) and an YSZ thermal barrier coating (Metco 204 NS). The nominal chemical compositions of the components are given in Table 3.1. The bond coat was about 150 µm thick and deposited by low-pressure plasma spraying (LPPS). The TBC was air-plasma sprayed (APS) and about 300 µm thick. All coatings were supplied by IWV-1, Forschungszentrum Jülich GmbH.

Table 3.1- Chemical composition of TBC

CMSX – 4												
Element	**Ni**	**Co**	**Cr**	**Al**	**Ti**	**Ta**	**W**	**Mo**	**Re**	**Hf**	**Zr**	**C**
wt.%	Rest	9.6	6.5	5.64	1.03	6.5	6.4	0.6	2.9	0.11	0.001	0.003

PWA 286						
Element	**Ni**	**Co**	**Cr**	**Al**	**Y**	**Hf**
wt.%	48.3	21.1	17.1	12.6	0.61	0.4

Metco 204 NS										
Element	**ZrO_2**	**Y_2O_3**	**HfO_2**	**TiO_2**	**Al_2O_3**	**CaO**	**SiO_2**	**MgO**	**CeO_2**	**Fe_2O_3**
wt.%	91.4	7.78	1.62	0.113	0.053	0.015	0.019	<0.002	0.024	<0.003

The specimen manufacturing and heat treatment were divided into several parts: (i) solution heat treatment of CMSX-4; (ii) precipitation aging of CMSX-4, which consisted of two stages, (iii) bond coat application after the first precipitation ageing and (iv) ceramic topcoat application after the second heat treatment. Details of the heat treatment process are given in Table 3.2.

Table 3.2 - Heat treatment procedures

Solution annealing of CMSX-4	
In vacuum, at 1280°C, for 0.2 h	Air cooling > 150 °C/min
In vacuum, at 1290°C, for 3.0 h	
In vacuum, at 1305°C, for 6.0 h	
1st precipitation ageing of CMSX-4	
In vacuum, at 1140°C, for 6.0 h	Gas cooling
VPS bond coat application	
Diffusion heat treatment and pre-oxidation	
In vacuum, at 1080°C, for 4 h	Air cooling > 150 °C/min
2nd precipitation ageing of CMSX-4	
In vacuum, at 870°C, for 20h	Air cooling > 150 °C/min
APS TBC application	

The microstructure of the TBC system in as-received state is shown in Figure 3.1. The APS topcoat microstructure had typical crack network and inter-splat porosity as well as columnar grain morphology (Fig. 3.1.b). The total porosity was about 11-12%. The NiCoCrAlY bond coat microstructure mainly consists of two phases, which are homogeneously distributed over the thickness. The β-(Ni(Co)Al) precipitates with an average diameter of ~2 µm took up about 70% of the total volume in a continuous γ-(Co/Ni/Cr) phase (Figure 3.1.c). The Ni-base superalloy in the initial state showed a high volume fraction of approx. 70-75% cuboidal γ′-precipitates (Ni_3Al) with their edges oriented along the <001> direction in the γ matrix. The γ′ particle size was about 0.5 µm and the width of the γ-channels was ca. 50 nm (Figure 3.1.d).

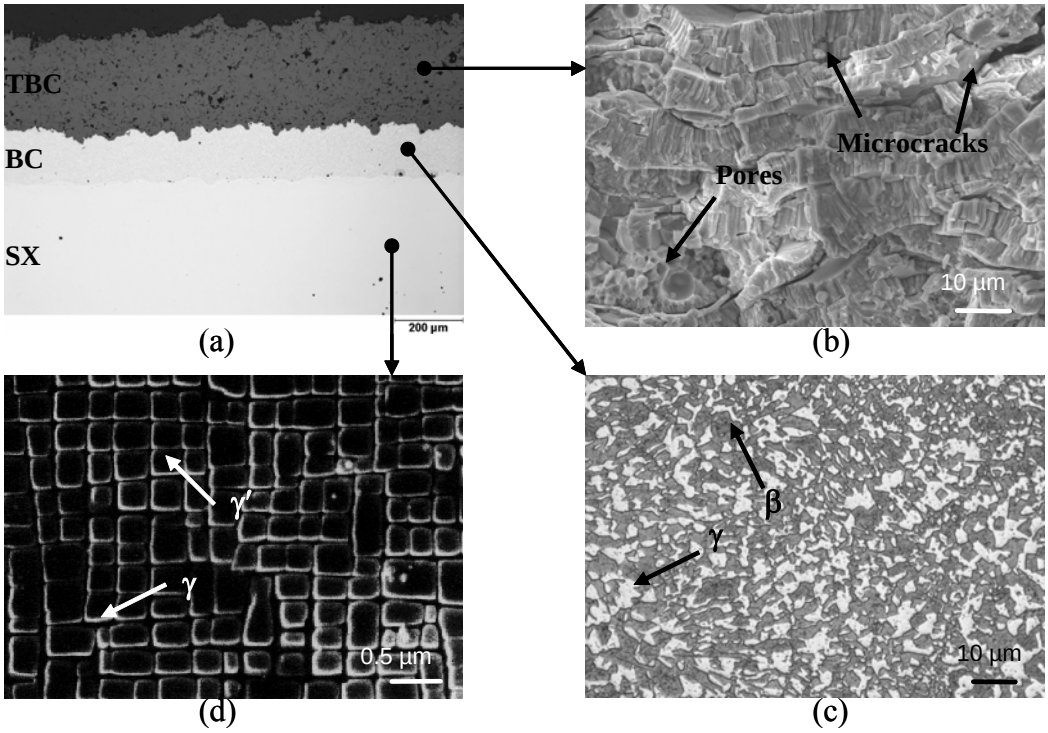

Figure 3.1 - Microstructure of TBC system in as-received state

3.2 Experimental procedures

3.2.1 TMF testing

The TMF tests were conducted using a universal testing machine (Instron, model 8802) with a 100 kN load cell (50 kN dyn / 100kN stat) equipped with an 24 kW - infrared furnace (24 halogen lamps 1 kW each) from Xerion GmbH. To achieve uniform temperature distribution throughout the specimen, IR lamps were arranged in 3 circuits with 8 lamps over the each circuit. Cooling was performed by internal and external compressed air flows. The temperature was controlled with ±10°C measuring error along the gauge length using 3 pyrometers, which were calibrated in advance with Pt/Pt-Rh-thermocouples. The specimen

deformation was monitored using two high-temperature extensometers from MTS systems GmbH. An overview of the TMF testing equipment is given in Figure 3.2.

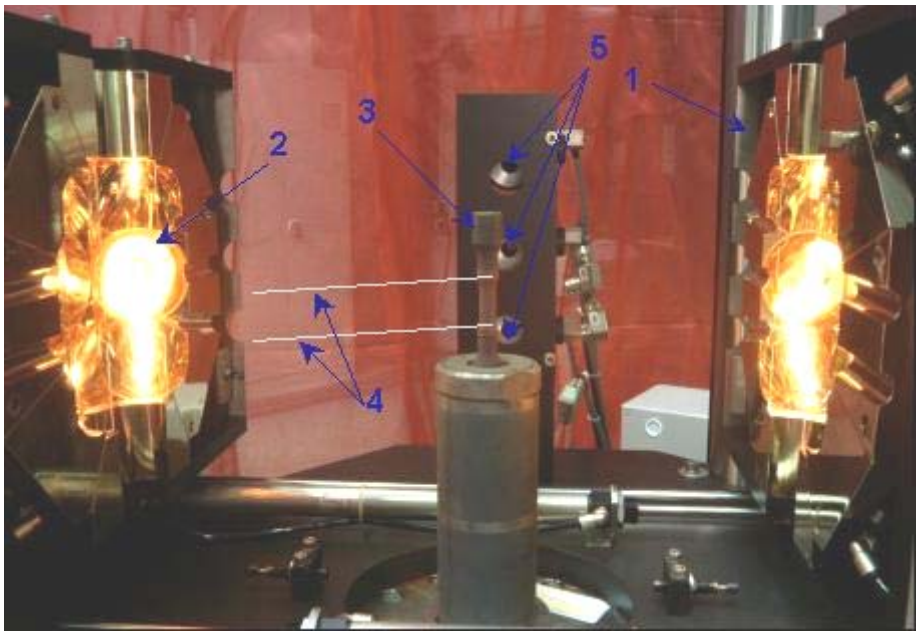

Figure 3.2 – Overview of the TMF testing equipment: 1- furnace half; 2- lamp with reflector; 3- specimen; 4- extensiometers; 5- optical pyrometers

Hollow cylindrical specimens with internal diameter of 6.85 mm and external diameter of 10 mm over the gauge length of 20 mm were used for TMF tests. The geometry of the TBC-coated fatigue specimen is shown in Figure 3.3. Before the tests it was coated with iron oxide to improve absorption of IR radiation.

Figure 3.3 - TMF specimen configuration

The TMF tests were carried out under strain control with different mechanical strain ranges, namely 0.6% and 0.3% and a temperature range of 350°C-1050°C. Two cycle shapes were used, out-of-phase (OP) and in-phase (IP), as shown schematically in Figure 3.4. In some tests, the dwell time of 120 minutes at T_{max} = 1050°C was introduced. For the OP TMF without a dwell time, pre-oxidation treatment was carried out for 300 hours, 1000 hours and 2000 hours.

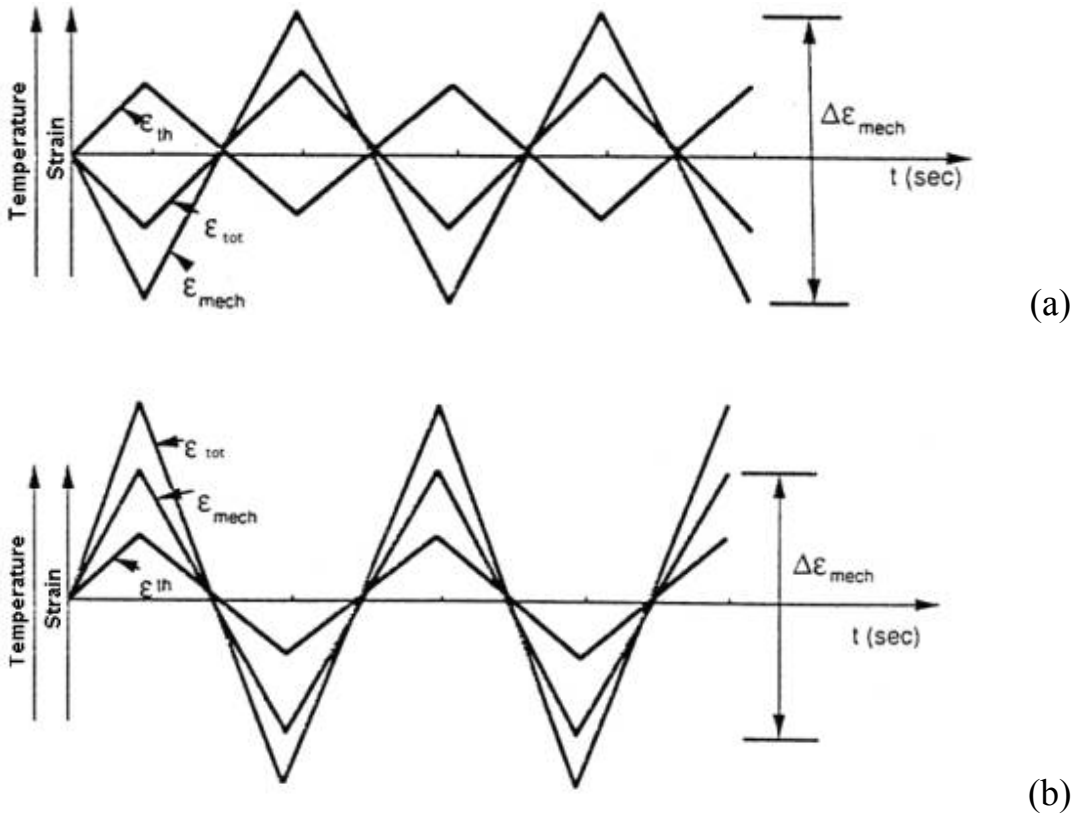

Figure 3.4 – Schematic presentation of the temperature-strain behaviour corresponding to (a) OP TMF and (b) IP TMF test

Prior to each TMF test, the thermal strain, ε_{th}, was determined for each sample with the same temperature-time cycle under zero mechanical load. During TMF testing, the mechanical strain ε_m command was evaluated according to the cycle time (t). The thermal strain was calculated in real time from the measured temperature (T) and added to the mechanical strain to get the total strain as a signal input for the strain control of the mechanical testing:

$$\varepsilon_{tot} = \varepsilon_{th}(T) + \varepsilon_m(t) \qquad \text{Eq-n. 3.1}$$

The stresses were calculated using the sample cross-section including the thickness of both BC and TBC.

3.2.2 Thermal cycling

For the thermal cycling experiments in the temperature range 60°C -1050°C an infrared furnace from Xerion GmbH with 6 lamps of 1kW each was used (Figure 3.5). The temperature was controlled using an optical pyrometer calibrated before with Pt/Pt-Rh-thermocouples. Temperature distribution was ±15°C over the specimen's length. Cooling of the specimens was enhanced by external compressed air flow. To achieve a temperature gradient over the TBC thickness, internal air-cooling was applied. Temperature distribution

was calibrated by Pt/Pt-Rh thermocouples placed at external and internal surfaces as a function of airflow.

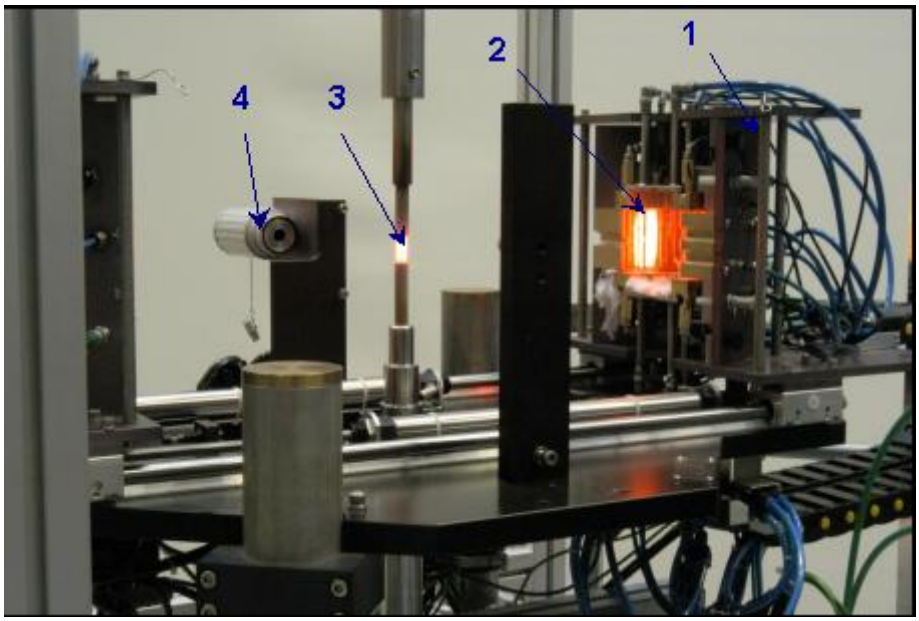

Figure 3.5 - Experimental set-up for thermal cycling: 1- furnace half; 2- lamp with reflector; 3- specimen; 4- optical pyrometer

Hollow cylindrical specimens with an internal diameter of 6.85 mm, an external diameter of 8.5 mm and length of 25 mm were used (Figure 3.6).

Figure 3.6 - Specimen configuration for thermal cycling

The thermal cycle consisted of 8 minutes heating and 8 minutes of forced air cooling followed by 1 minute dwell time at a minimum temperature for thermal cycling and 120 minutes of high temperature dwell time for a cyclic oxidation test, as shown in Figure 3.7.

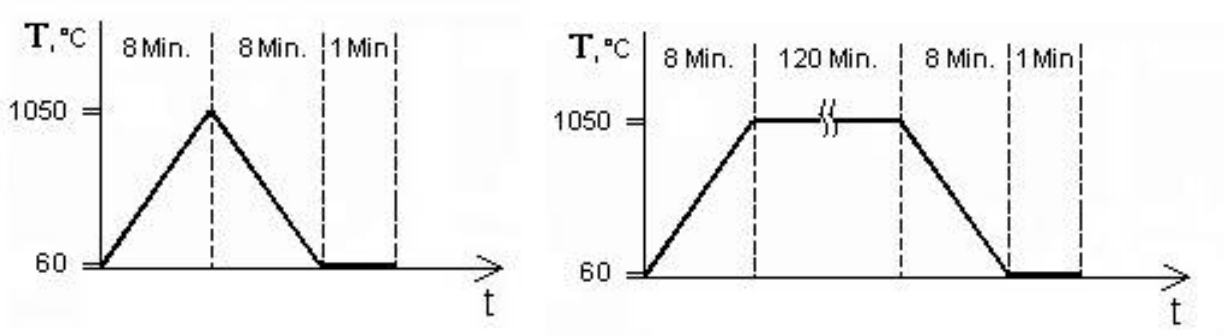

(a) (b)

Figure 3.7 – Typical cycles used during test procedures: a) thermal cycling; b) cyclic oxidation

3.2.3 Compressive deformation

The compression tests were conducted using an universal testing machine (Instron, model 1361) with 5 kN load cell equipped with 3-zone resistance furnace from Heraeus with Pt/Pt-Rh thermocouples which controlled the temperature with a measuring error ± 3°C over the gauge length. The specimen deformation was monitored using two opposite resistance foil strain gauges from Hottinger Baldwin Messtechnik, located near to the top and bottom contact plane of the specimen and pushing rod.

Freestanding TBC specimens of cylindrical geometry with an inner diameter of 14 mm, height of 12 mm and wall thickness of 0.5 mm were used (Figure 3.8).

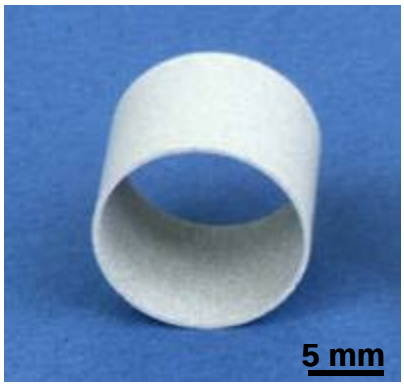

Figure 3.8 - Sample of free standing TBC

Specimens of cylindrical geometry were manufactured by air-plasma spraying a zirconia powder (204NS, Sulzer Metco) onto a conventional low carbon steel rod with a diameter of 14 mm. The TBC had a wall thickness of approximately 0.6 mm and a porosity level of 11-12%. The specimens were cut and ground to a height of 12 mm and a wall thickness of 0.5 mm. The steel rod was then completely dissolved with hydrochloric acid to obtain freestanding coatings.

The tests were carried out isothermally in the temperature range RT-1150°C with constant loads of 40 MPa, 80 Mpa,120 MPa, 260 MPa, 300 MPa and 380 MPa or constant strain rates of 10^{-4} s^{-1} and $10^{-6}s^{-1}$.

3.3 Microstructural investigation

3.3.1 Metallographic preparation

Before cutting, the specimens were cold mounted in epoxy resin to avoid additional damage to the coatings, which could have been caused by sectioning. A precision diamond saw with fine abrasives was used. For cylindrical specimens, both the transversal and longitudinal cross-sections were prepared.

Initial grinding started with 320-grit SiC abrasive paper followed by 400, 600, 800 and 1200 grit SiC paper. Polishing was carried out using diamond suspensions of 6 µm, 3 µm and 1 µm grain size followed by final polishing. Final polishing with colloidal silica provides a chemo-mechanical polishing (CMP) action, which significantly reduces subsurface damage and improves surface finish.

3.3.2 Microscopy

Polished cross-sections of selected samples were investigated under an optical microscope “Leica” 'MEF4M' equipped with 2/3-inch digital color camera ProgRes 3008 (Jenoptik AG). Magnification steps of 12.5, 50, 100, 200, 500 und 1000x were used.

The high resolution imaging of the microstructure and damage was carried out by a scanning electron microscope (SEM) LEO1530 – 'Gemini'. In general, the secondary electron (SE) or InLens-SE detectors were applied. Qualitative and quantitative chemical microanalysis (point, line, and area) was carried out using energy-dispersive HPGe-detectors (EDX). To investigate crystallographic properties, the electron backscattered diffraction method (EBSD) was used.

Moreover, *in-situ* deformation experiments were performed in SEM at room temperature in special attachment (tensile stage up to about 600°C).

3.3.3 Image analysis

Further microstructural evaluation was performed by a commonly used technique of image analysis. In the present study, “analySIS 3.2 Pro” software was used to measure TGO thickness, the size of interdiffusion zones as well as the crack length and location.

3.4 Non-destructive methods

3.4.1 Acoustic emission (AE)

AE analysis is a non-destructive technology for the investigation of material properties and damage behavior. A short, transient AE event is produced by a very fast release of elastic energy, e.g. by crack formation. An elastic wave propagates in all directions and can be detected by appropriate sensors and analyzed. Commercial AE devices detect and interpret the acoustic events resulting from these crack processes and can identify, locate, and display damage in the initial stages in the tested object within very short time.

The behavior of the material and when the release of elastic energy begins, e.g. by crack formation, are influenced by the material properties and the environmental conditions. The elastic wave propagating through the material is detected and converted into an electrical AE signal by piezo-electric sensors (Figure 3.9). The AE system processes the AE signal, converts the detected bursts into future data sets, determines the crack source locations, calculates statistics, and displays them graphically and numerically in real time.

So-called parametric channels measure the environmental conditions (such as temperature) as well as the external load as reference parameters for the detected AE.

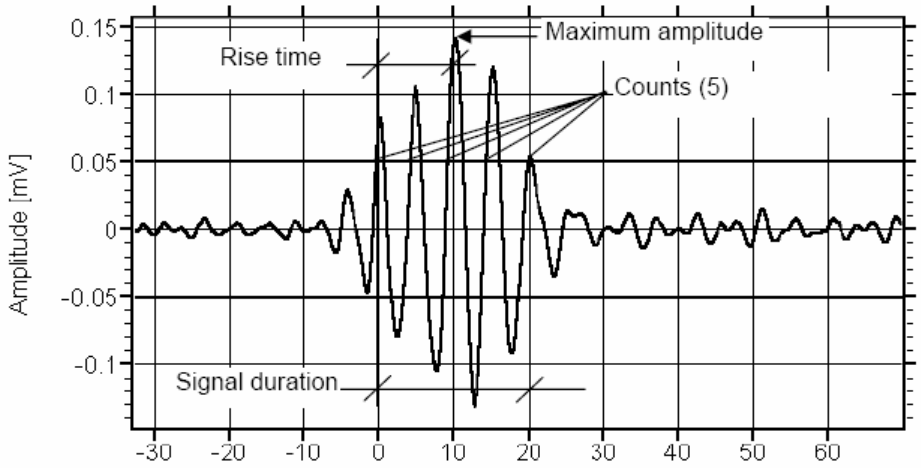

Figure 3.9 - Transient AE signal characteristics

Basically, there are two types of AE signals, transient and continuous signals. With transient signals (bursts), the start and end of the signal deviate clearly from the background noise. With continuous signals, we can see amplitude and frequency variations, however the signal never goes to zero. Useful signals for AE testing are burst type signals, e.g. originating from fracture or crack growth.

The most important parameters of the waveforms are:

- Arrival time (time of first threshold crossing, needed for calculation of crack location)
- Peak amplitude
- Rise-time (time between first threshold crossing and peak amplitude)
- Signal duration (time between first and last threshold crossing)

- Number of threshold crossings (counts)
- Energy (integral of the squared (or absolute) amplitude over time of signal duration)
- RMS (Root Mean Square) of the continuous background noise (before the burst)

The determination of the source location of each event is an essential element of AE testing. The distance difference between source (defect) and different sensors are equal to Arrival Time Difference * Sound Velocity.

In the present work AE system AMSY4 (Vallen-System) was used. It consists of:

- Master unit;
- 4 AE-channels;
- Broadband sensors with a measuring range between 200 and 900 kHz;
- Software package:

  Acquisition 32 – AE+TR data acquisition program;

  VisualAE – visualizes AE results, waveforms and special features (e.g. classification results). It combines filtering, location, clustering, 2D/3D-graphs, TR graphs, listings, calibration table and more.

AE recording was conducted at room temperature for samples after isothermal oxidation at high temperatures, as well as *in-situ* during thermal cycling. The configuration of the AE measurement system is shown schematically in Figure 3.10.

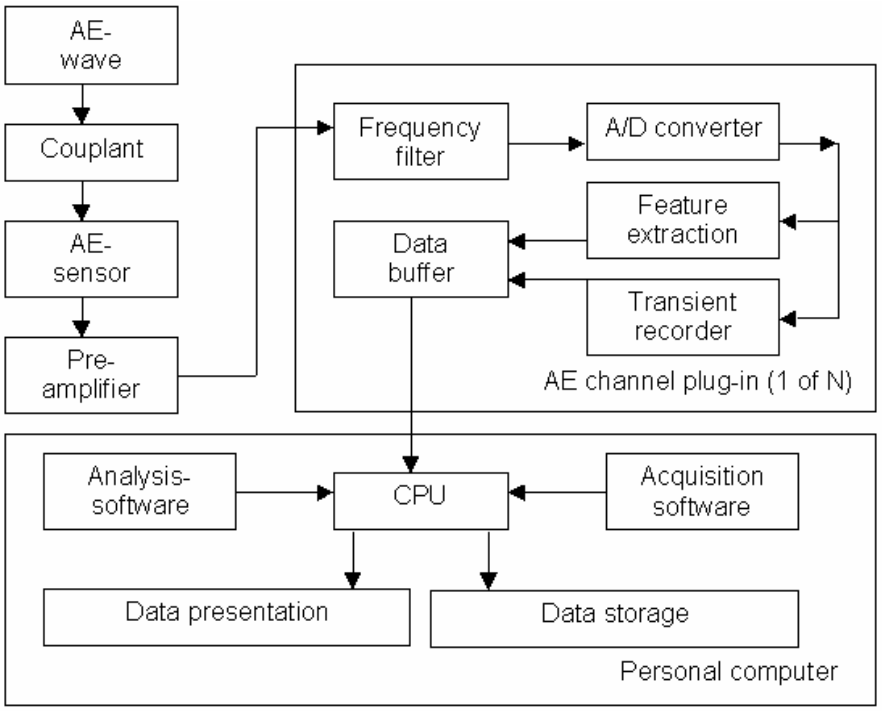

Figure 3.10 - AE measurement system configuration

3.4.2 Infrared Thermography

Infrared measurement and investigation techniques are widely used for the inspection of subsurface defects and features, thermo-physical properties, coating thickness and subsurface structures. During infrared thermo-graphic inspections, there are two approaches that can be used: passive and active. The passive approach is usually used for the investigation of materials that are at different (often higher) temperatures than the ambient, whereas in the case of the active approach an excitation source, such as optical flash lamps, heat lamps, hot or cold air guns, etc., are used with the intention of inducing thermal contrasts.

During transient thermography (active approach), the surface under investigation is pulse heated (time period of heating varying from ms to s) by various heating sources (i.e. flash lamps) and the resulting thermal transient at the surface is monitored using an infrared camera. The duration of the heating pulse depends on the thermal and physical properties of the material, as well as its thickness. The heat flow into the sample is altered in the presence of a subsurface defect or feature, creating a temperature contrast at the surface that is recorded by an infrared system.

Thermography detection was conducted using a ThermaCAM SC 3000 system with Quantium Well Infrared Photodetector (QWIP) that provides image resolution of 320×240 pixels in a spectral range 8-9 μm. The thermal sensitivity was 0.03°C at 30°C, image frequency was 50/60 Hz. Image acquisition and evaluation were supplied by ThermoLab software from T-ZfP.

Figure 3.11 displays a schematic diagram of a transient thermography imaging system.

- Portable PC
- Thermography camera ThermaCAM SC 3000
- 2 flash lamps with IR filters
- Flash generator Avant 1000

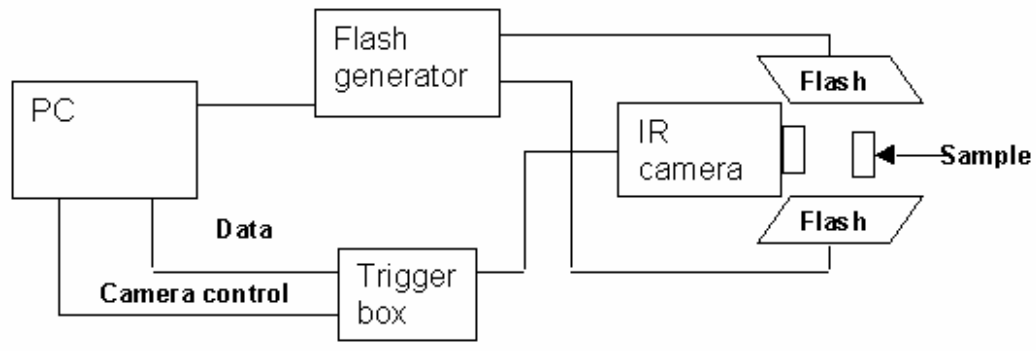

Figure 3.11 - Thermography imaging system configuration

The sample was flash heated using two high-intensity flash lamps and an infrared camera recorded the subsequent thermal transient of its surface. Subsurface defects, such as delamination etc., were revealed as “hot regions” in the thermal images of the surface recorded by the infrared camera during the cooling transient (Figure 3.12.a). The reason for

this is that the surface above the defect cools more slowly than its surroundings because the heat deposited at the surface over the defect becomes trapped between the defect and the surface. It can be clearly seen from the temperature-time curves analysis (Figure 3.12.b) that slower cooling occurred in middle region (points 2, 3, 4) in comparison to regions 1 and 5. This corresponded to areas with delaminated TBC and that are still attached or intact areas, respectively.

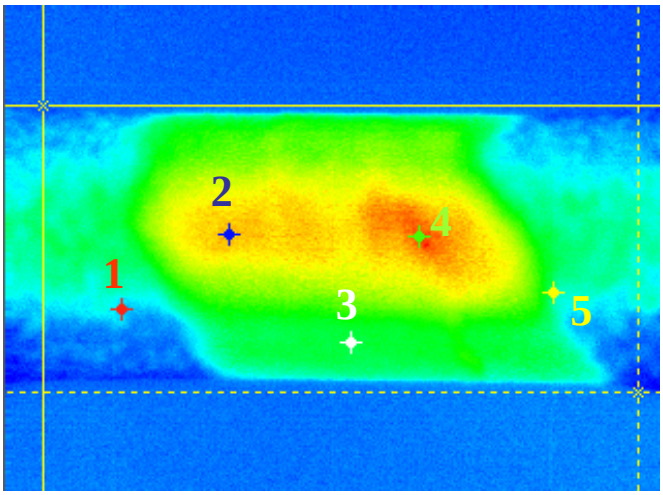

(a)

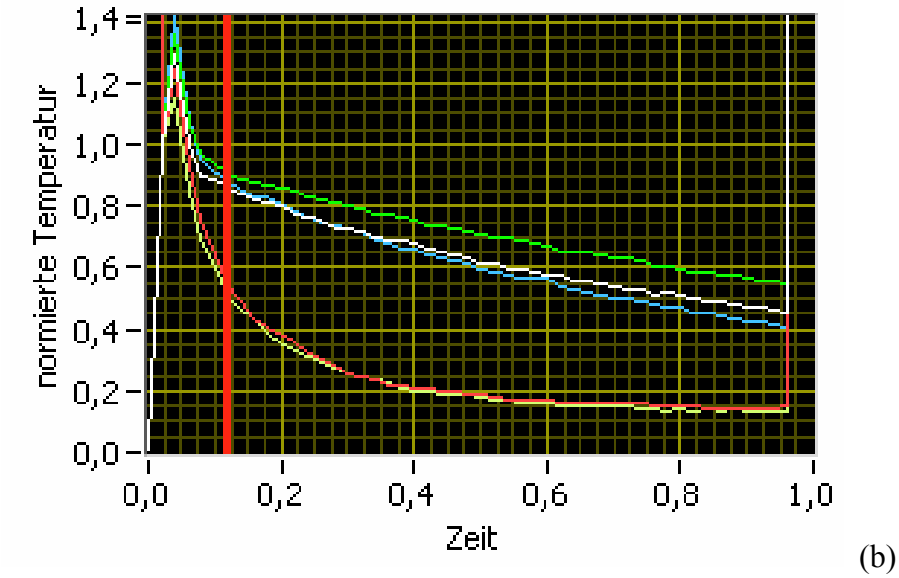

(b)

Figure 3.12 – (a) Example of the IR image and (b)corresponding to points 1-5 temperature-time distribution

4 Aim of investigation

High temperature components in gas turbines experience a complex thermal and mechanical loading during a typical operation cycle. Under base load operating conditions, isothermal exposure at high temperatures is one of the major life limiting factors of the TBCs while under peak loading thermal and thermomechanical fatigue reduce significantly the lifetime of turbine blades and vanes.

It is one of the major aims of the present work to focus not only on one specific single laboratory test, which may reflect and emphasize just one aspect of the complex in-service loading scenario of gas turbine components with thermal barrier coatings, but rather to use a selection of six different types of laboratory tests to determine their respective effect on the kind of damage and the differences in life-time or number of cycles to failure.

The damage and failure behaviour of thermal barrier coatings was of major interest, but the influence of the corrosion protection coating and the TBC on the fatigue failure of the superalloy or rather base material was an additional important aspect of the investigations.

The six types of laboratory tests were interpreted as six different loading profiles, which were divided into the respective load components in order to enable a comparison between them with respect to their influence on damage and failure modes.

Figure 4.1. points out how the load profiles of the six test types were divided into four basic load components, namely:

- HT exposure;
- thermal cycling;
- mechanical cycling;
- temperature gradient.

The assignment of test types or load profiles to a superposition of single load components provided the basis for the analysis of the influence of complex load scenarios on the damage and failure modes of thermal barrier coatings. Furthermore, it classifies which of the degradation parameters and processes was activated by certain load component and helps to get better understanding in their development and influence on the damage.

An isothermal oxidation test (type 1) was therefore interpreted as a single load component test with “high temperature exposure” as the dominating load component. This test or load component activates bond coat oxidation and the associated diffusion processes and phase changes as well as the stiffness increase of the thermal barrier coating, which will be related to a sintering.

A thermal cycling test (type 2), which comprised only heating to T_{max} and cooling to T_{min}, but no dwell-time at high temperature, was also interpreted as a single load component test. In contrast to high temperature exposure, it primarily activates cyclic stresses near the bond coat/TBC interface, which are thermally induced by the mismatch of the thermal expansion coefficients of metallic and ceramic coating. Bond coat oxidation and sintering are reduced to a minimum.

Test type	Load profile	Load components			
		HT exposure	Thermal cycling	Mechanical cycling	T gradient
1	Isothermal oxidation				
2	Thermal cycling				
3	Cyclic oxidation				
4	Cyclic oxidation with temperature gradient				
5	TMF				
6	TMF with dwell time				

Figure 4.1 – Types of laboratory tests and their load components

Cyclic oxidation (type 3) consists therefore of the two load components “thermal cycling” and “high temperature exposure” and test type 4, which referred to as cyclic oxidation with temperature gradient, comprises three basic load components.

A regular TMF test (type 5) without high temperature exposure comprises the two components “thermal cycling” and “mechanical cycling”, i.e. cyclic mechanical strains. It activates thermal stresses near the TGO and causes a superposition of additional mechanical stresses, which, for instance, affect the in-phase stress component in the coating near the TGO.

In the case of out-of-phase TMF loading it may cause also fatigue cracks in the bond coat, which than may lead to base material failure. It comprises no dwell-time at high-temperature, so that bond coat oxidation and sintering are reduced to a minimum in comparison to a cyclic oxidation test, for instance.

Test type 6 is a TMF test with dwell-time, which comprises additionally high temperature exposure and thus also activates bond coat oxidation and sintering. It should be emphasized that this test type may also be interpreted as a cyclic oxidation test with additionally superimposed mechanical strains.

On the basis of this approach, which divides the test types into basic load components, it becomes clear that it is not cyclic oxidation and a regular TMF test, but cyclic oxidation and

TMF with dwell-time that should be compared, when the question on the additional influence of TMF strains on damage and failure is being addressed. A comparison between cyclic oxidation and regular TMF would comprise the damage of two parameters, namely “switching off” high temperature exposure and “switching on” mechanical strains, the effects of which would not be separable afterwards.

Additionally compressive deformation experiments were carried out on free standing plasma-sprayed TBCs consisting of zirconia doped with 7-8 wt% yttria with the aim of generating a deformation data set for plasma-sprayed TBCs with realistic structure and investigating the corresponding microstructural changes.

5 Results and discussion

5.1 As-received state

In Figure 5.1 the typical microstructure of APS TBC coated components in the as-received state after standard heat treatment is represented. The interface between bond coat and TBC had a roughness amplitude of R_a = 7-8 µm to provide better mechanical adhesion (clamping) of the ceramic top coating. The thickness of the ceramic top coat and the bond coat was about 300±20 µm and 150±30 µm, respectively.

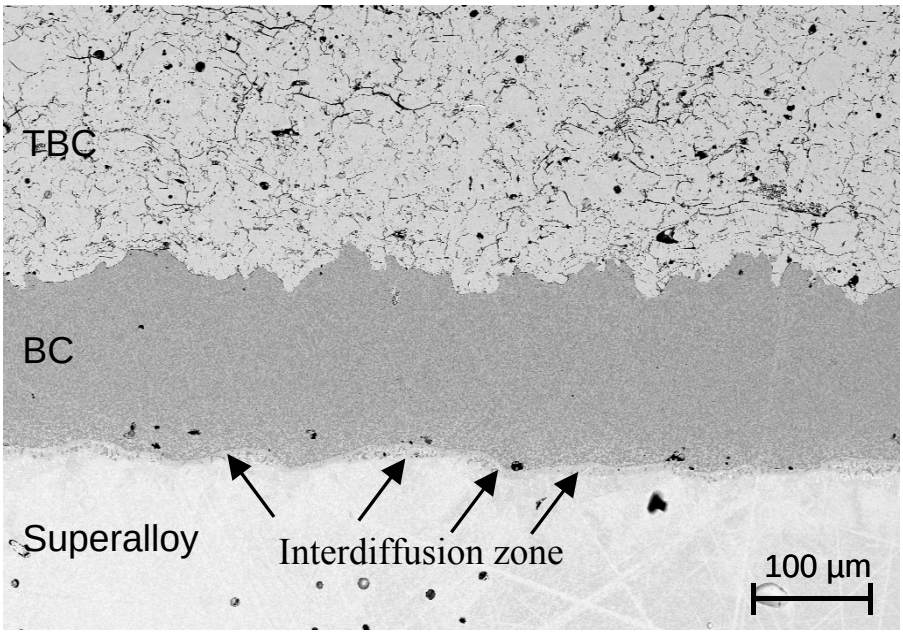

Figure 5.1 - SEM image of as received TBC microstructure in bond coat region

More detailed images of the interface between TBC and BC, as well as between BC and substrate are shown in Figure 5.2. After plasma spraying, a thin oxide layer (TGO) of about 0.5µm in thickness was formed on the surface of the bond coat (Figure 5.2.a). At the interface between BC and substrate, an interdiffusion zone (IZ) with an average thickness of about 15 µm was formed, mostly below interfacial peaks (Figure 5.2.b).

The interfacial region between BC and base material can be divided into the following zones:

I. Three-phase BC (β, γ, and α), predominantly unaffected
II. Interdiffusion zone:
    a - β-depleted zone in BC;
    b - affected substrate zone
III. Unaffected single crystal substrate

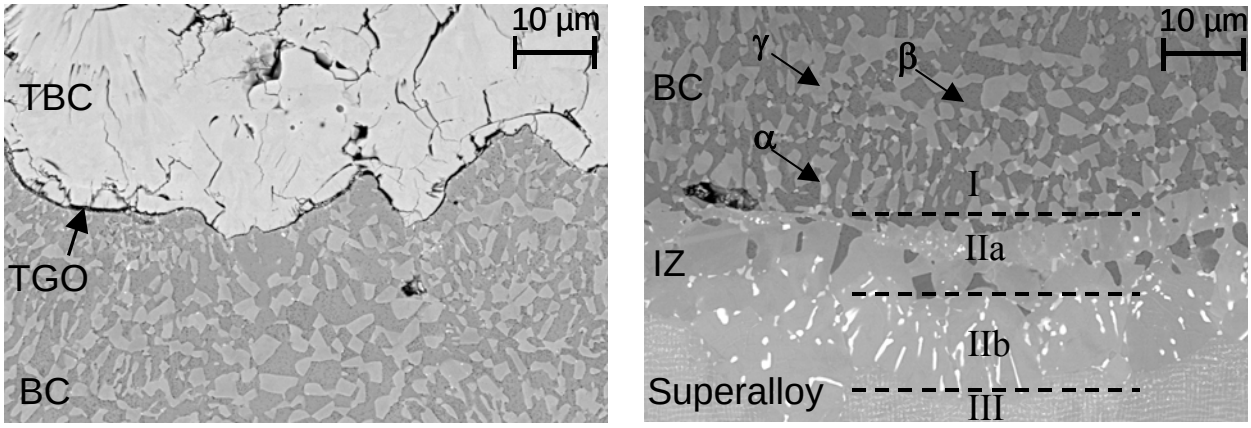

(a) (b)

Figure 5.2 - SEM images of TBC microstructure: a) TBC / BC interface; b) BC / base material interface, zones I to III explained in the text

Further analysis of the interdiffusion zone as well as its development under different load profiles will be discussed in the sections that follow.

5.2 Thermal loading

Failure modes and damage mechanisms of TBC systems under thermal loading were investigated using isothermal and cyclic load profiles. Under cyclic conditions, the superposition of thermal cycling and isothermal exposure, as well as an additional temperature gradients were studied. The test parameters are summarized in Table 5.1.

Table 5.1 - Summary of test parameters and experimental results

Loading	ΔT, °C	N_f	t_f, h
Isothermal exposure	1050	1	4490
Thermal cycling	60 - 1050	>23500	---
Cyclic oxidation	60 - 1050	700	1400
	350 - 1050	1440	2880
Cyclic oxidation with temperature gradient	60 - 1050 (BC) - 1150 (TBC)	56	112

5.2.1 Isothermal oxidation

A series of 22 isothermal oxidation experiments at 1050°C for up to 4500 hours were carried out. The list of specimens tested is given in Table 5.2.

Table 5.2 – Isothermal exposure tests at 1050°C

Sample No.	**1**	**2**	**3**	**4**	**5**	**6**	**7**
Time, h	96	190	290	380	480	570	670

Sample No.	**8**	**9**	**10**	**11**	**12**	**13**	**14**
Time, h	770	960	1150	1340	1540	1730	1920

Sample No.	**15**	**16**	**17**	**18**	**19**	**20**	**21**	**22**
Time, h	2210	2400	2590	2780	3070	3360	3840	4490

In order to get additional information about damage evolution, samples were connected to the acoustic emission (AE) device up to 400 hours after high temperature exposure and cooling down to the ambient temperature. Infrared pictures were taken before and after AE testing. Then the specimens were cut and metallografically prepared for microstructural investigation. The evolution of TGO thickness as well as microcrack distribution (length, number) was systematically determined using SEM pictures (8 pictures with the same magnification for each sample), which resulted in an analysis of 0.8 mm of the axial specimen length. For measuring cracks longer than 800 μm, pictures with lower magnification were used.

5.2.1.1 Damage accumulation at ambient temperature

After the specimens had cooled down from 1050°C to ambient temperature generally no macroscopic spallation was observed, but IR images (see section 3.4.2 about IR thermography) revealed slight delaminations starting from the edges (Figure 5.3.a,c,e, red zones). In the case of 1720 hours of exposure, the comparison of IR images directly after cooling and over 400 hours at room temperature did not reveal significant changes (Figure 5.3.a,b). In contrast, after 3840 hours at 1050°C, the delaminated zones at the edges increased further during 400 hours at RT (Figure 5.3.c,d). Finally, complete TBC spallation occurred after 300 hours at ambient temperature for the specimen exposed for 4490 h at 1050°C (Figure 5.3.f).

The IR images document that the damage of the TBCs developed and accumulated without any further external loading at room temperature.

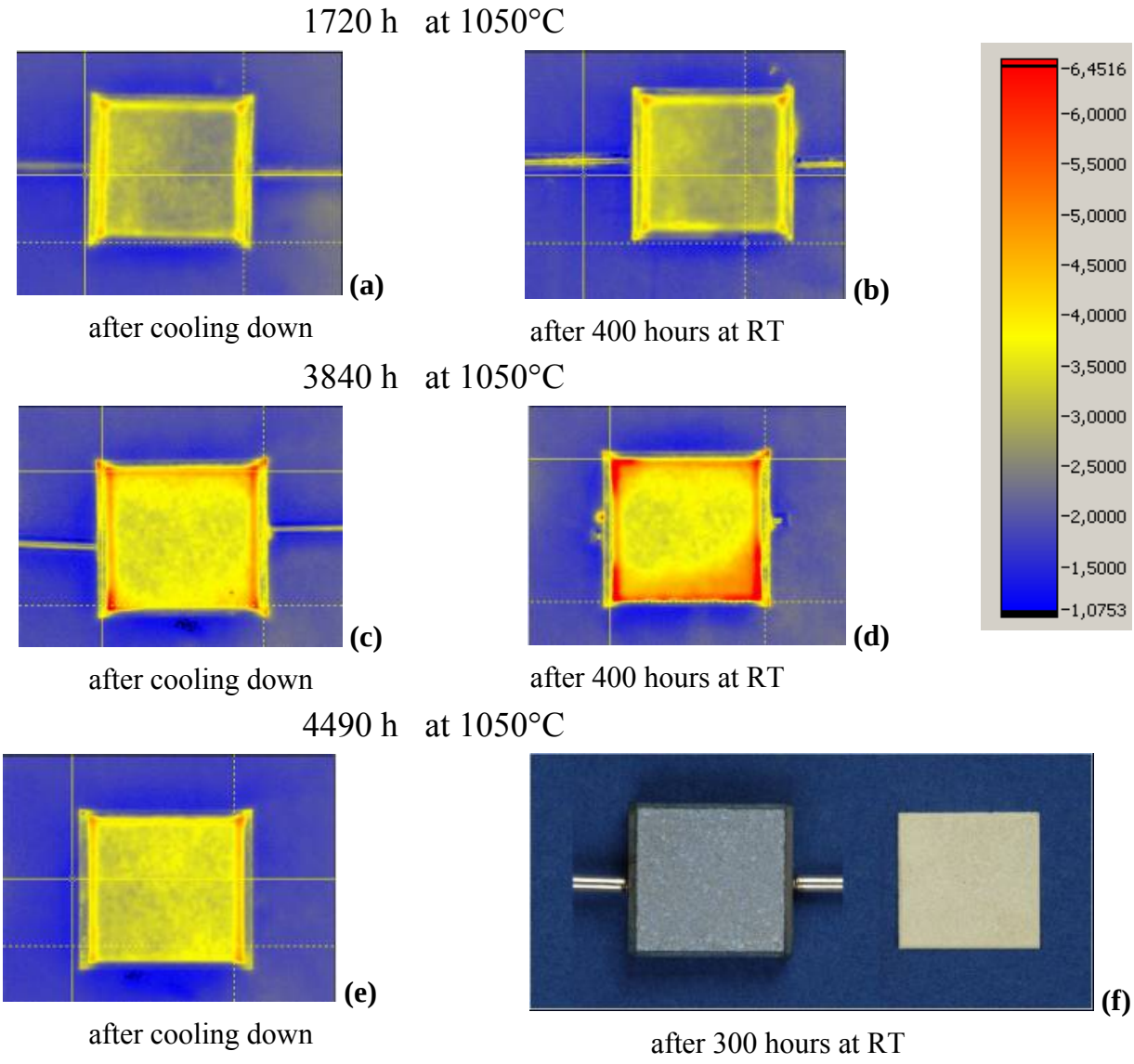

Figure 5.3 – The effect of damage accumulation at ambient temperature for TBC specimens after high temperature exposure at 1050°C illustrated by:
a-d) thermographical images; e) macro image of the spalled coating

The “cold spallation” or “desktop effect” displayed in Figure 5.3.e and f and which is well known for EB-PVD coatings [106], was also observed here for APS thermal barrier coatings. Damage accumulation and “cold spallation” are assumed to be due to cooling stresses, which generally result from a combination of thermal mismatch and TGO growth. Perhaps the humidity in the ambient air plays a role in this process. This effect is sometimes discussed, but has not been investigated systematically as yet.

The observation of damage accumulation at low or ambient temperatures was supported additionally by acoustic emission. The crack formation and propagation associated with strain energy release was detected by acoustic emission measurements. Figure 5.4 shows AE data recorded at room temperature for up to 400 hours after different high temperature exposure times.

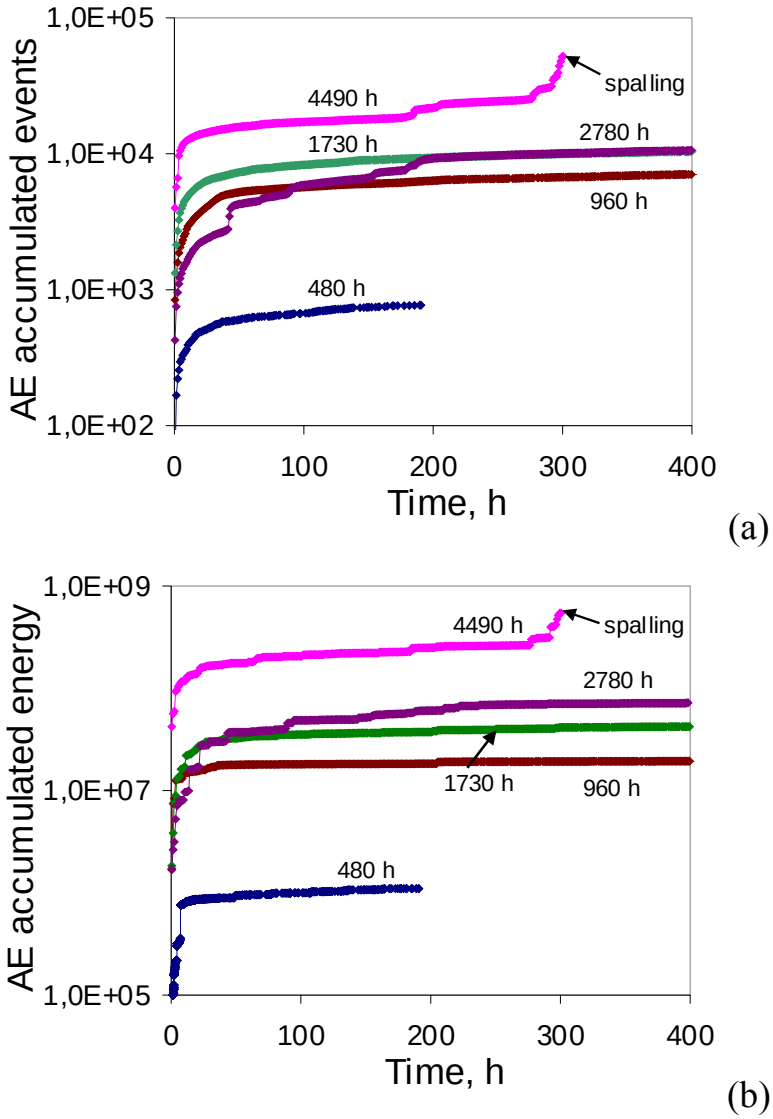

Figure 5.4– AE data recorded at RT for the specimens exposed at 1050°C: a) accumulated acoustic events; b) accumulated acoustic energy

The curves display the accumulated number of acoustic events (left) and the accumulated amount of acoustic energy (see section 3.4.1 about acoustic emission) as a function of time at room temperature. Both types of acoustic emission parameters increased continuously with increasing time at room temperature, indicating clearly the accumulation of damage in the TBC specimens at room temperature. Both parameters showed a rapid increase directly after cooling down and a more moderate increase after about 50 hours. This reflects a comparably high initial damage rate after cooling down, which becomes significantly smaller after a certain time. It reveals that the majority of damage is generated in the first 50 hours after cooling down. The accumulated acoustic events, as well as the accumulated acoustic energy, revealed at some points a stepwise increase in the case of those specimens, that were exposed for 2780 and 4490 hours. For shorter exposure times, the shape of the curves was more uniform. The biggest stepwise increase was observed for the specimen, which was exposed for 4490 hours, namely after 300 hours at room temperature. This increase is associated with the complete spallation of the TBC from the base material.

Furthermore, the absolute values of accumulated events and accumulated energy also increased with increasing exposure times, i.e. at equal times after cooling down the values were higher for longer exposure times. This effect is presented in Figure 5.5, where the accumulated acoustic events and the accumulated acoustic energy are plotted as a function of high temperature exposure time for 50 hours and 200 hours after cooling down. For instance, the accumulated energy was two orders of magnitude higher after 4490 h of high temperature exposure than after 480 h.

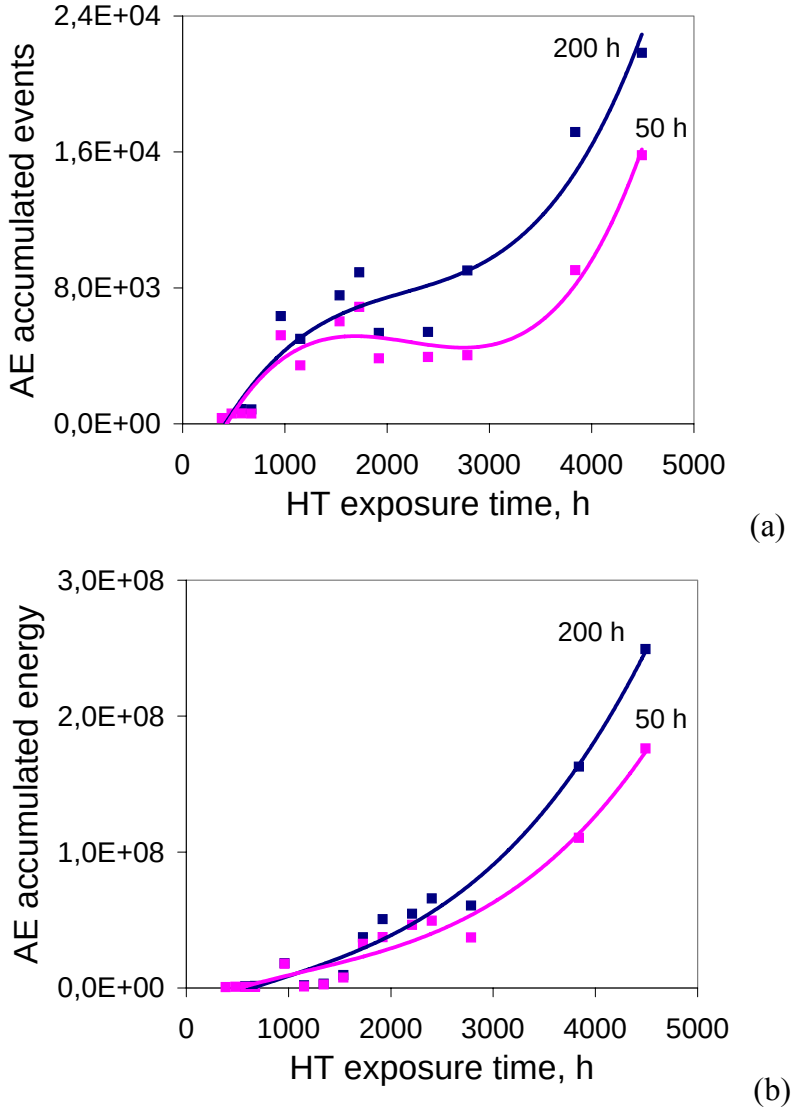

Figure 5.5– AE data recorded at RT for the specimens exposed at 1050°C: a) accumulated acoustic events; b) accumulated acoustic energy

The observed damage accumulation at ambient temperature has a significant effect on the understanding of damage evolution of plasma-sprayed TBCs with respect to practical consequences for the service operation. The results imply:

i) that crack formation and crack propagation, which degrades the mechanical integrity of the TBC composite at the metal/ceramic interface during and after cooling is not instantaneous, but a process, which develops with time;

ii) that this time-dependent damage process, which develops without any further external temperature or stress loading is perhaps influenced by environmental boundary conditions, such as humidity;

iii) that the lifetime of a TBC coated gas turbine component is consumed at room temperature, while the service operation of the gas turbine is interrupted.

The last point has a direct effect on the operation mode, particularly for peak load operation of a gas turbine. The longer the dwell time is at lower temperatures, the more damage that is accumulated and the more lifetime that is consumed.

5.2.1.2 Microstructural observations

Microstructural observations were conducted on polished cross-sections as a function of exposure time. Figures 5.6, 5.8 and 5.9 show some examples of the microstructural changes in the specimens after 96, 960, 1920, 3070, 3840 and 4490 hours of oxidation.

Figure 5.6 points out the TGO development with a lower and higher magnification. The TGO consists mainly of alumina, but during the initial oxidation stages, the formation of less stable oxides, such as (Ni, Co, Cr) oxides was observed (Figure 5.6.c,d). SEM EDX mappings shown in Figure 5.7 confirm presence of Ni, Co and Cr oxides at TBC/TGO interface.

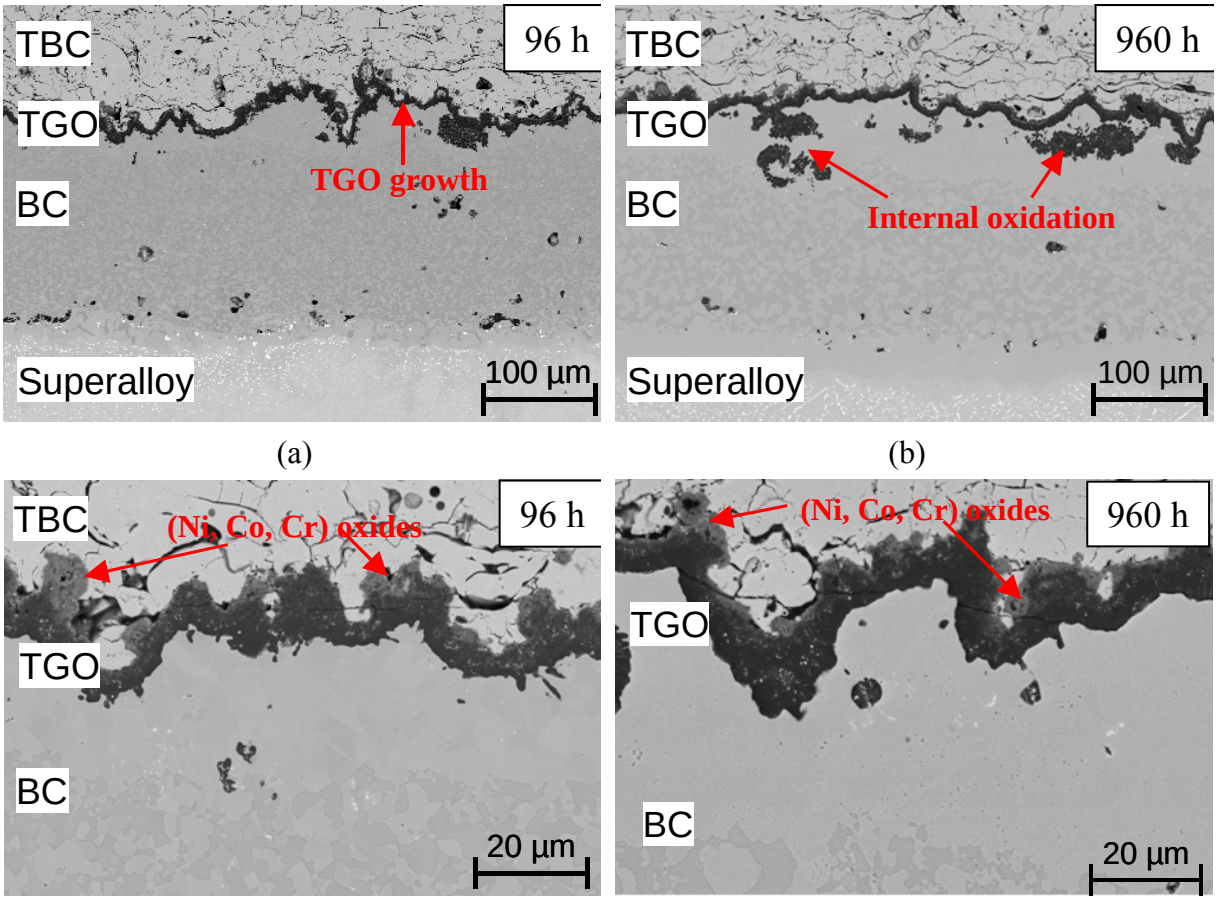

Figure 5.6 – Microstructure evolution of TGO growth in TBC specimens exposed at 1050°C

During further high temperature exposure, mainly alumina growth took place, whereas amount of other oxides did not change. The TGO thickness was not uniform along the interface. For instance, protrusions, related to reactive element (Y) containing internal oxides, were present and led to local differences in scale thickness. The protrusions developed by rapidly transporting oxygen through the RE(Y) - containing oxides and its reaction with aluminium in the alloy. They did not appear before 960 hours of exposure at 1050°C (see element distribution in Figure 5.7 made by EDX). However, a strong correlation between internal oxidation and exposure time was not observed.

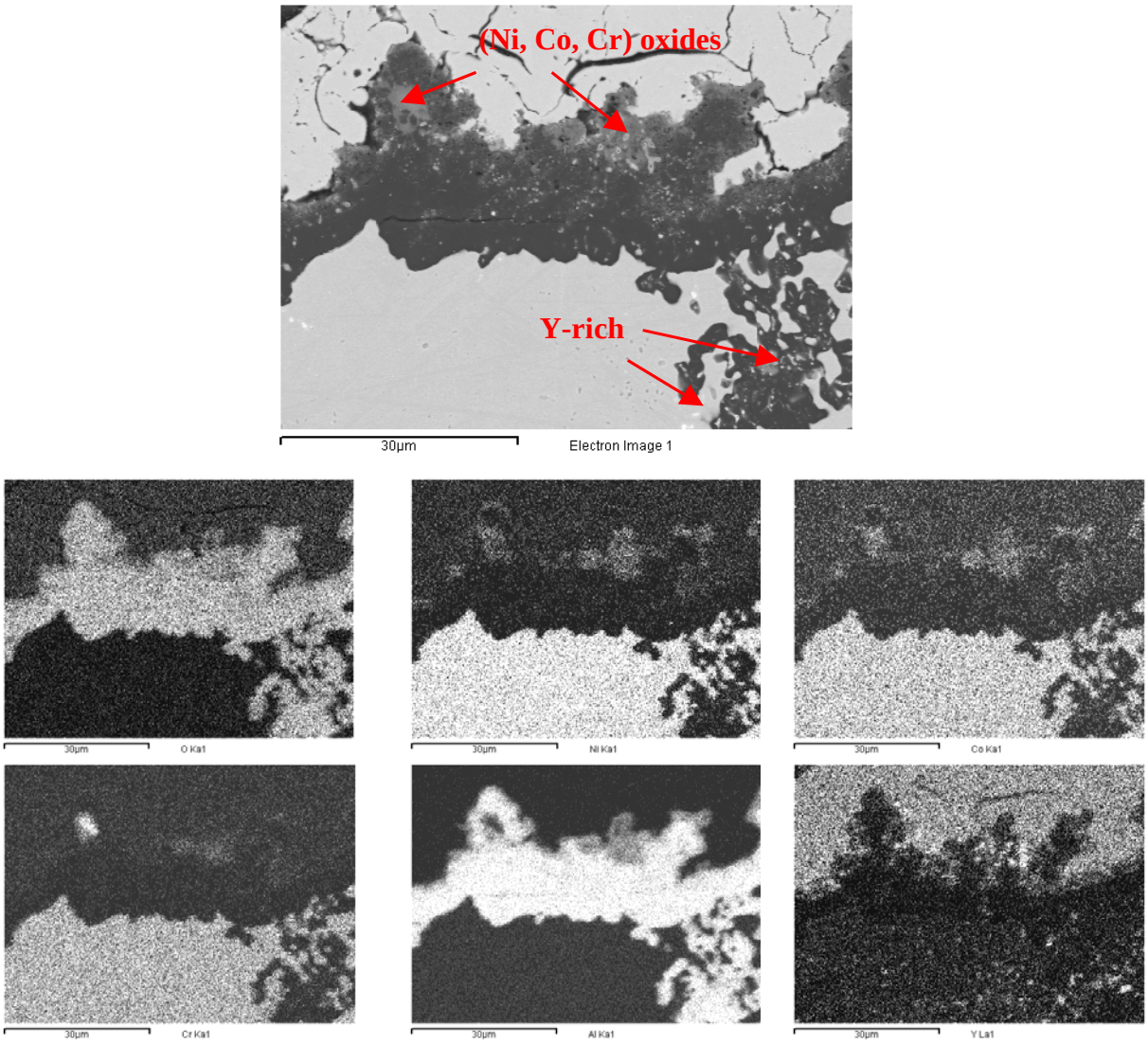

Figure 5.7– EDX mapping for different elements in TGO after 960 hours of exposure at 1050°C. The bright zones indicate the distribution of the respective elements

TGO growth was associated with Al consumption, mainly from Al-rich β-phase in BC. Another β-phase depletion zone in BC was developed close to BC/base material interface because of interdiffusion processes (Figure 5.8.a). Complete β-NiAl phase depletion occurred after ca. 3000 hours of high temperature exposure at 1050°C (Figure 5.8.b).

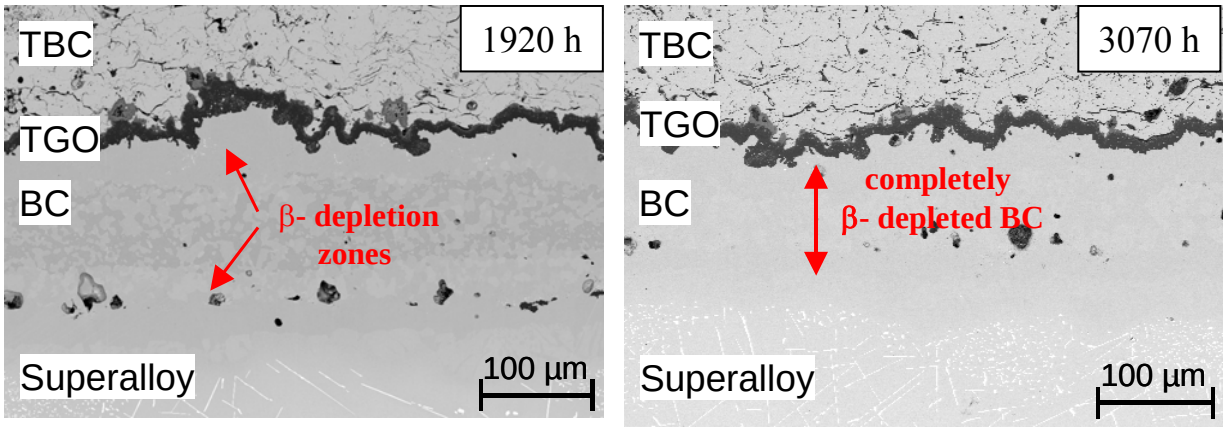

(a) (b)

Figure 5.8 – Depletion of β-NiAl in BC under high temperature exposure at 1050°C

Moreover, after longer exposure times (> 3000 hours) delamination cracks were observed propagating at the TBC/BC interface (Figure 5.9.a). After critical Al-depletion, alumina is not able to form anymore. This led to the development of less protective oxides and quicker penetration of internal oxidation through the thickness of the coating (Figure 5.9.b), which in turn led to coating spallation.

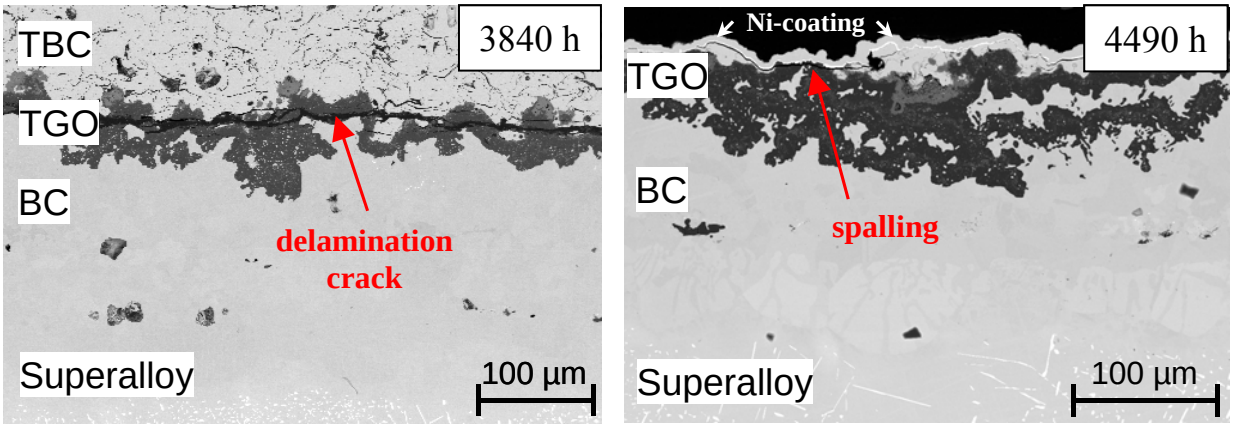

(a) (b)

Figure 5.9 – Delamination crack propagation after high temperature exposure at 1050°C

The delamination crack is propagated partly in the TGO and partly in the TBC, which leads to a so-called “black-and-white” failure.

Examination of the fracture surfaces after spallation of the TBC revealed the presence of (Ni, Co, Cr)-oxides, which can be responsible for TBC failure. In Figure 5.10, the white, dark grey and light grey regions correspond to the YSZ TBC coating, Al_2O_3-TGO and (Ni, Co, Cr)-oxides, respectively.

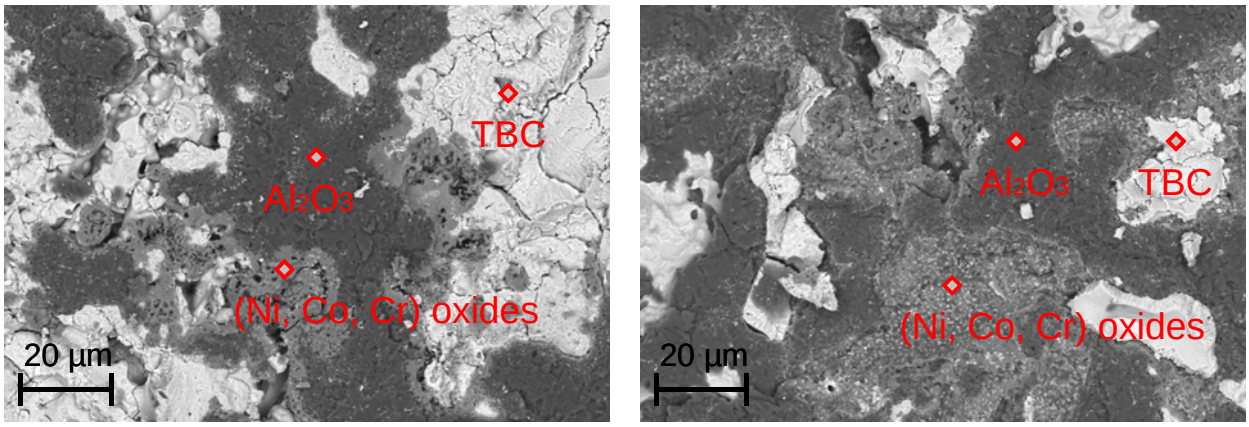

(a) (b)

Figure 5.10 – SEM images of fracture surfaces after TBC spallation: a) from the top surface of BC, b) from the bottom surface of spalled YSZ

5.2.1.3 Damage evolution

In order to quantify the damage evolution near the TGO, particularly the microcrack evolution, a series of 8 SEM images with identical magnification was selected for isothermal oxidation tests at 1050°C (see Table 5.2, p.46). The exposure times ranged from 96 hours to 4490 hours, i.e. from 2% of lifetime to final failure. The number of oxidation tests included in the investigations was 22 in total, therefore the damage evolution was characterized by 22 measuring points along the life span. The length of each microcrack was measured. The results comprise the statistical number distribution of microcracks over their length, i.e. they comprise information on how many cracks were formed with which length. Furthermore the results include the evolution of the mean crack length and the evolution of the longest crack. Since each series of images covers a constant length of 0.8 mm of the axial specimen length in total, the number of cracks may also be considered as a crack density. Cracks that were longer than 0.8 mm were measured with additional images of lower magnification. In addition to the microcracks, the TGO thickness was measured for each exposure time. The measurements were carried out by means of quantitative image analysis.

Figure 5.11 shows snapshots of the damage evolution for six different exposure times at 1050°C. Cracks initiated already after 96 hours of high temperature exposure, mainly at the TBC/TGO interface. Some of the pre-existing cracks within the TBC close to the TGO were opened further (Figure 5.11.a,b). After longer times (>1700 hours) cracking within the TGO as well as at TGO/BC interface occurred, thus the main crack path shifted towards the TGO (Figure 5.11.c,d). Further exposure at 1050°C (>2500 hours) led to the linking of individual cracks and the formation of macroscopic cracks (Figure 5.11.e,f).

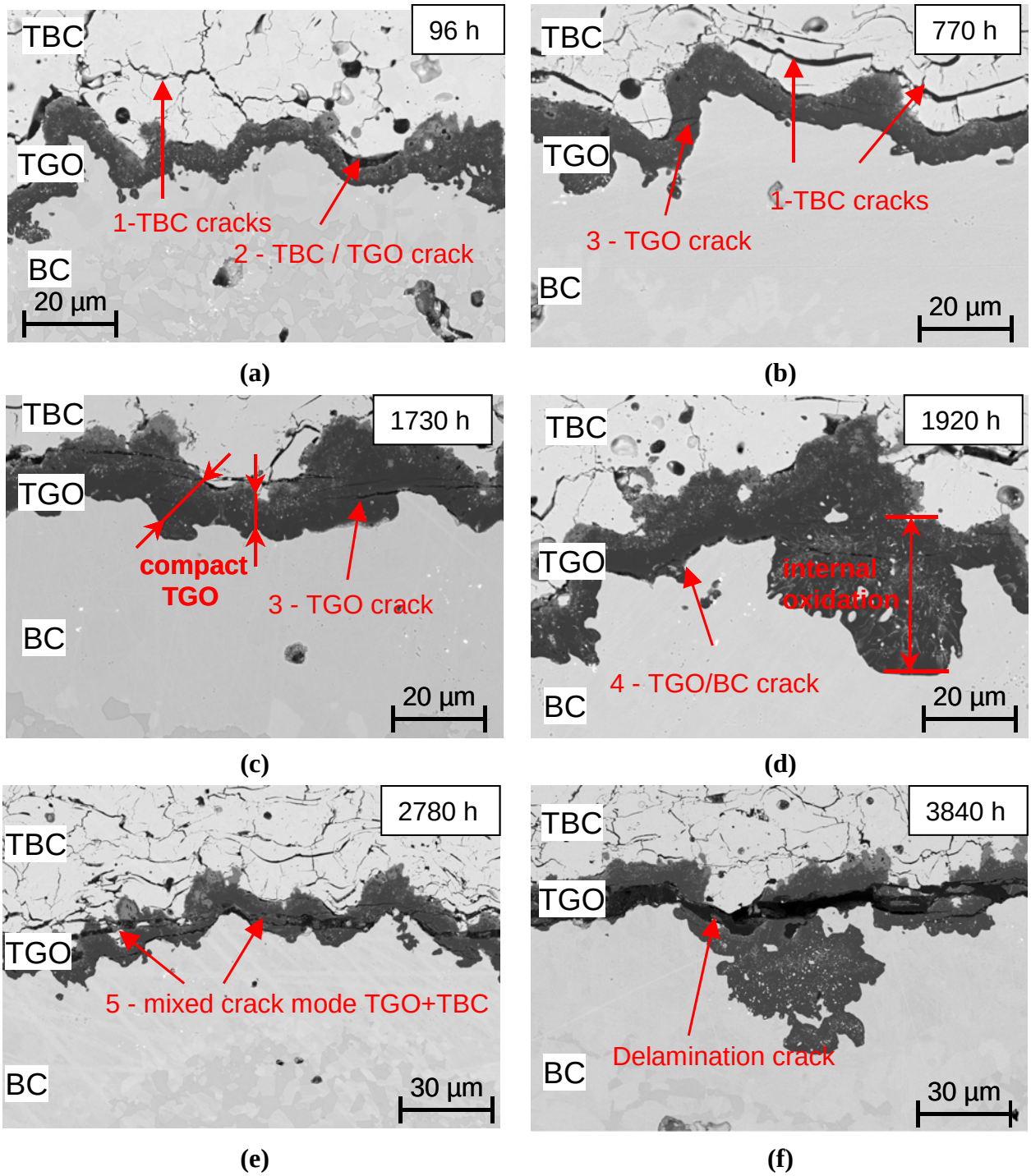

Figure 5.11 – Selected SEM images showing damage evolution in the plasma-sprayed TBC with increasing exposure time at 1050°C

The following crack types were distinguished after detailed examination of sample cross-sections (see Figure 5.11.):

1 - cracks within the topcoat (TBC);
2 - separations between the TBC and the TGO (TGO / TBC);
3 - cracks running across the TGO (TGO);
4 - separations between the BC and the TGO (TGO / BC);
5 - mixed cracks propagating partly in TBC, partly in TGO (TGO+TBC).

The number of cracks as a function of their length (number distribution) is shown in Figure 5.12.a for all microcracks observed after 580 hours of exposure time. The bar graph is generated by counting the number of cracks, which belong to a pre-defined crack length interval of 1 µm, and by plotting the respective number of cracks for each interval as bars along the crack length axis. The bar distribution was then represented by adjusting a statistical Gaussian distribution function to obtain smooth and comparable correlations. Figure 5.12.b shows four distribution functions for different exposure times, which contain additional information about the evolution of the population of microcracks. The mean crack length, which is defined as the crack length at the peak of the distribution, increased only slightly from 10µm to 12 µm between 580 hours and 1730 hours of exposure time. In contrast, the number, or number density increased by a factor of 3.5.

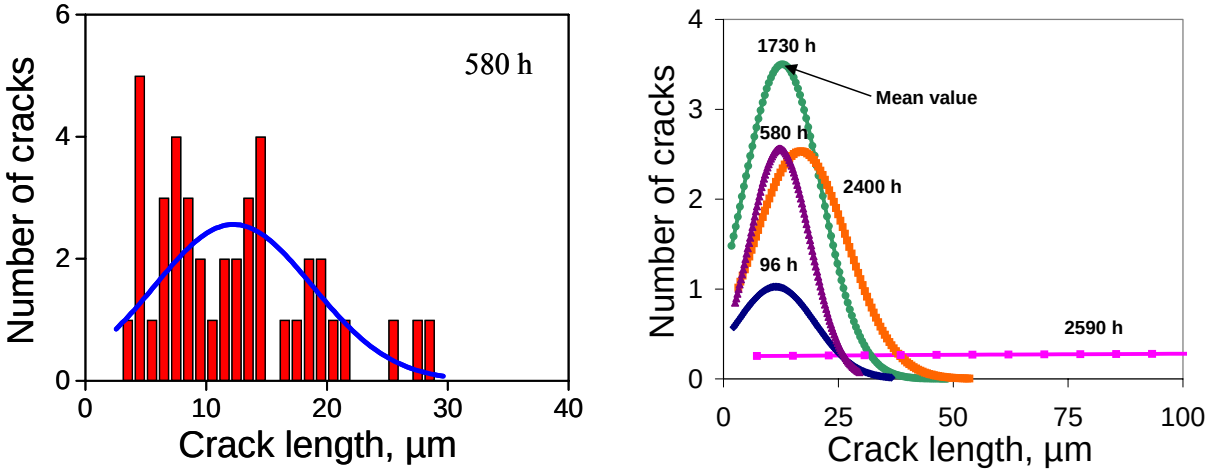

Figure 5.12 – Development of the mean crack length as a function of exposure time at 1050°C: a) example of crack length measurements for specimen after 580 hours of exposure time with a Gaussian distribution function, b) distributions for different exposure times with a mean value at the maximum

Thus, during the first 1800 hours of exposure time microcracks were increasingly formed, but they did not grow during this time. With further exposure, the number density started to decrease while the mean crack length increased up to 18 µm after 2400 hours. After longer times (> ca 2500 hours), the mean crack length reached several hundred µm by linking of individual microcracks, therefore number of cracks decreased drastically.

The mean crack length as a function of exposure time at 1050°C up to 3840 hours of oxidation is presented in Figure 5.13. It can be clearly seen that only cracks of type 5, i.e. those, which propagate through TGO and TBC, reached macroscopic values while the mean length of other crack types remain limited in their size. On the one hand, it shows that the failure crack path under oxidation conditions is located partly in the TGO and partly in the TBC, and here predominantly over roughness valleys. On the other hand, it can be calculated that the remaining microcracks do not contribute directly to the final spallation.

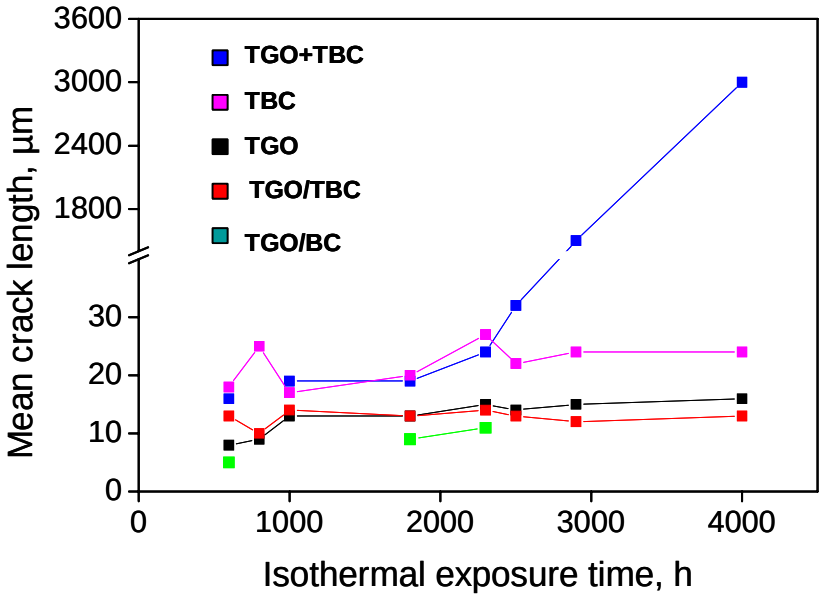

Figure 5.13 - Development of different type of microcracks as a function of exposure time

For further discussion only mixed crack type (type 5, TGO+TBC) is considered and the focus is put on the maximum crack length, because the longest crack causes failure. In Figure 5.14 the maximum crack length, as well as the number of cracks, are represented as a function of exposure time.

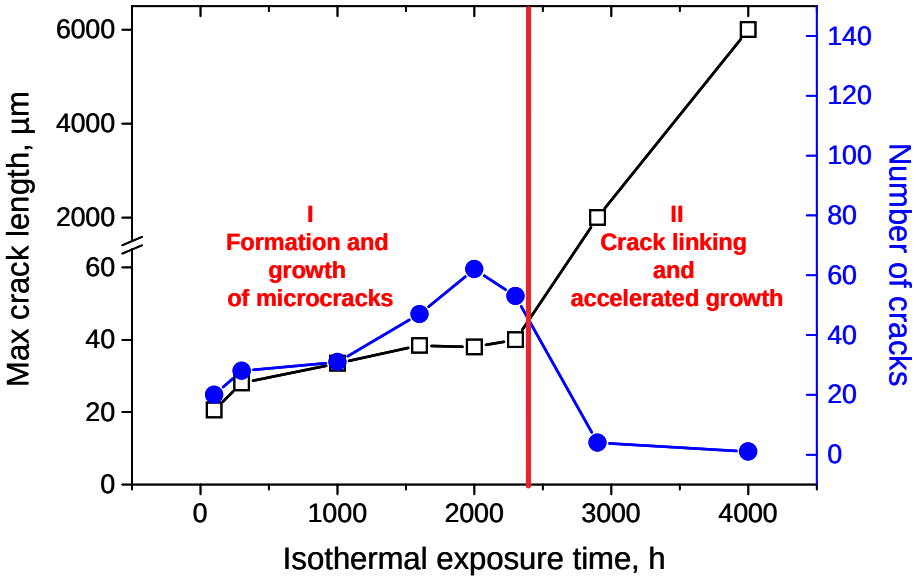

Figure 5.14 - Maximum crack length and number of TBC / TGO cracks as a function of exposure time

The crack length was below 40 µm up to 2500 hours of exposure time and then cracks started to link and propagate up to macroscopic size while the crack number was decreased. In other words, the process of crack initiation and crack growth can be divided into two phases:

1. Formation and growth of microcracks: the initiation of microcracks and their initial growth was governed by TGO growth and processes related to bond coat oxidation. Microcracks mainly localized in the TGO as well as at its interfaces and restricted in length (below 40 µm).
2. Crack linking and accelerated crack growth: crack propagation and penetration into the TBC (stable or subcritical crack growth) occurred. This resulted in spallation failure of TBC with delamination crack path partly in TBC, partly in TGO.

Results of TGO thickness (compact TGO as well as internal oxidation) measurements as a function of exposure time at 1050°C are represented in Figure 5.15. The compact TGO thickness reached 5 µm after about 200 hours, 10 µm after 2500 hours and was ca. 13 µm for the specimen, which showed complete TBC spallation after 4490 hours. The depth of internal oxidation tended to increase with increasing oxidation time. It was about 20 µm after 300 hours and 70-80 µm after 4000 hours, but large scatter could be observed in between. Thus, the specimens exposed for 1000 hours and for 1700 hours had an internal oxidation depth of about 100 µm.

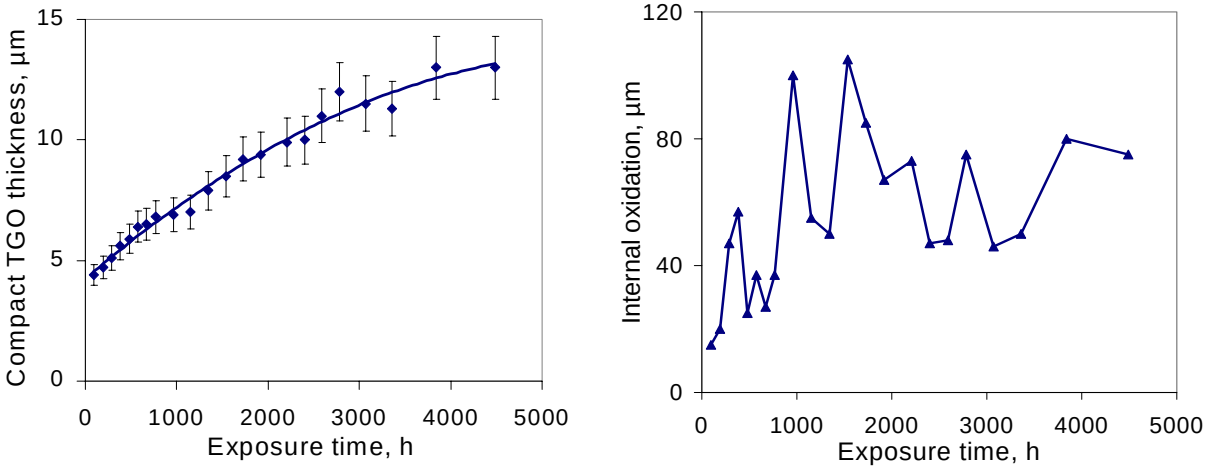

(a) (b)

Figure 5.15 - TGO thickness as a function of exposure time at 1050°C: a) compact TGO, b) internal oxidation

In order to find reasons for the relatively large scatter of internal oxidation, it was plotted in comparison to the bond coat thickness, which also showed relatively large scatter between 110 µm and 200 µm. The mean bond coat thickness was ca. 150µm.

Figure 5.16 displays both the bond coat thickness of each of the exposed specimens and the depth of internal oxidation. It shows a clear correlation between a thicker bond coat and more or deeper internal oxidation. The correlation was independent from the exposure time itself at a first glance. This effect can be noticed more or less throughout the entire exposure time (300-4490 hours).

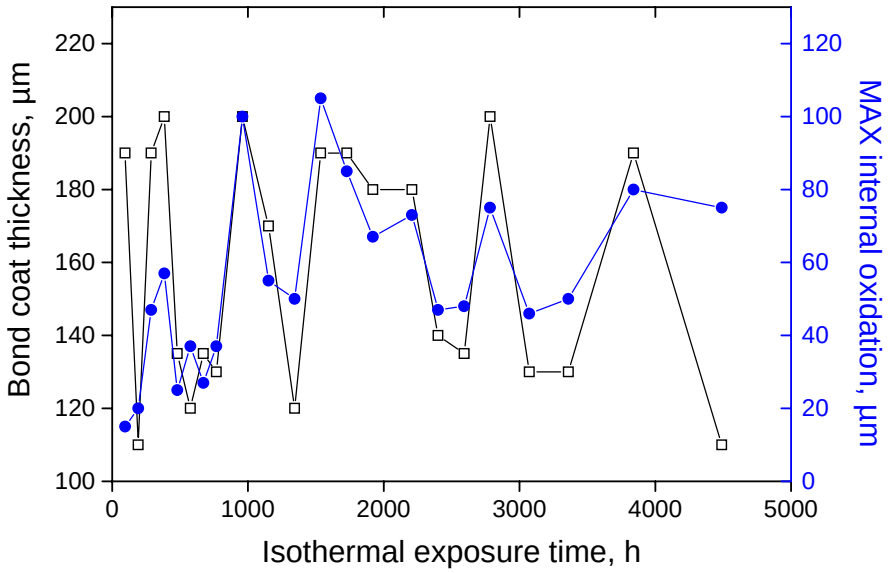

Figure 5.16 - Correlation between maximum internal oxidation depth and variation in bond coat thickness of TBC specimens

Taking into account crack growth kinetics and compact TGO, the critical TGO thickness of about 10 µm was found above that the accelerated crack growth occurred (Figure 5.17).

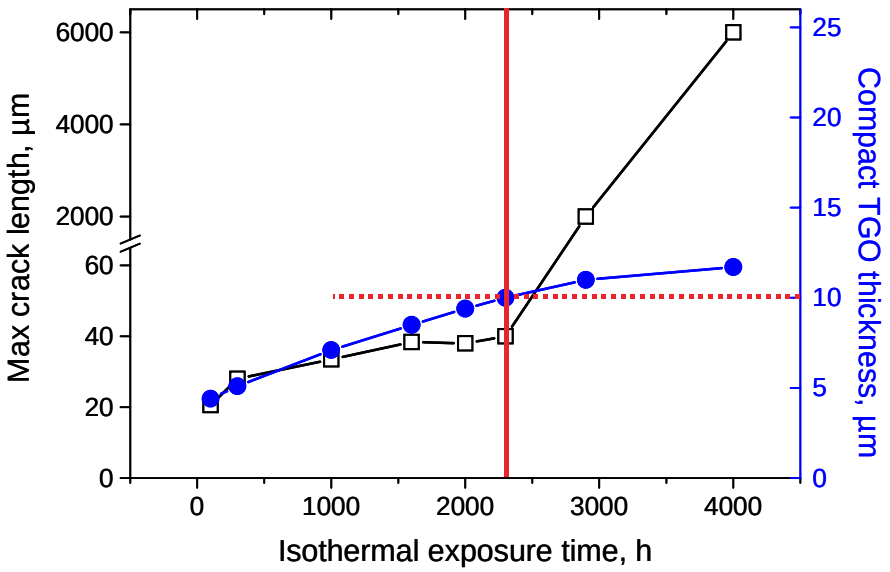

Figure 5.17 - Maximum crack length and TGO thickness as a function of exposure time

Thus the crack growth vs. time curves always allowed the process to be separated into two stages as shown in Figure 5.14 and Figure 5.17:

1 - damage incubation phase with crack length below 40 µm and TGO thickness below approximately 8-10 µm;

2 - crack growth phase when cracks initiated in the TGO (thickness >10 µm) penetrate the TBC and propagate over macroscopic distances.

5.2.2 *Thermal cycling*

Thermal cycling tests were carried out in order to compare pure isothermal tests as the case with minimum amount of cyclic load steps (one heating step, one cooling step) with pure cycling as the load case with a minimum high temperature exposure. The comparison shall reveal, whether high temperature exposure and thermal cycling activate different damage modes with respect to the final failure crack path. The thermal cycle consisted of 8 minutes of heating up to 1050°C and 8 minutes of forced air-cooling followed by a 1-minute dwell time at minimum temperature of 60°C. The experiment was carried out in an IR furnace (see section 3.2.2) for up to 23500 cycles. No macroscopic spallation was observed after the last load cycle. Thermographical analysis also revealed no delamination at the TBC/BC interface (Figure 5.18).

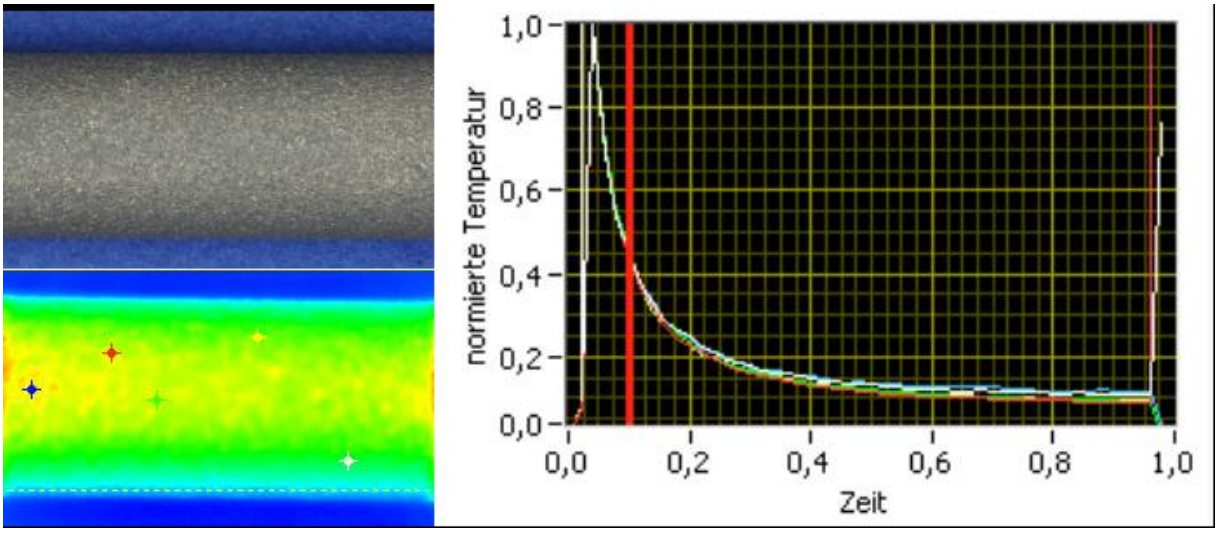

Figure 5.18 – Macro and thermographical images (left) and temperature-time curves of impulse thermography (right) for TBC specimen after 23500 thermal cycles (60-1050°C). Five measuring points (blue, red, green, yellow, white) showed normal temperature decay curves, i.e. no clear indications for larger delamination

However, the examination of the cross-section in longitudinal direction revealed a long delamination crack with a length of about 3 mm in the TBC close to the TGO (Figure 5.19), which propagated parallel to the TBC/TGO interface.

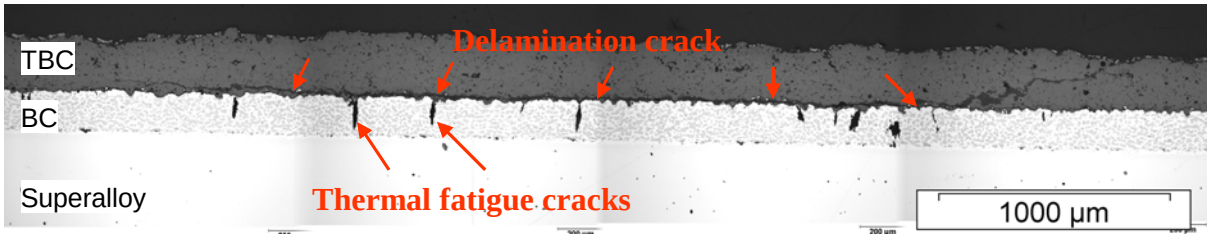

Figure 5.19 – Image of TBC length-section after 23500 thermal cycles: delamination crack along TBC/TGO interface, thermal fatigue cracks in BC

In addition to the delamination crack, thermal fatigue cracks were observed in BC with lengths of less than 100 µm. A more detailed view of the TBC/BC interface is shown in Figure 5.20 for transversal and longitudinal cross-sections, which reveal that thermal fatigue cracks started from valley regions in the roughness profile. They were only located in BC and did not penetrate into the base material, and thus cause no lifetime-limiting damages. Within the ceramic top coating, some segmentation cracks were also present.

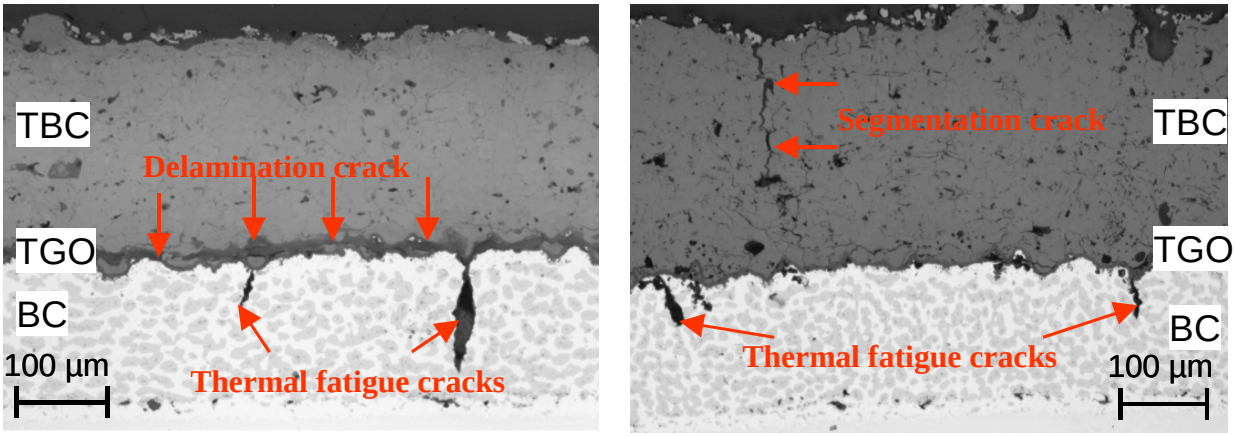

(a) (b)

Figure 5.20 – Delamination crack path after 23500 cycles at higher magnification: a) in longitudinal section, b) in transversal section

Besides the fatigue cracks in BC, three main types of cracks at the TBC/BC interface were present after 23500 thermal cycles (Figure 5.21):

1 - cracking within the topcoat (TBC);
2 - separation between the TBC and the TGO (TGO / TBC);
3 - cracks within the TGO (TGO).

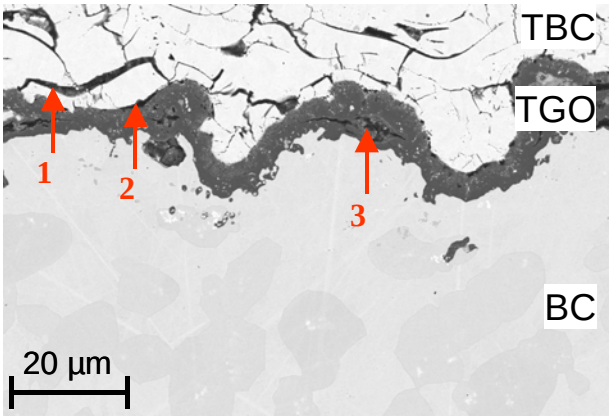

Figure 5.21 – SEM images of TBC cross-section after 23500 thermal cycles: cracks at the TBC/BC interface

Similar crack types were also observed in the initial stages of the isothermal exposure loading. The average TGO thickness was relatively small with about 3.5 µm because of short accumulated time at high temperature (about 30 hours at 1050 ± 5°C). Thus, the influence of

oxidation-related damage mechanisms was reduced. The TGO cracks did not exceed a length of about 20 µm and no evidence for penetration of these cracks into the TBC was found. Both values, i.e. length of cracks in the TGO and TGO thickness are consistent with the crack length data from section 5.2.1.3.
Damage was mainly caused by cyclic stresses generated due to the thermal expansion coefficient mismatch between bond coat and ceramic top coat. The main failure mode under thermal cycling was the delamination crack within TBC close to the TBC/TGO interface.

5.2.3 Cyclic oxidation

Under service conditions the TBC systems experience more complex loading than pure isothermal exposure or pure thermal cycling. A combination of either load components with predominant effect of oxidation or cyclic loading often occurred. Thermal cycling with high temperature exposure was realised by means of cyclic oxidation tests with high temperature dwell time of 2 hours at 1050°C. Experiments were carried out in two temperature ranges:

1. ΔT = 60 - 1050°C
2. ΔT = 350 - 1050°C

It was also investigated which damage mode and which types of microcracks were activated under a combined load profile such as cyclic oxidation.

5.2.3.1 Temperature range 60-1050°C

The tests were carried out up to failure in the same IR-furnace as the thermal fatigue tests. The damage was traced by *in situ* acoustic emission recording. After 700 cycles, which corresponds to 1400 hours exposure at 1050°C TBC spallation was occurred (Figure 5.22). This lifetime was similar to that after cyclic oxidation in a resistance furnace with the same TBC composition [109]. Figure 5.23 shows that the delamination crack path, which located partly in TBC, partly in TGO was between that for pure cyclic and pure isothermal exposure.

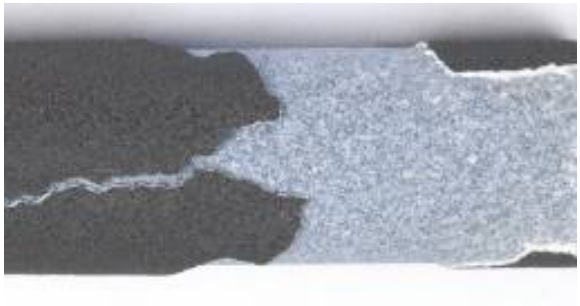

Figure 5.22 – Grey failure of TBC by spallation after thermal cycling in temperature range 60-1050°C with 2 hours of dwell time at high temperature (cyclic oxidation)

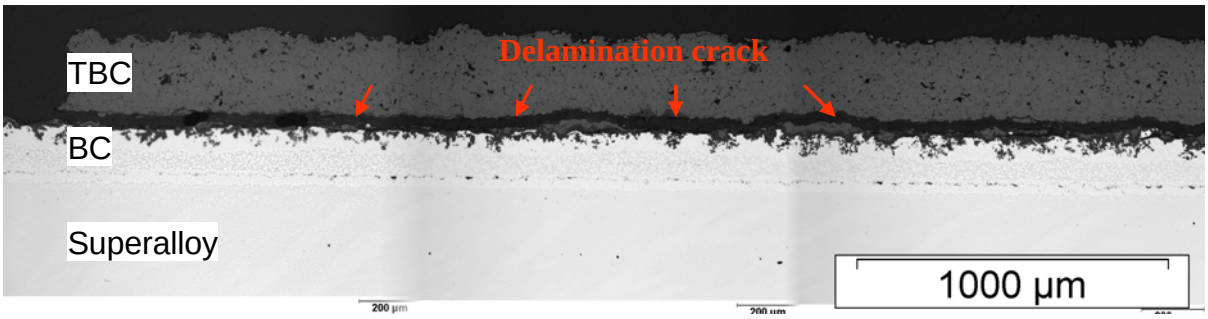

Figure 5.23 – Delamination of the TBC after 700 thermal cycles in temperature range 60-1050°C with 2 hours of dwell time at high temperature

Detailed views of both longitudinal and transversal sections are shown in Figure 5.24. Delamination cracks at the TBC/BC interface and segmentation cracks in the TBC were present. Since the cyclic oxidation loading consists of two load components (isothermal exposure and thermal cycling), damage processes related to each component were activated.

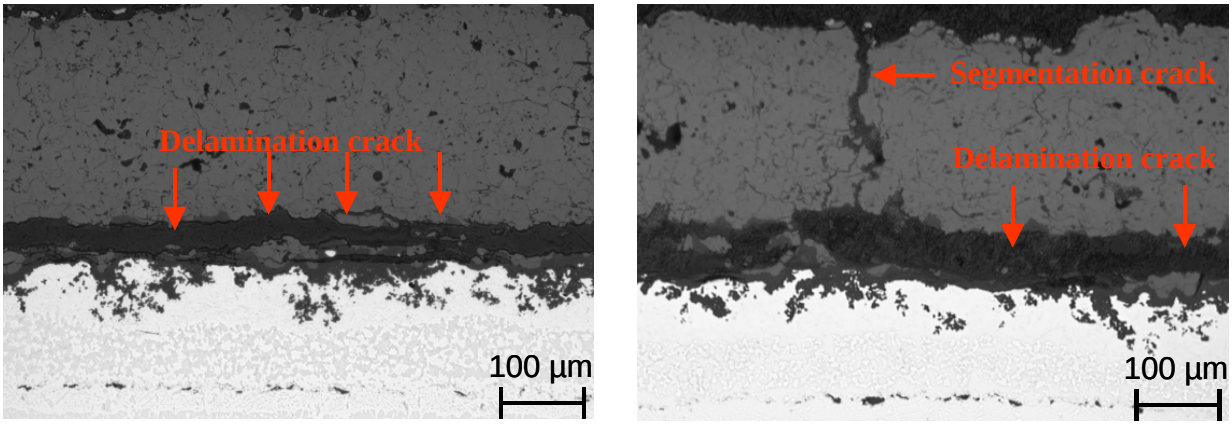

(a) (b)

Figure 5.24 – SEM images of delamination at the TBC/TGO interface after cyclic oxidation: a) length-section, b) cross-section

Oxidation related processes led to TGO growth of up to about 10 µm. In contrast to the longest isothermal exposure, the depletion of Al-rich β-phase in BC was not complete after failure. Additional cyclic damage accumulated due to thermal stresses led to accelerated crack propagation at the TBC/BC interface and thus a lower lifetime for TBC (4490 hours for isothermal exposure and 1400 hours for cyclic oxidation). It was shown in [109] for the same TBC system that TGO cracks were initiated and continued to grow in the TBC after only 500 cycles (1000 hours at 1050°C) under interrupted cyclic oxidation tests (Figure 5.25).

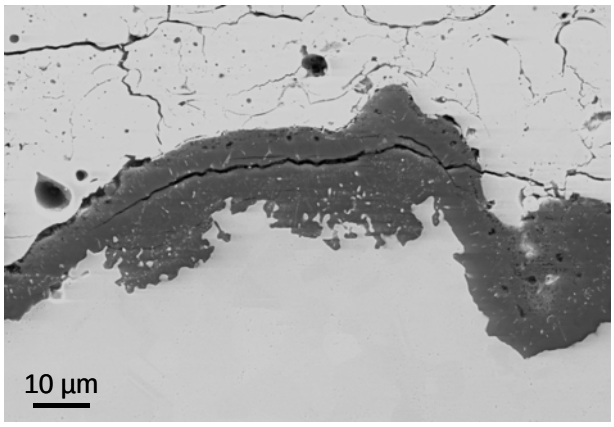

Figure 5.25 – SEM image of a typical mixed type crack in an APS specimen after cyclic exposure (1050°C, 1000h) [109]

Damage evolution under cyclic oxidation loading was monitored by acoustic emission. AE data recorded show continuous increase of accumulated AE events as well as AE energy (Figure 5.26), indicating a continuous damage buildup with each heating /cooling cycle.

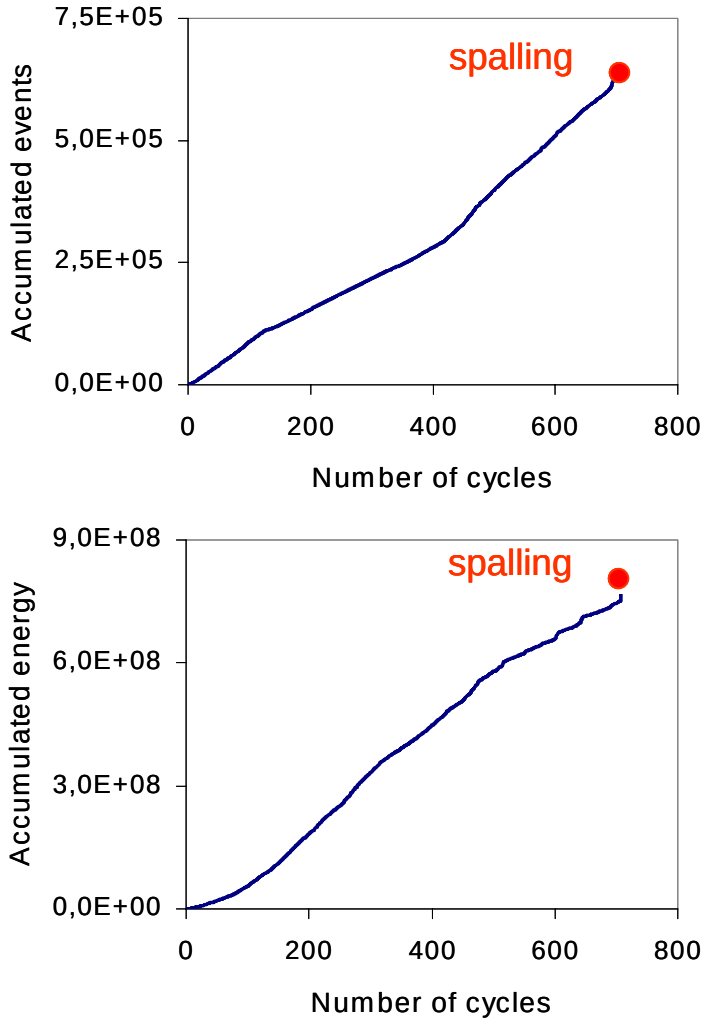

Figure 5.26– AE data recorded in-situ during thermal cycling: a) accumulated events; b) accumulated energy

The AE activity occurred mainly during cooling, while almost no AE signals were detected during high temperature dwell time, as shown in Figure 5.27. A steep increase in AE activity was observed in the temperature range 600-900°C and then below 300°C (Figure 5.27.b). At the highest temperature in the oxidation cycle, the BC composition lay in a four-phase region of the ternary Ni-Cr-Al diagram and in a three-phase region at 850°C and below. The coating thus underwent a change of its microstructure for every cycle, which might be accompanied by volume changes [42] and resulting near-interface stresses and damage increases.

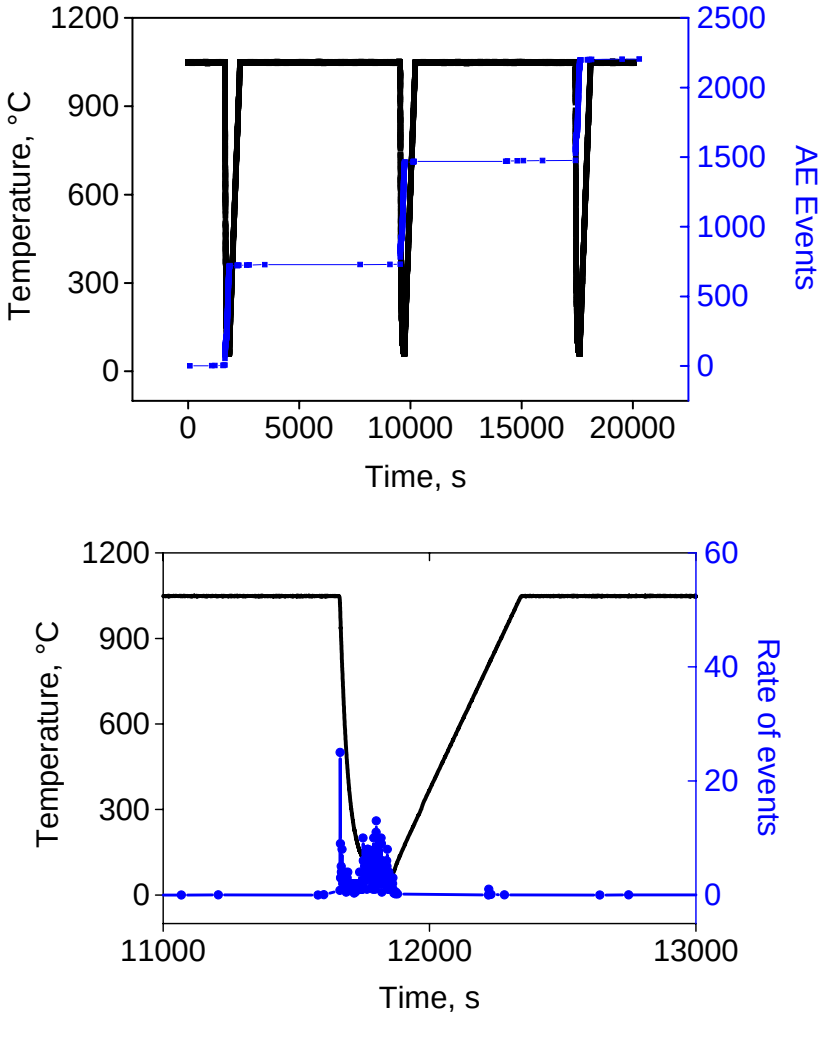

Figure 5.27 – (a) Temperature dependence of accumulated AE events and (b) rate of AE events under thermal cycling with HT dwell time (cycles No.10 and 11 are shown)

From the AE data, it is evident that the damage occurs during cooling due to an increase in thermal stresses. The AE activity increased with an increasing temperature drop, especially below 300°C. This correlates with increasing thermal stresses due to the mismatch of thermal expansion coefficients.

5.2.3.2 Temperature range 350-1050°C

The next step involved conducting the cyclic oxidation in the temperature range 350-1050°C with the aim to investigate the influence of the minimum temperature of the thermal cycle.
The test was terminated after 1450 cycles when a macroscopic crack was observed (Figure 5.28.a). The test duration corresponds to 2900 hours exposure at 1050°C. Thermographical analysis revealed that the TBC was widely delaminated along the crack except for a small area ahead the crack, as shown by the white curve in Figure 5.28.b. The temperature decays for the green, red, yellow and blue measuring points were retarded, which clearly indicates delaminations that disturb the thermal flow through the material. Only the white measuring point shows a normal temperature decay, i.e. no delaminations.

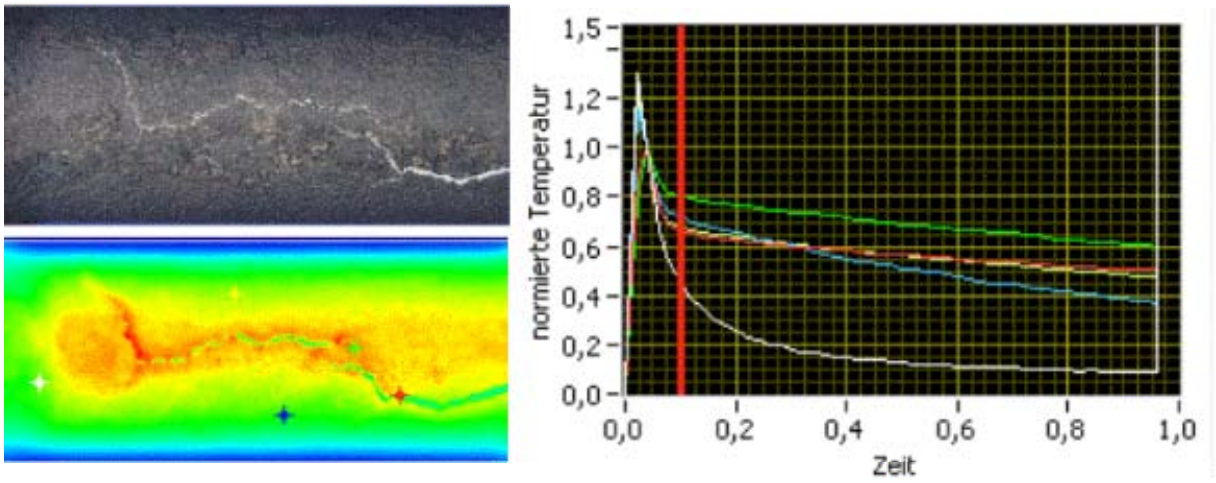

(a) (b)

Figure 5.28 – (a) Macro and thermographical images and (b) temperature-time curve of impulse thermography of TBC specimen after thermal cycling in temperature range 350-1050°C with 2 hours of dwell time at high temperature

The delamination crack path is pointed out in Figure 5.29. It was similar to that after cyclic oxidation in the temperature range 60-1050°C. Thus, the difference in the minimum temperature of thermal cycling had no significant influence on the failure mode of the TBC.

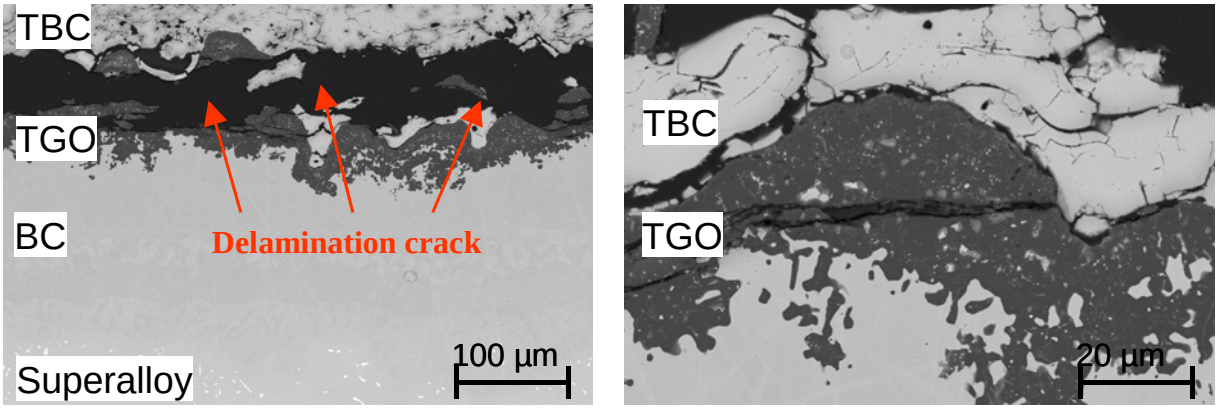

(a) (b)

Figure 5.29 – SEM images of cross-sections after TBC spallation: a) delamination crack, b) detailed view of damaged TGO

However, increasing the minimum temperature (decrease of temperature range) in the thermal cycle led to a longer lifetime, due to decreased thermal stresses. Thus, thermal stresses contribute to the degradation process to a limited extent in comparison to BC oxidation under cycling oxidation in the temperature range 350-1050°C. The average TGO thickness after 1490 cycles was around 12 µm, similar to the isothermally exposed sample with an exposure time of 3000 hours at high temperatures.

5.2.4 Cyclic oxidation with temperature gradient

The influence of a superimposed temperature gradient as an additional load component besides thermal cycling and high temperature exposure is discussed in this section. The bond coat temperature was 1050°C; the TBC surface temperature was 1150°C, corresponding to a temperature drop of 100°C over the TBC or a gradient of approximately 0.3°C/µm. This load profile resulted in a considerably lower lifetime of 56 cycles or 112 hours of exposure at high temperature. Failure occurred when one piece of coating spalled while the rest of YSZ coating was still intact (Figure 5.30).

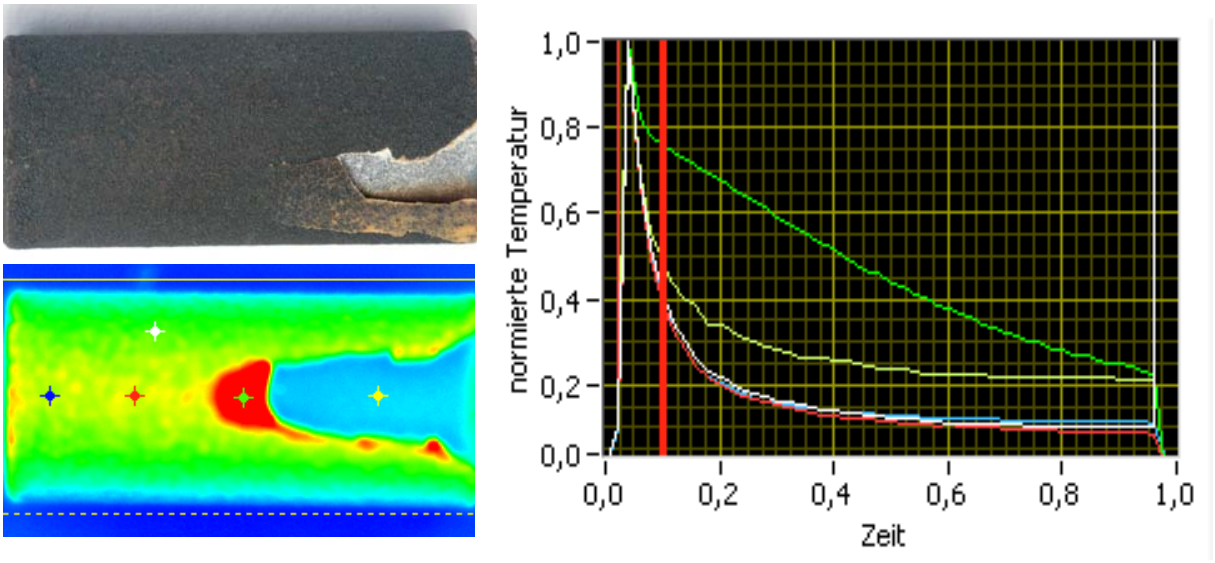

(a) (b)

Figure 5.30 – Macro and thermographical images: a) TBC specimen; b) time-temperature curves after thermal cycling with gradient in temperature range 60-1050 °C (bond coat) / 1150 °C (TBC surface) with 2 hours of dwell-time at high temperature

Examinations of the respective specimen cross-section revealed (Figure 5.31.a):

1) delamination cracks close to the surface;
2) delamination cracks close to the interface;
3) diagonal cracks from the interface to the surface.

Furthermore, delamination cracks propagated in the TBC at some distance from the TBC/TGO interface as shown in Figure 5.31.b. This crack also comprises diagonally oriented parts, which propagated towards the surface, however no spallation of TBC was observed.

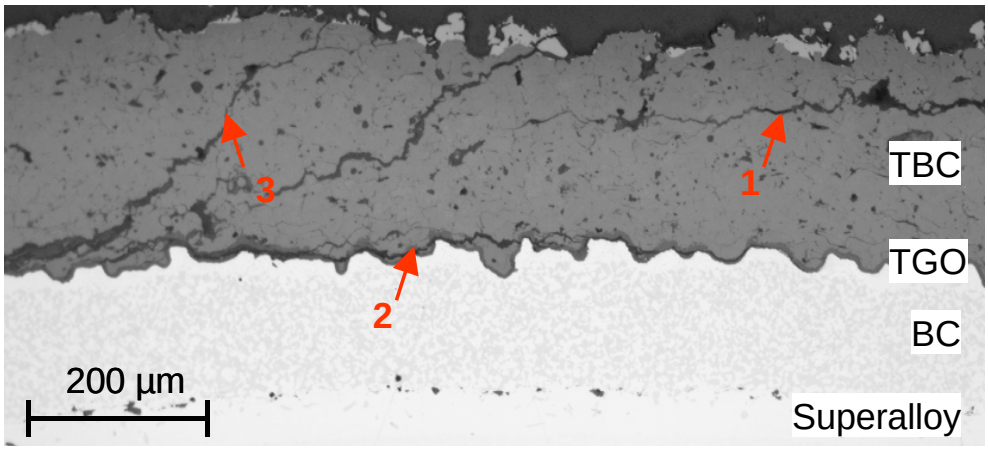

(a)

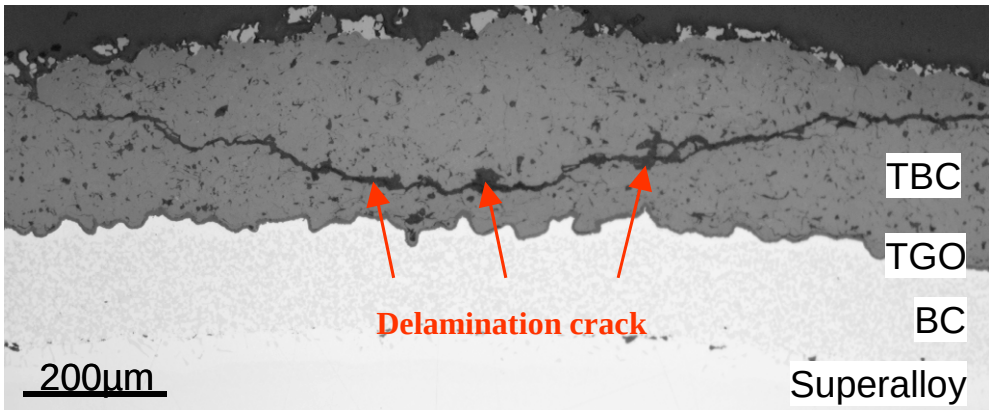

(b)

Figure 5.31 – Examples of delamination and segmentation cracks in TBC causing spallation of top coating (cross-section)

The shifting of the delamination crack towards the TBC is probably related to the sintering processes in the ceramic top coat. Sintering could be promoted by higher compressive stresses in the TBC caused by the temperature gradient. This can lead to the stiffness increase and thus a decrease in strain tolerance under cyclic loading. A more detailed discussion of the possible deformation mechanisms in APS TBC under compression and the corresponding microstructural changes can be found in section 5.5.

In Figure 5.32 the delamination crack path observed in the longitudinal section is shown. Crack propagated mostly within TBC close to the TBC/TGO interface (Figure 5.32.a). At a higher magnification (Figure 5.32.b), cracks within the TGO as well as at the TGO/BC interface can be observed. These cracks with lengths up to about 40 µm did not propagate into the TBC and thus did not affect the failure mode. The average TGO thickness remained relatively low – about 5 µm. This is in good agreement with critical crack length and TGO thickness found for the initial crack growth stage of crack propagation kinetics under isothermal exposure (section 5.2.1.3).

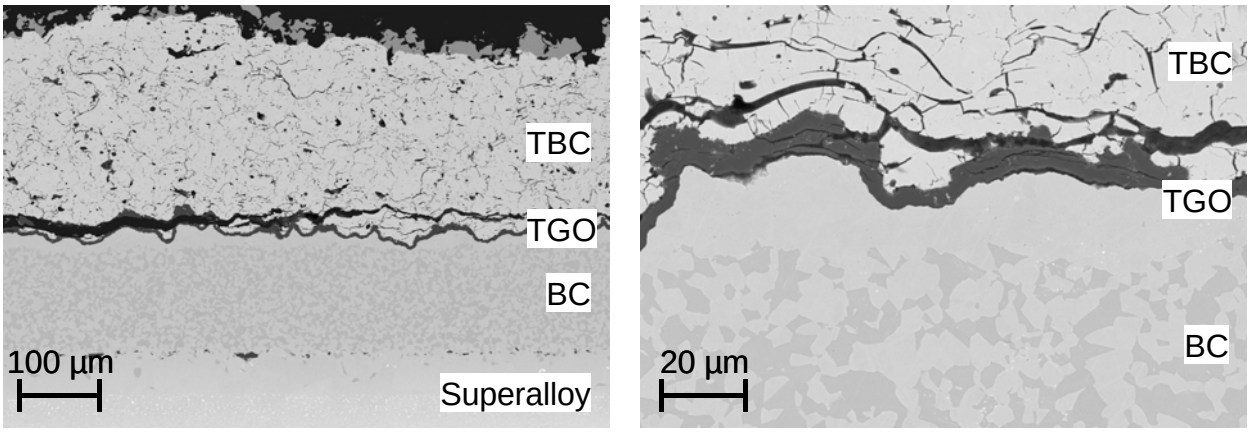

(a) (b)

Figure 5.32 – SEM images of length sections after 56 thermal cycles: a) delamination TBC/TGO crack, b) detailed view of crack path

5.2.5 Lifetime and failure mechanisms under various thermal loadings

In Figure 5.33, the comparison of the time at high temperature (lifetime) is shown for four thermal load profiles:

- Isothermal exposure;
- Thermal cycling;
- Cyclic oxidation (two temperature ranges);
- Cyclic oxidation with temperature gradient.

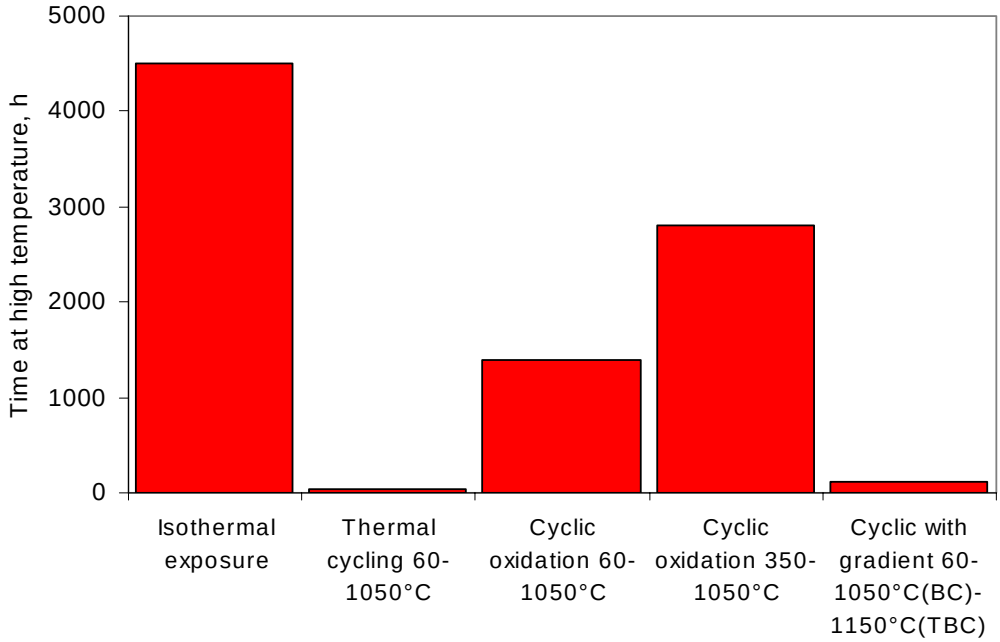

Figure 5.33 – Dependence of TBC lifetime on loading profile

The longest lifetime (4490 hours) was observed for isothermal exposure, whereas under thermal cycling, only about 30 hours at 1050±5°C were accumulated. A combination of both load components in the cyclic oxidation tests led to a decrease in lifetime (1400 hours) in

comparison to isothermal loading. This effect was less pronounced when the temperature range was decreased due to increase in the minimum cycle temperature (2890 hours). Finally, the introduction of a third load component - temperature gradient - led to a considerable decrease in TBC lifetime (112 hours).

Moreover, the isothermal exposure of plasma-sprayed thermal barrier coatings caused spallation of the ceramic top coat along the TGO (partly in the TGO and partly in the TBC), whereas thermal cycling led to the delamination crack path in the TBC. The combination of both thermal cycling and HT exposure load components in cyclic oxidation tests resulted in the final failure crack path forming between that for pure cyclic and pure isothermal exposure. If a temperature gradient across the coating was additionally superimposed under cyclic oxidation loading, the crack propagation path would have shifted into the TBC.

The observed failure modes for the respective loading profiles are displayed schematically in Figure 5.34.

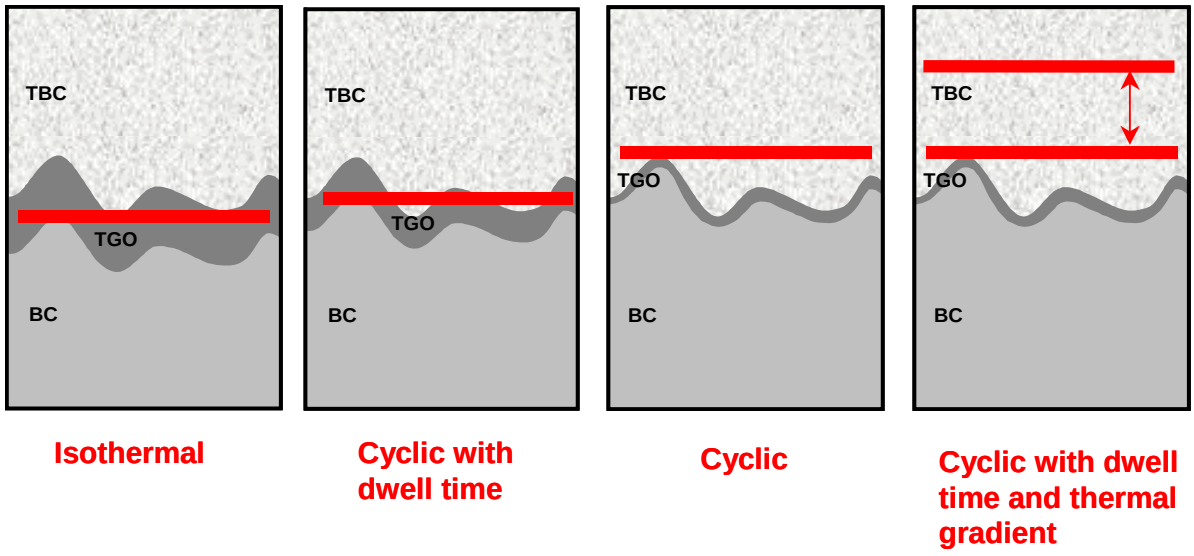

Figure 5.34 – Delamination crack path as a function of increase in cyclic and/or temperature range components under thermal loading

A possible failure mechanism, which may have led to the observed delamination crack patterns for APS TBC is illustrated schematically in Figure 5.35. In the earlier studies of degradation, the cracks started to form at the TBC/TGO interface or existing cracks within the TBC close to the TBC/TGO interface opened (Figure 5.35.a). Under thermal cycling loading, these initiated cracks subsequently propagated approximately parallel to the TGO/TBC interface, touching the TGO at the peaks. Delamination cracks propagate above valley regions because of high compressive stresses there due to the rough BC surface (Figure 5.35.b).

When the oxidation related load components are present (isothermal or cyclic oxidation) cracks can form at the TGO/BC interface after a certain time (TGO thickness) and grow within the limits of roughness amplitude (Figure 5.35.c). With TGO thickening, the local stress distribution changes and cracks can penetrate the TBC and link up. As a result,

delamination crack formed propagates partly through the TBC and partly through the TGO (Figure 5.35.d).

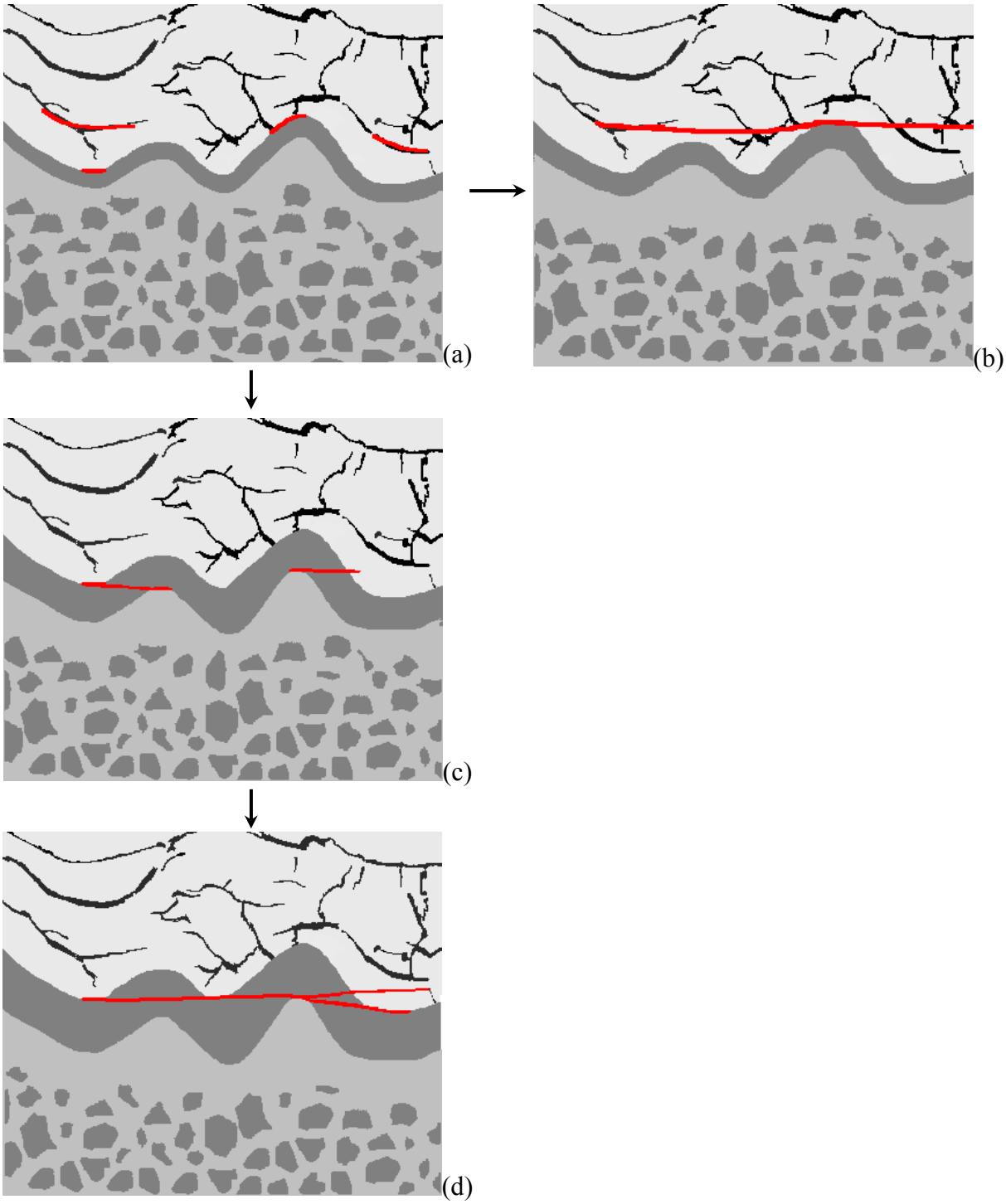

Figure 5.35 – Schematic of microstructural development leading to the failure of the TBC under thermal loading: a-b) thermal cycling, a-c-d) isothermal or cyclic oxidation

5.3 Thermomechanical loading

Under service conditions, the hot gas turbine components, e.g turbine blades, experience cyclic mechanical loading in addition to thermal loading. In order to characterize the influence of both cyclic thermal and cyclic mechanical loads on damage and failiure of the APS-TBC composite, thermomechanical fatigue tests were carried out. Most of the TMF experiments were performed using the out-of-phase (OP) cycle type, for which the maximum compressive strain develops at a maximum temperature and the maximum tensile strain at a minimum temperature. One experiment was also conducted under in-phase (IP) conditions with a maximum compressive strain at a minimum temperature and the maximum tensile strain at a maximum temperature.

The influence of the high temperature exposure on damage mechanisms and failure modes of the TBC was investigated using two approaches: (i) pre-oxidation treatment at 1050°C before testing and (ii) integration of high temperature dwell time at 1050°C into the TMF cycle.

The corresponding testing conditions and the results are listed in Table 5.3.

Table 5.3 - Summary of TMF loading conditions and experimental results

Type	**Cycle**	**Dwell time at 1050°C**	**Pre HT at 1050°C**	**N_f, cyc**	**t_f, h**
TMF OP	ΔT=350-1050°C Δε= 0.6 %	---	---	1620	---
			300 h	948	---
			1000 h	615	---
			2000 h	620	---
TMF OP	ΔT=350-1050°C Δε= 0.6 %	2 h	---	619	1240
TMF OP	ΔT=350-1050°C Δε= 0.3 %		---	1638	3276
Cyclic oxidation	ΔT=350-1050°C Δε= 0 %		---	1442	2890
TMF IP	ΔT=350-1050°C Δε= 0.6		---	531	1060

5.3.1 Mechanical behaviour, failure mode

The symmetrical out-of-phase TMF test represents a superposition of cyclic mechanical and cyclic thermal load components with a phase angle of 180°. Figure 5.36 shows a typical example of the temperature-strain cycles for the OP TMF test with a 0.6 % mechanical strain range and a temperature range between 350 and 1050°C, which was applied to the TBC system.

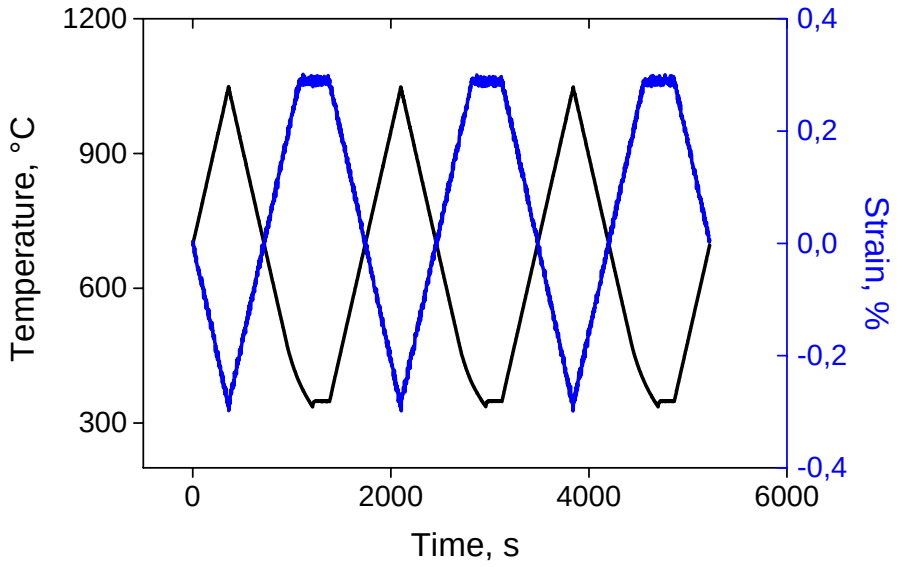

Figure 5.36 – OP TMF cycle applied to TBC

Stress-temperature hysteresis loops for different numbers of load cycles are shown in Figure 5.37. A short dwell time at T_{min} was introduced to compensate a slight deviation from the nominal cooling rate.

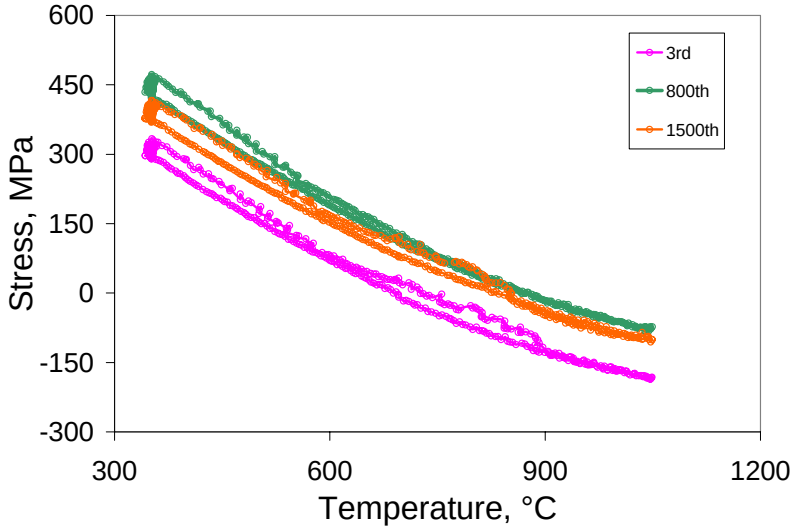

Figure 5.37 – Stress-temperature loops at three different numbers of load cycles during OP TMF with mechanical strain range of 0.6% and temperature range of 350-1050°C

The measured stresses as a function of the cycle number is displayed in Figure 5.38. The maximum and minimum stresses shifted towards higher tensile stresses with increasing cycle numbers because of relaxation processes at high temperature.

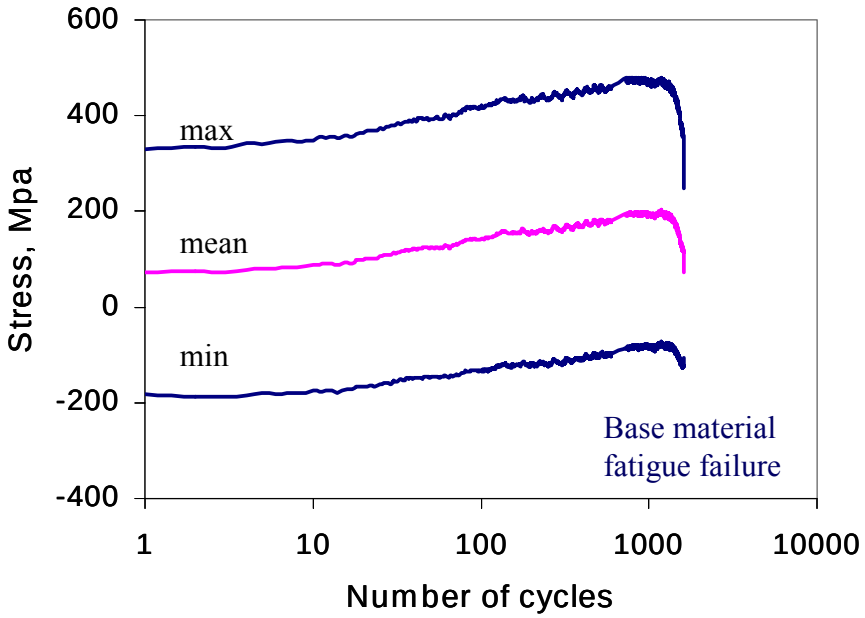

Figure 5.38 – Evolution of maximum, mean and minimum stresses applied to TBC under OP TMF with mechanical strain of 0.6% range and temperature range of 350-1050°C

A tensile stress of about 350 MPa was developed after first cycles and reached a maximum of about 500 MPa shortly before end of life. Sharp decrease in tensile stresses in last cycles gave evidence for pronounced fatigue crack growth. Failure of base material occurred after 1620 cycles. As a consequence, near the failure crack in the base material, a segmentation crack in the TBC as well as a macroscopic delamination of about 1 mm in diameter was formed in the TBC, as can be seen in Figure 5.39.

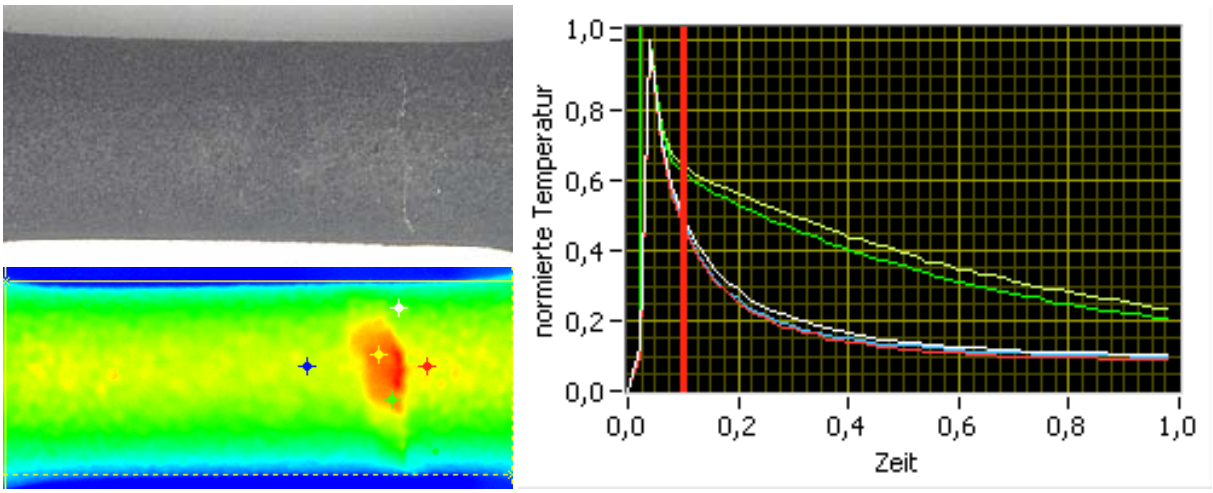

(a) (b)

Figure 5.39 – (a) Macro and thermographical images and (b) temperature-time distribution of TBC specimen after OP TMF in temperature range of 350-1050 °C with mechanical strain range of 0.6 %

Microstructural observation on transversal (Figure 5.40.a) and longitudinal (Figure 5.40.b) cross-sections revealed failure crack initiation in the bond coat and subsequent crack propagation into the substrate and the ceramic top coating.

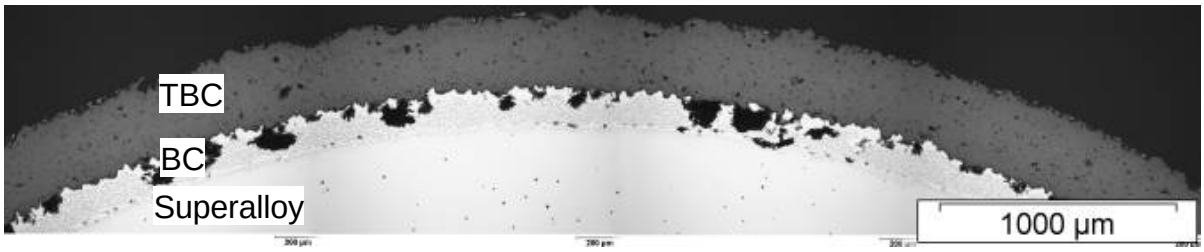

(a)

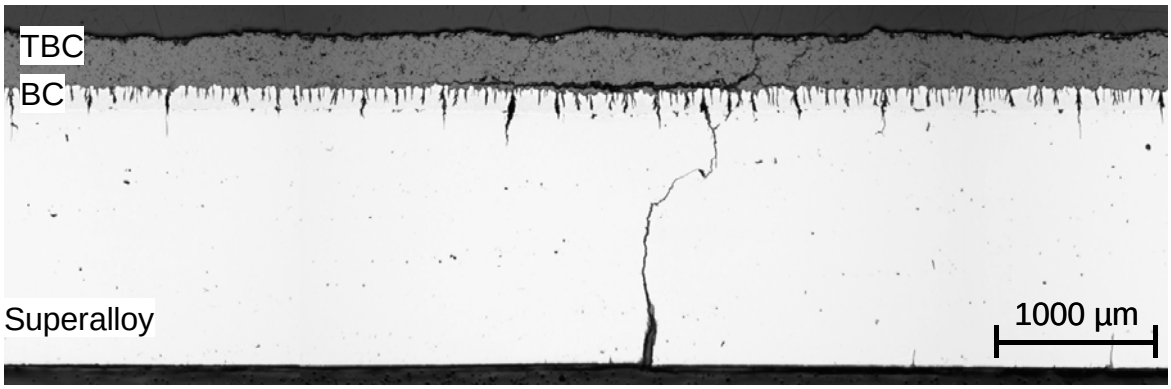

(b)

Figure 5.40 – An overview of the crack propagation within the TBC system under OP TMF TMF with mechanical strain range of 0.6% and temperature range of 350-1050°C: a) in cross-section; b) in length-section

Detailed view of TBC/BC interfaces and fatigue cracks formed after OP TMF are illustrated in Figure 5.41. The cracks were formed at the bond coat/TBC interface at valley regions as a result of enhanced stresses there due to notch effects. The same observations were reported in [91] for a similar TBC system.

Fatigue cracks appeared as narrower cracks in longitudinal section and as widely opened cracks in transversal section (Figure 5.41). No delamination cracks at the TBC/BC interface nor segmentation cracks within topcoat were found.

The crack surfaces, as well as the TBC/BC interface, were covered with oxide scales of the same thickness of about 4 µm. The relatively low TGO thickness is presumably the reason for the fact that coating failure did not limit the lifetime rather than base material failure. This is consistent with the results that long-range delamination cracks at the interface do not develop before a TGO thickness of about 8-10 µm is reached.

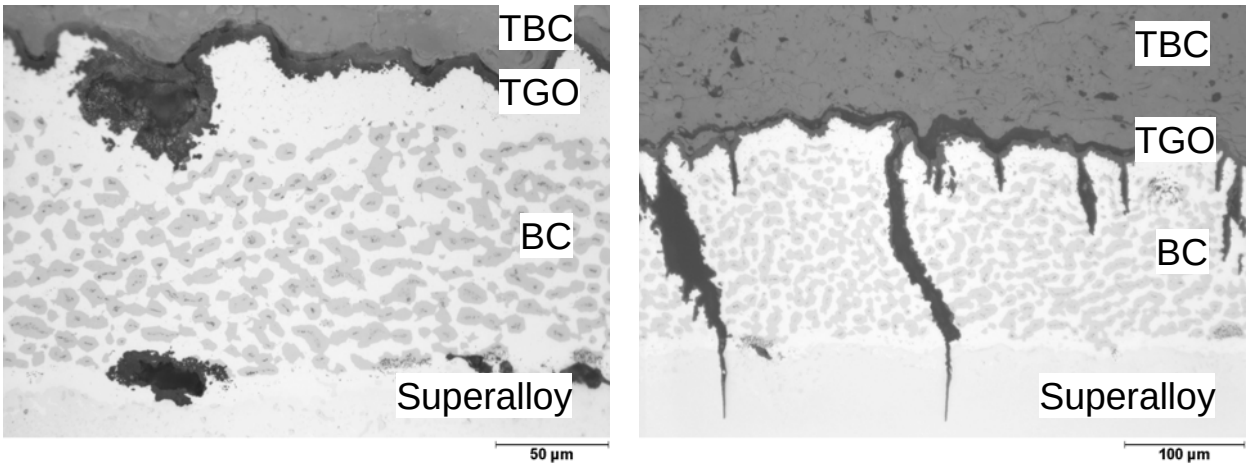

(a) (b)

Figure 5.41 – Detailed view of TBC/BC interface after OP TMF test: a) fatigue crack in BC (transversal section); b) penetration of fatigue cracks in base material, delamination TBC/TGO crack (longitudinal section)

5.3.1.1 Influence of pre-oxidation treatment

With the aim to activate delamination damage in TBC, some specimens were subjected to high temperature exposure at 1050°C prior to the TMF tests. It was mentioned in the literature that the presence of a TGO of a certain thickness could lead to delamination failure of the TBC [93] before fatigue cracking of base material.

Taking into account data for TGO growth as well as crack growth kinetics under isothermal exposure at 1050°C (see section 5.3.1.3), three different pre-oxidation times were chosen: 300 hours, 1000 hours and 2000 hours. The initial TGO thickness was about 5 µm, 7 µm and 9 µm, respectively. Moreover, initiated oxidation processes led to microcrack formation at the TBC/BC interface with lengths up to 40 µm.

The OP TMF tests were carried out with the same parameters as for non-treated specimens, e.g. with mechanical strain range of 0.6 % and temperature range between 350 and 1050°C. The effect of the pre-oxidation treatment on the cyclic stress response in comparison to non-treated TBC under TMF is represented in Figure 5.42.

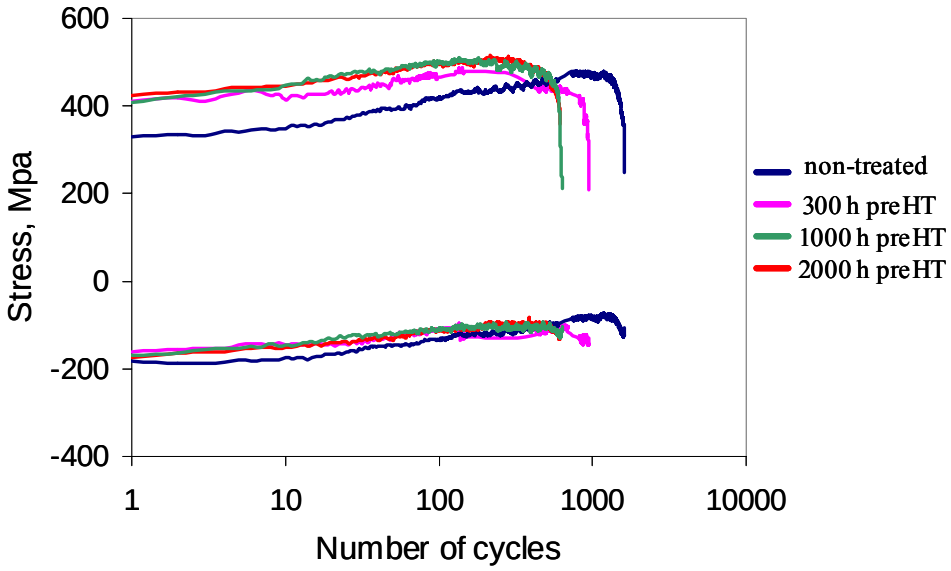

Figure 5.42 - Maximum and minimum stresses versus number of cycles under OP TMF with mechanical strain range of 0.6% and temperature range of 350-1050°C for TBC specimen after different pre-oxidation treatment

TBC specimens after heat treatments revealed similar behaviour to the non-treated specimen, when the maximum and minimum stresses shifted in the tensile regime during TMF test. Typical tensile stress drop in later stages of testing occurred for all pre-oxidised specimens, indicating fatigue failure of the base material. An example of the failure mode after OP TMF test for specimen pre-oxidized for 300 hours is shown in Figure 5.43

Figure 5.43 – Failure mode of TBC specimen pre-oxidized for 300 hours after OP TMF with mechanical strain range of 0.6% and temperature range of 350-1050°C

Moreover, for pre-oxidized specimens the tensile stress level developed was higher than that for non-treated specimen (about 510-515 MPa instead of 495 MPa) while the compressive stresses had the same level. Thus specimens after pre-oxidation treatments experienced higher stress range during TMF in comparison to these that was not treated. This resulted in a considerable decrease in the lifetime of tested TBC systems with an increase in the pre-

oxidation time, as shown in Figure 5.44. Cyclic lifetime was reduced by approx. 40 % for specimen pre-oxidized for 300 hours at 1050°C and by more than 60% for specimen pre-oxidized for 1000 hours. Further reduction in lifetime for specimen oxidized for 2000 hours was not observed.

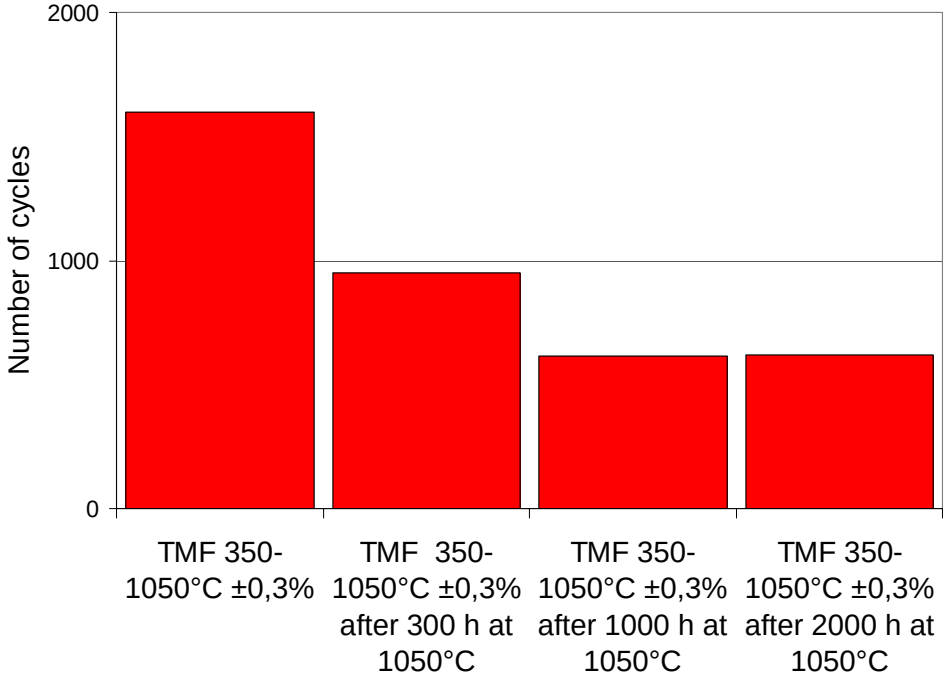

Figure 5.44 – TMF lives as a function of pre-oxidation time at 1050°C

Microstructural observation revealed that the increase in pre-oxidation time was correlated with a decrease in fatigue crack density, as shown in Figure 5.45, also when compared with non-treated specimen (Figure 5.40.b). It can be related to the morphological changes at the TBC/BC interface caused by oxidation processes, as shown in Figure 5.46.

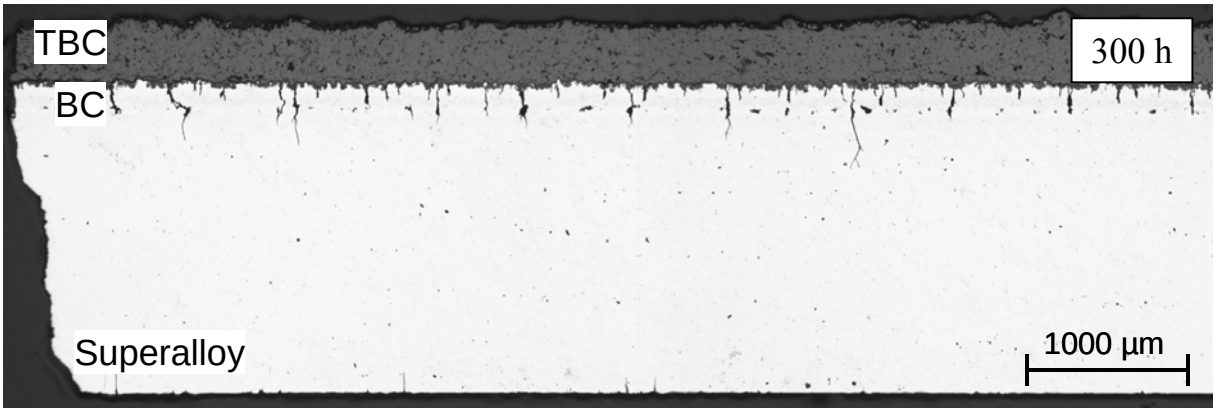

(a)

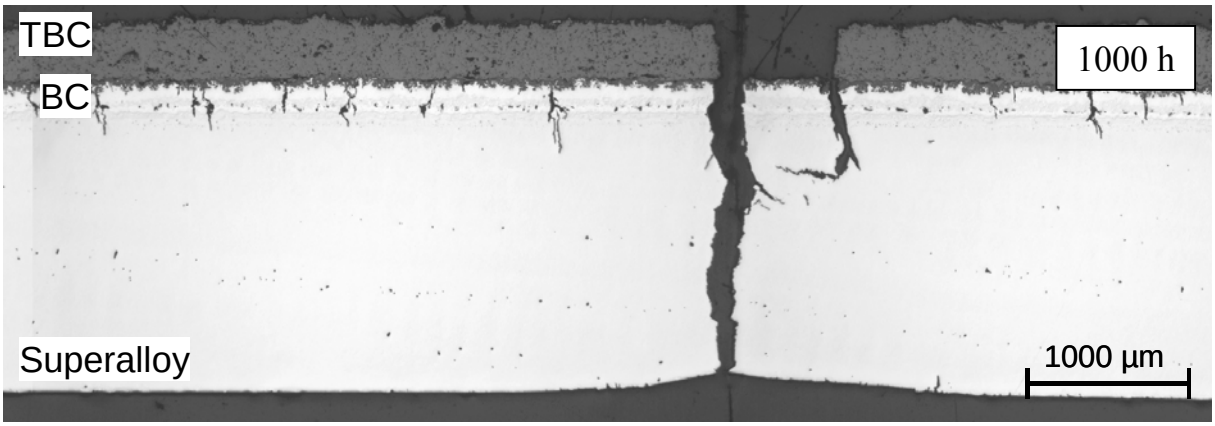

(b)

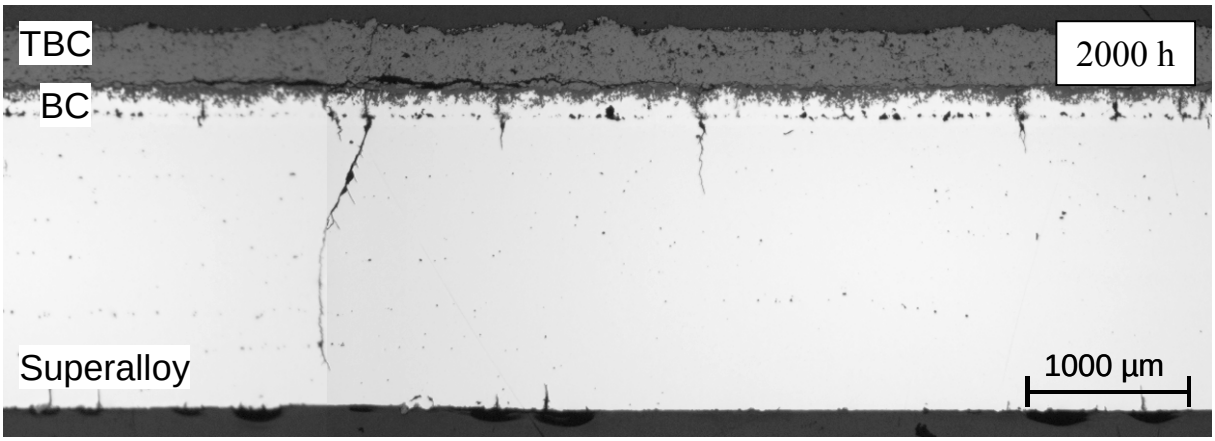

(c)

Figure 5.45 – Longitudinal sections of TBC specimen after different pre-oxidation treatments TMF tested in temperature range of 350-1050 °C with mechanical strain range of 0.6 %: a) 300 hours, b) 1000 hours and c) 2000 hours

As it was mentioned for non-treated specimen, the fatigue cracks in most cases started at the valley region of TGO/BC interface roughness due to enhanced thermal and mechanical stresses at those places. Pre-oxidation treatment led to TGO growth and consecutive reduction in interface roughness and thus to the reduction of respective stresses. Moreover, for pre-oxidized specimens, delamination cracks were observed propagating within the TBC close to the TBC/TGO interface (Figure 5.46.b-d), but they did not lead to the spallation failure before fatigue failure.

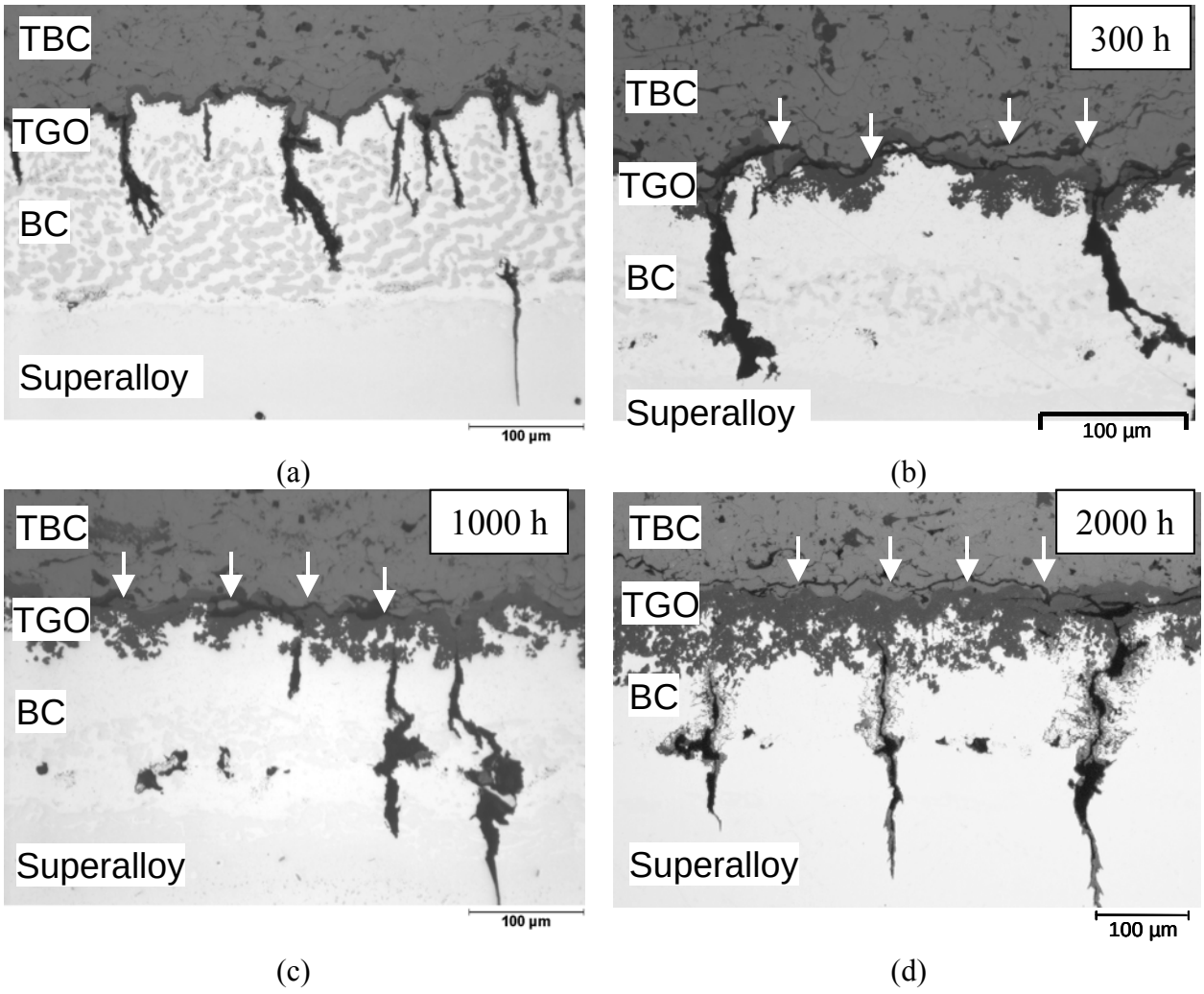

Figure 5.46 – Bond coat and base material cracking of TBC during OP TMF in temperature range of 350-1050 °C with mechanical strain range of 0.6 %: (a) in non-treated state and after (b) 300 hours, (c) 1000 hours, (d) 2000 hours of pre-oxidation treatments (white arrows indicate delamination cracks in TBC)

5.3.1.2 OP TMF with dwell time

In order to achieve the service failure in the TBC system, the high temperature exposure load component was integrated into the TMF cycle. It was realised in TMF with a dwell time of 2 hours at T_{max}, as shown in Figure 5.47. Experiments were carried out in two strain ranges: 0.6% and 0.3%.

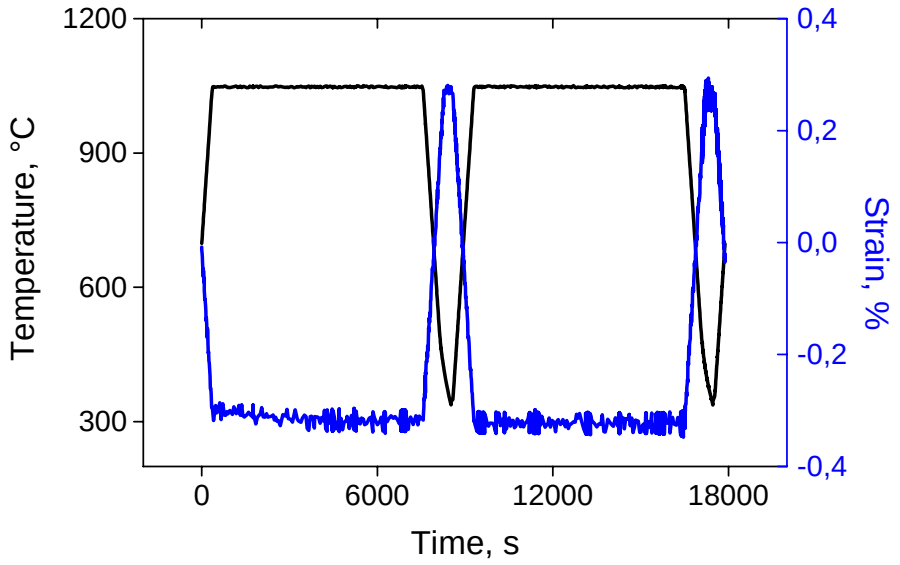

Figure 5.47 – Example of OP TMF cycle with a dwell time at high temperature applied to TBC

Cycle stress response revealed a typical OP TMF shift in the tensile regime similar to that observed for TMF without a high temperature dwell time (Figure 5.48). With a decreasing strain range both the maximum and the minimum stresses decreased, e.g. the maximum tensile stress decreased from 400 MPa for a mechanical strain range of 0.6 % to 250 MPa for a mechanical strain range of 0.3 %.

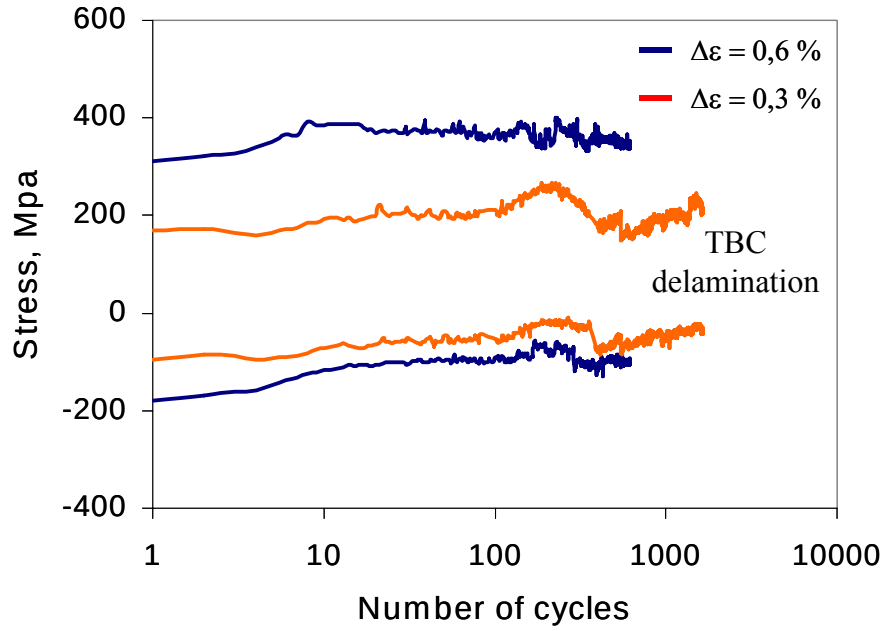

Figure 5.48 - Evolution of maximum and minimum stresses applied to TBC under OP TMF with a dwell time in temperature range of 350-1050°C

In contrast to TMF tests without a dwell time, the failure occurred by TBC spallation before fatigue cracking of base material, therefore no reduction was observed in the stress level. Failure occurred after 620 cycles for TMF with a strain range of 0.6% and 1638 cycles with a strain range of 0.3%. This corresponded to 1240 and 3276 hours of high temperature exposure, respectively. An example of TBC spallation after TMF with 0.6 % strain is shown in Figure 5.49.

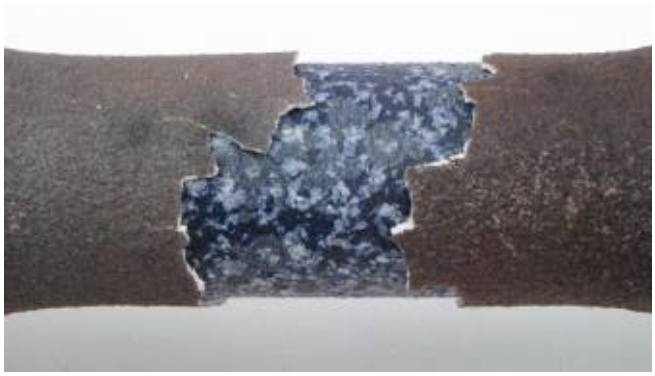

Figure 5.49 - Spallation of TBC after OP TMF with dwell time at high temperature in temperature range of 350-1050°C and mechanical strain range of 0.6 %

Taking into account data obtained for the cyclic oxidation of TBC in the same time-temperature cycle between 350 and 1050°C (see section 5.3.3.2) i.e. TMF with 0 % mechanical strain, it is clear that cyclic mechanical strain of 0.6 % led to a decrease of more than a factor of two in TBC lifetime.

Examination of the cross-sections after OP TMF with dwell time (Figure 5.50) showed the presence of fatigue cracks in BC. The crack density also decreased with decreasing strain range. Almost all cracks were of a similar length and stopped at the BC/superalloy interface.

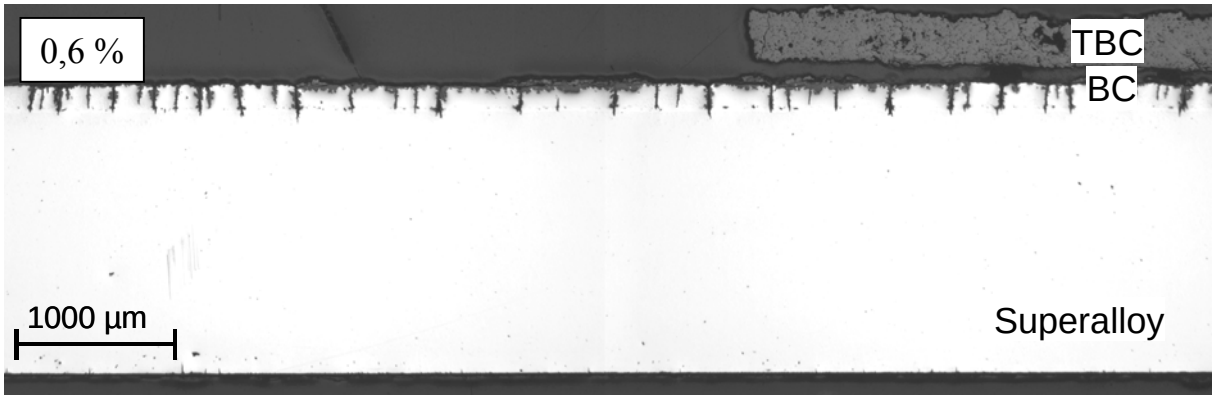

(a)

(b)

Figure 5.50 - Overview of the crack propagation within the TBC system under OP TMF with a dwell time and temperature range of 350-1050°C: a) mechanical strain range of 0.6%, b) mechanical strain range of 0.3%

A detailed view of TBC with spalled topcoat is presented in Figure 5.51. The delamination crack path ran partly in TGO, partly in TBC. A similar oxide thickness was observed around the crack and on the interface, which leads to the assumption that initiation of cracks took place within first cycles of the TMF test. The average TGO thickness was about 12 µm.

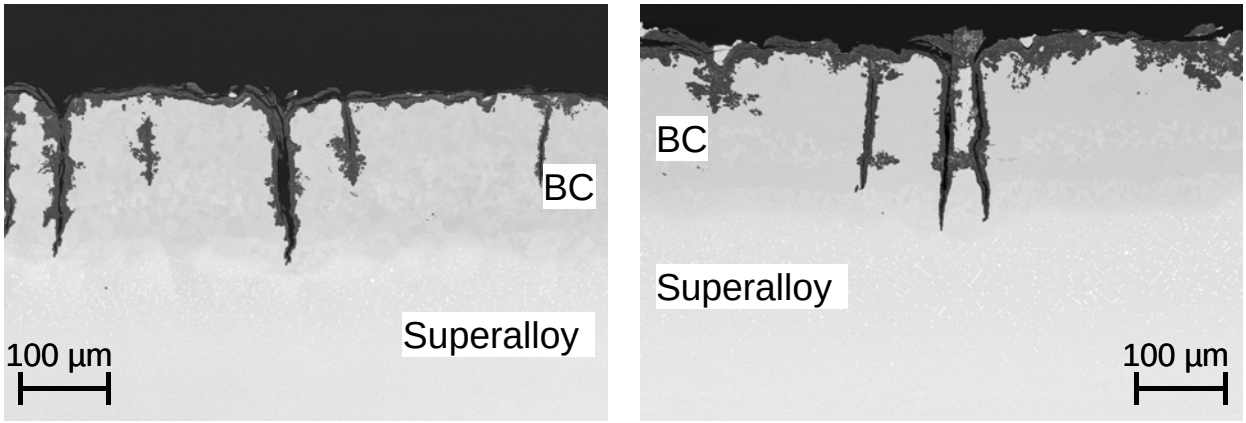

(a) (b)

Figure 5.51 – TBC spallation after OP TMF with dwell time and temperature range of 350-1050°C: a) mechanical strain range of 0.6%, b) mechanical strain range of 0.3%

5.3.1.3 IP TMF with dwell time

In order to investigate the influence of the cycle form on damage mechanisms and the failure mode of TBC under TMF load with high temperature dwell time, the IP cycle with mechanical strain range of 0.6 % and temperature range between 350 and 1050°C was applied, as shown in Figure 5.52.

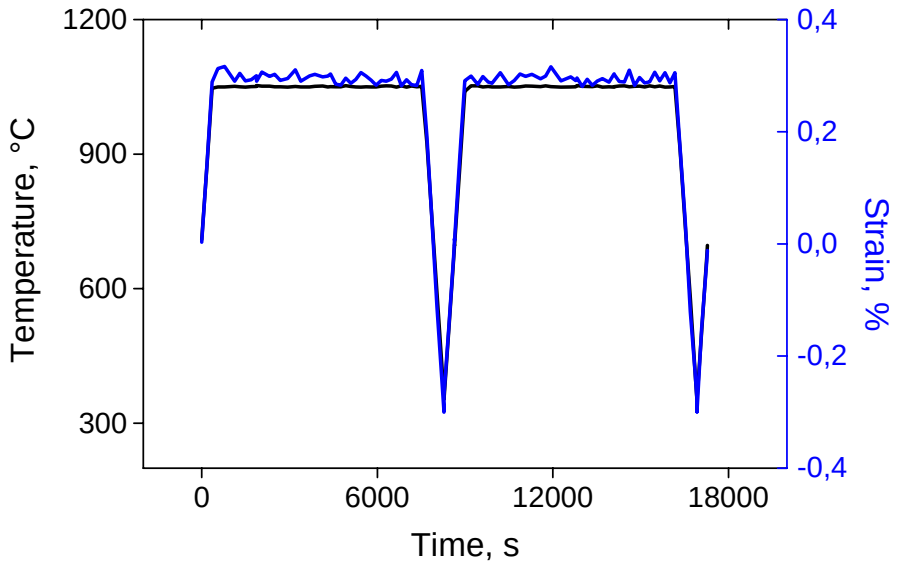

Figure 5.52 - IP TMF cycle with dwell time at high temperature applied to TBC system

During IP TMF cycling, the maximum compressive and tensile stresses were developed at the low and high temperature, respectively. The cyclic stress response is shown in Figure 5.53. The compressive stress of about 420 MPa developed after the initial cycles and reached maximum of about 550 MPa.

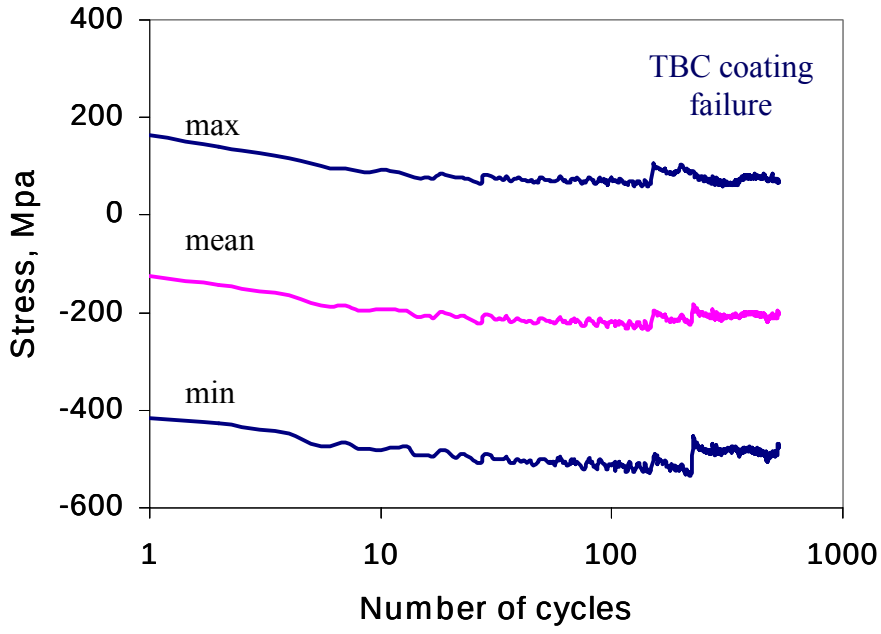

Figure 5.53 – Evolution of maximum, mean and minimum stresses applied to TBC under IP TMF with dwell time, mechanical strain range of 0.6% and temperature range of 350-1050°C

Failure occurred after 531 cycles by delamination segmentation cracking in TBC, as can be seen in Figure 5.54. Thermography analysis shows that there was complete delamination damage of TBC.

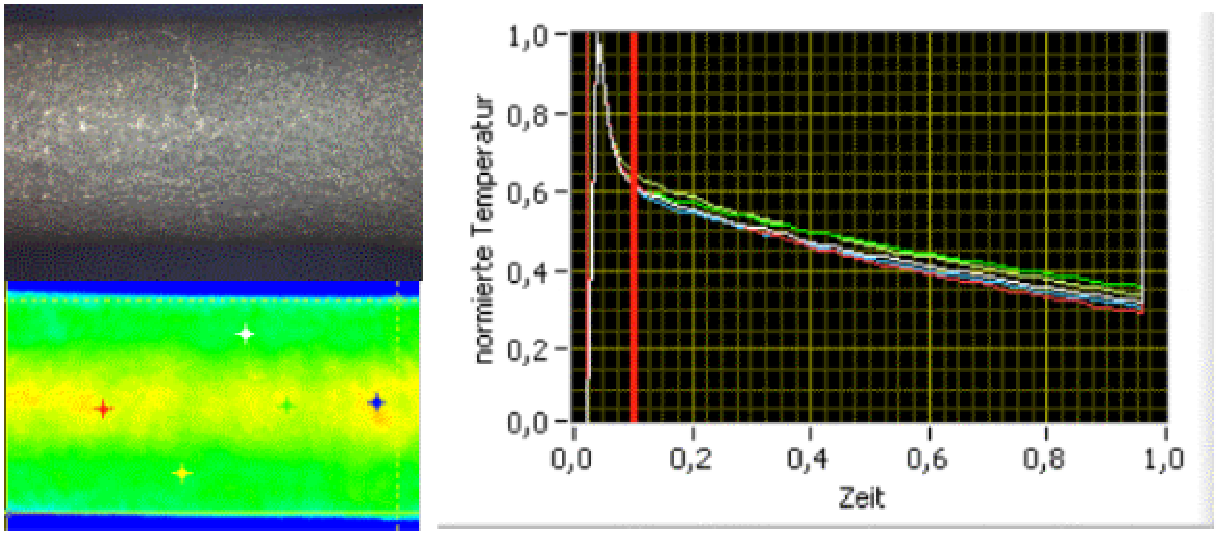

(a) (b)

Figure 5.54 – (a)Macro and thermographical images and (b) temperature-time distribution of TBC specimen after IP TMF with dwell time in temperature range of 350-1050°C with mechanical strain range of 0.6 %

Microstructural observations revealed that under IP TMF cycling no fatigue cracks were formed in the BC (Figure 5.55). Instead, cracks were found within the superalloy propagating from pores perpendicular to the loading direction.

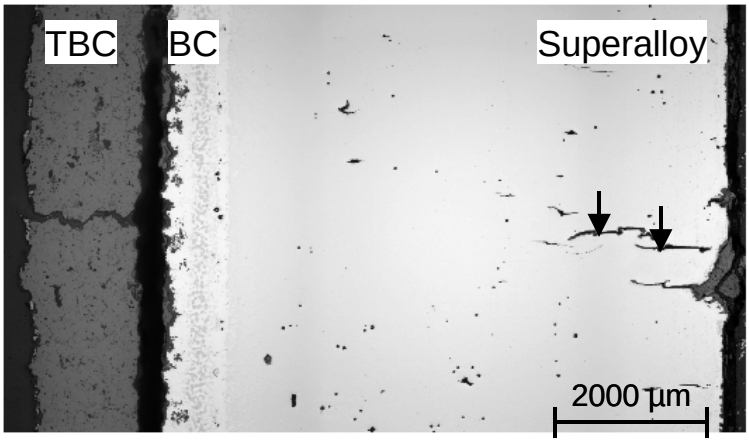

Figure 5.55 – Delamination crack propagation within the TBC after IP TMF with dwell time in temperature range between 350-1050°C and mechanical strain range of 0.6%; black arrows indicate creep-fatigue cracks in the superalloy

The detailed view of the TBC / BC interface illustrated in Figure 5.56 shows the delamination crack path through the TGO and TBC, which is similar to that observed under OP TMF with dwell time. The average TGO thickness was also the same - about 12 µm.

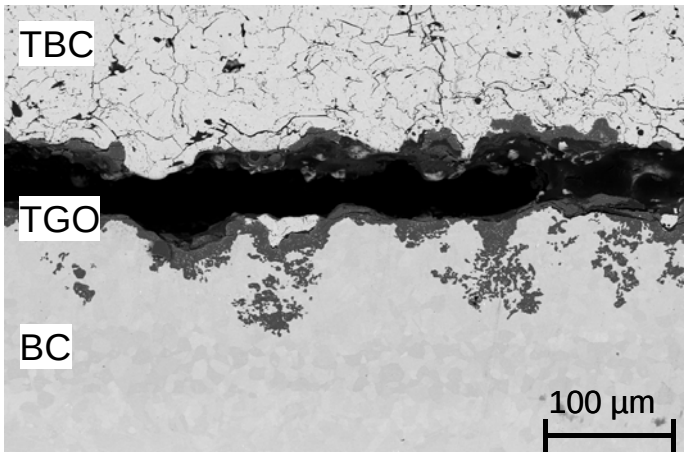

Figure 5.56 – Delamination crack at the BC/TBC interface after IP TMF with dwell time in temperature range between 350-1050°C and 0.6% mechanical strain range

Thus, for all TMF tests with a dwell time independent of the cycle form (OP/IP) and the strain range applied, the main failure mode is TBC delamination and/or spallation. The delamination crack path ran partly in the TGO, partly in the TBC similar to that observed after cyclic oxidation.

In contrast, the lifetime of the TBC systems was strongly dependent on the total strain amplitude and the cycle shape. The TMF lives of the OP tests with dwell time and different strain ranges as well as the IP test are compared in Figure 5.57.

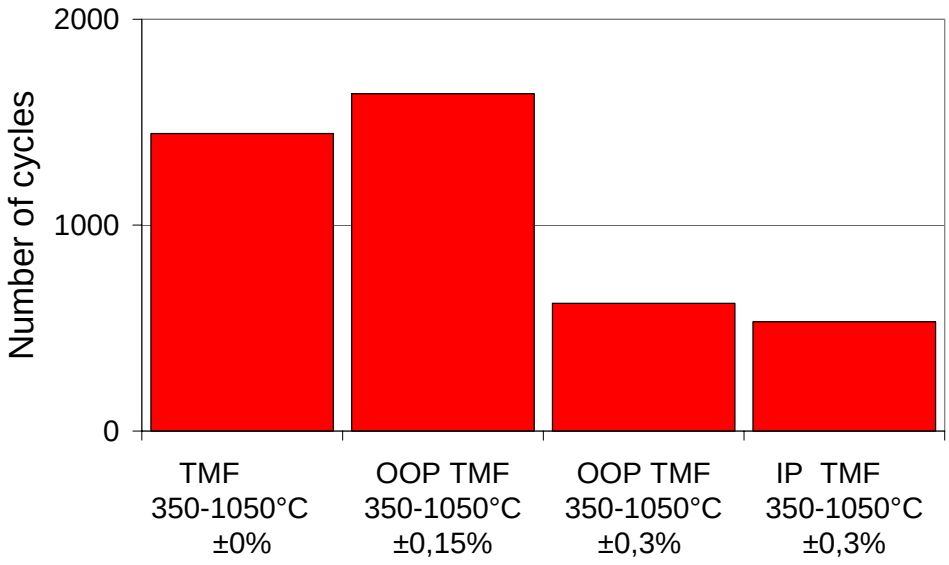

Figure 5.57 - Dependence of TBC lifetime on TMF cycle parameters

Mechanical strains in the range of 0.6 % led to a significant reduction (almost factor of three) in lifetime in comparison to cyclic oxidation or TMF with a smaller strain range. At the same time, lifetimes for OP and IP TMF cycle forms varied in the range of 10 %.

The failure mode under TMF loading changed only when the high temperature dwell time was integrated into the TMF cycle. TBC spallation failure was thus attained before fatigue

cracking of base material. Moreover, the activation of oxidation-related damage mechanisms due to dwell time led to a shift in the delamination crack path towards the TGO, as was observed for thermal cycling and cyclic oxidation. Taking into account only OP TMF with the same strain range, the damage modes can be schematically represented as shown in Figure 5.58.

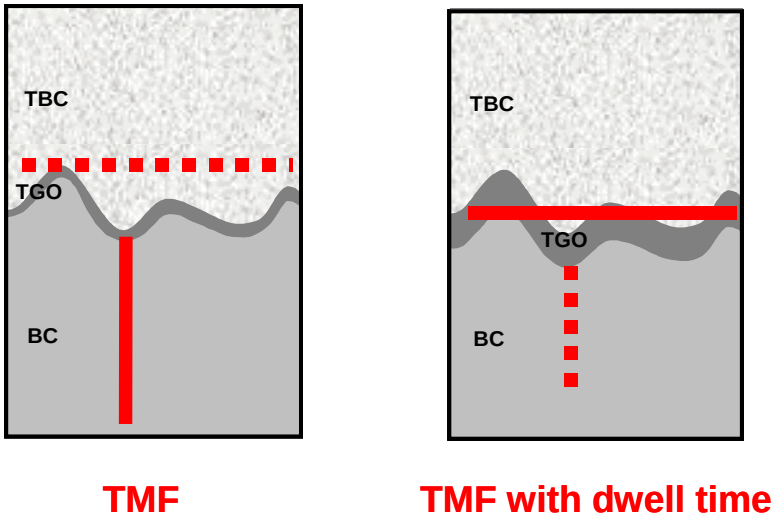

Figure 5.58 – Damage modes as a function of the cycle form component under thermomechanical loading

With the aim of investigating possible damage mechanisms, e.g. fatigue crack propagation, the interdiffusion processes at the BC/base material interface were studied using a number of techniques in SEM and discussed in following section.

5.3.2 Failure mechanisms under TMF loading

For TMF tests it was observed that the fatigue cracks formed at the TBC/BC interface limited the lifetimes because they propagated into the base material. For TMF with dwell time at high temperature, failure of topcoat occurred first because fatigue cracks were stopped at the BC/base material interface. High temperature exposure led to the development of an interdiffusion zone between the BC and superalloy. Thus interdiffusion and phase transformation processes are important aspects in understanding the thermomechanical fatigue failure of TBCs. With the aim to investigate microstructural changes that occurred on the BC/base material interface, the interdiffusion zone was closely studied using a number of techniques.

5.3.2.1 Interdiffusion between the BC and superalloy

First of all, the microstructural changes caused by interdiffusion processes between the BC and base material were investigated using SEM. Two specimens tested under different TMF cycles were compared with the as received one.

As received

Figure 5.59 shows the interdiffusion zone between the BC and base material in the TBC system for as received TMF specimen.

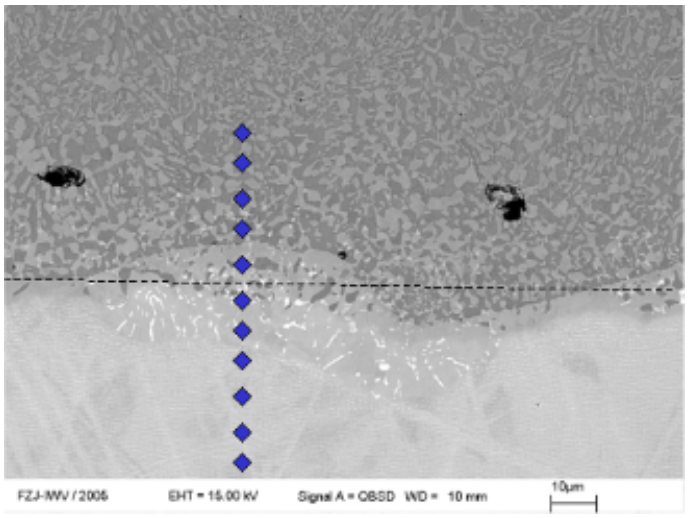

Figure 5.59 – SEM image of interdiffusion zone in as-received state; dashed line displays original BC/superalloy interface

The distribution of elements through the interdiffusion zone was studied by taking spot chemical analyses along a line-scan. Figure 5.60 displays the line-scan data for main bond coat and base material elements.

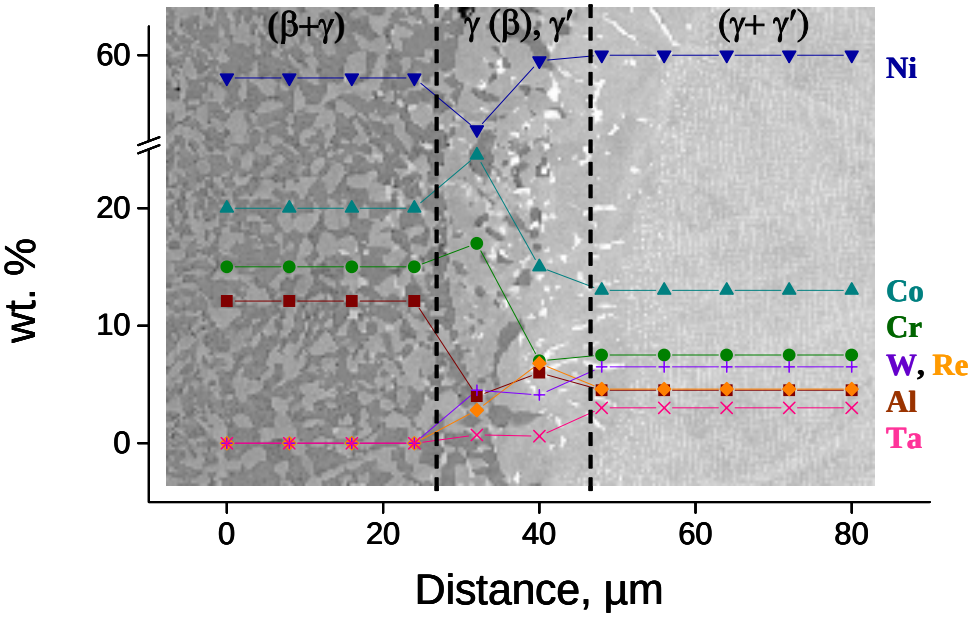

Figure 5.60 – Composition of interdiffusion zone in as-received state measured by EDX point analysis from Figure 5.59

Due to concentration gradients cobalt, chromium and aluminium diffuse out from the bond coat while nickel and rhenium as well as refractory elements diffuse into the coating. That leads to the depletion of β-phase and the precipitation of γ′-Ni_3Al along the interfaces.

Among the refractory metals, the interdiffusion of molybdenum, tantalum and tungsten is detected by the formation of TCP phases and carbides containing these elements along the substrate/coating interface.

Figure 5.61.a and b are higher magnification views of Figure 5.59, showing microstructural details of the interdiffusion zone in the BC depleted zone and affected substrate zone, respectively.

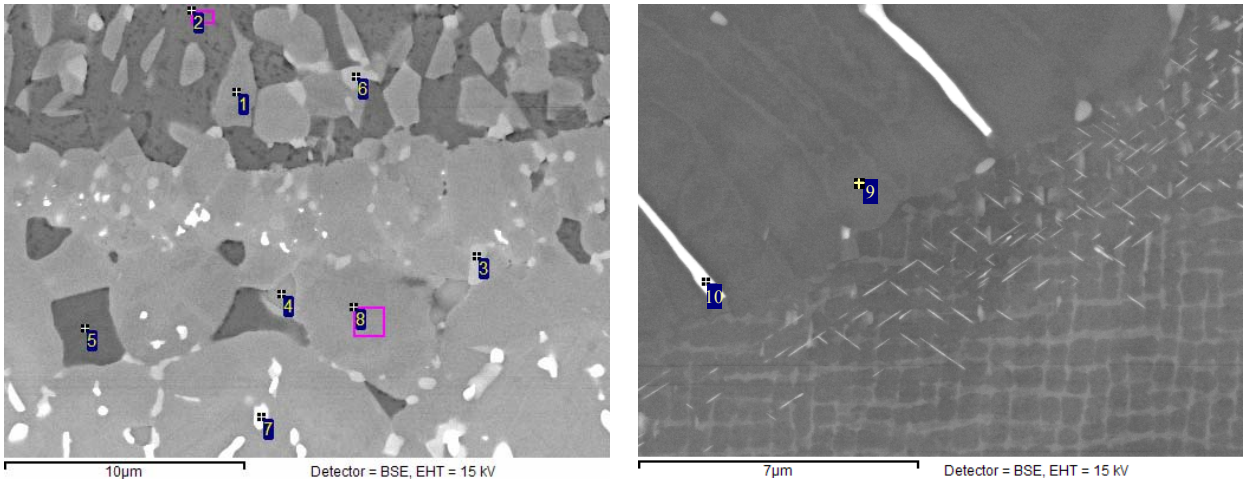

(a) (b)

Figure 5.61– Detailed view of interdiffusion zone in as-received state: a) close to BC, b) substrate affected zone

Points in Figure 5.61 indicate examples of EDX analysis. The average chemical composition for the various phases was obtained from three different places and is summarised in Table 5.4.

Table 5.4 - Chemical composition of interdiffusion zone and precipitates, **wt%**

Nr.	Phase	Ni	Al	Co	Cr	W	Ta	Re	Ti
1, 8	**γ**	46	3,5	26	19	3,5	2	---	---
2,5	**β**	64	16	14	5		0.6	---	0.4
6	**α-Cr**	16	1	30	40	7	1	5	---
7, 10	**μ- phase**	10		16,5	12	36,5	2	23	---
	σ-phase	21,5	1	26	31,5	11	1	8	---
9	**γ´**	62	7,5	11	4,5	5	4,7	---	1

In the main coating layer three phases can be observed: (i) γ phase matrix (points 1, 8), (ii) Al-rich β phase(points 2, 5) and (iii) Cr- rich α phase (point 6).The BC interdiffusion zone is characterized by the presence of Y-rich precipitates, as well as Cr- and Ta- carbides. To identify carbides, the EDX or WDX line-scan analysis was performed as shown in Figure 5.62 and Figure 5.63.

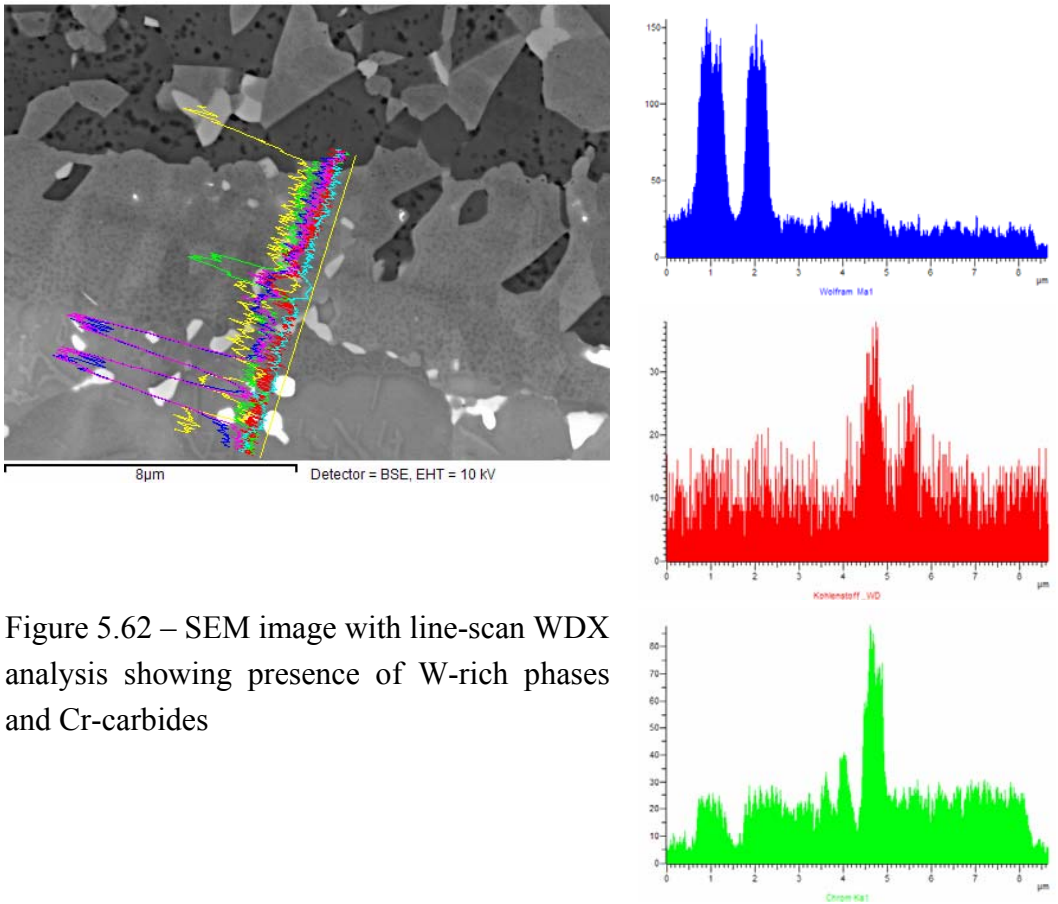

Figure 5.62 – SEM image with line-scan WDX analysis showing presence of W-rich phases and Cr-carbides

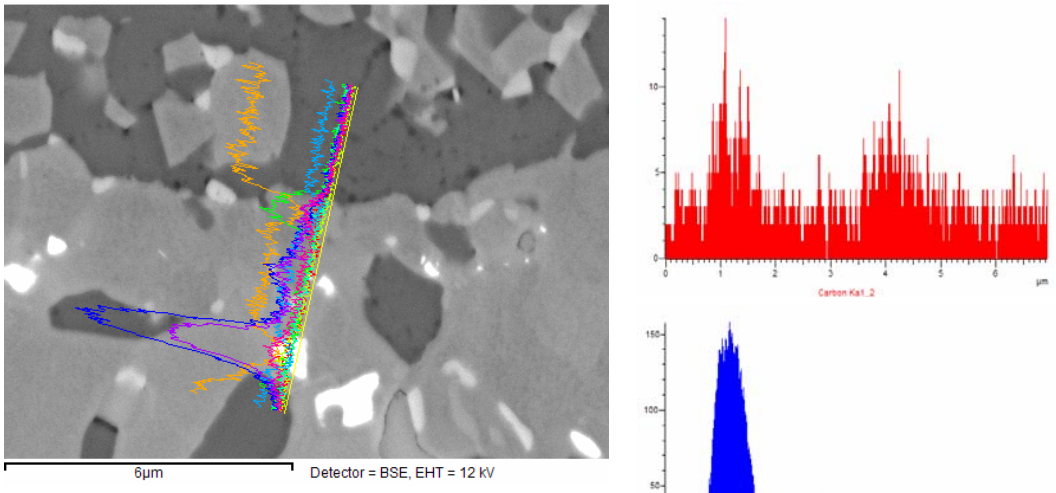

Figure 5.63 – SEM image with line-scan EDX analysis showing presence of Ta-carbides

The affected substrate zone has lost the typical single crystal γ / γ´morphology, and appears as a continuous γ´ layer. In this region precipitates with high content of W exhibit either round or elongated morphologies. From the chemical composition measured by EDX, it can be assumed this is a μ-phase with Co_7W_6 structure. In addition to the more usual Mo and W refractory elements, the μ phase is also rich in Re and Ta. Similar precipitation has also been observed in [79]. Occasionally, precipitates were found with similar composition and morphology to μ-phase, but with lower W and Re content and higher Cr content. They were identified as σ-phase. The composition of the precipitates is shown in Table 5.4. Also, a very fine needle-like phase within a single crystal structure was not possible to identify with SEM, TEM is needed to define them.

TMF tested samples

Figure 5.64.a and b shows length sections of samples after TMF and TMF with dwell time at high temperature (temperature range 350-1050°C, strain range 0.6%), respectively. The temperature and strain range of the tests are similar, but time at temperature accumulated during the tests was significantly lower for TMF (<10 hours) than for TMF with dwell time (1250 hours). This resulted in different interdiffusion zone development. As mentioned previously, the average interdiffusion zone for the as received sample was about 15 μm. For samples after TMF testing, it reached a thickness of approximately 40μm and >80 μm for both tests without and with dwell time, respectively.

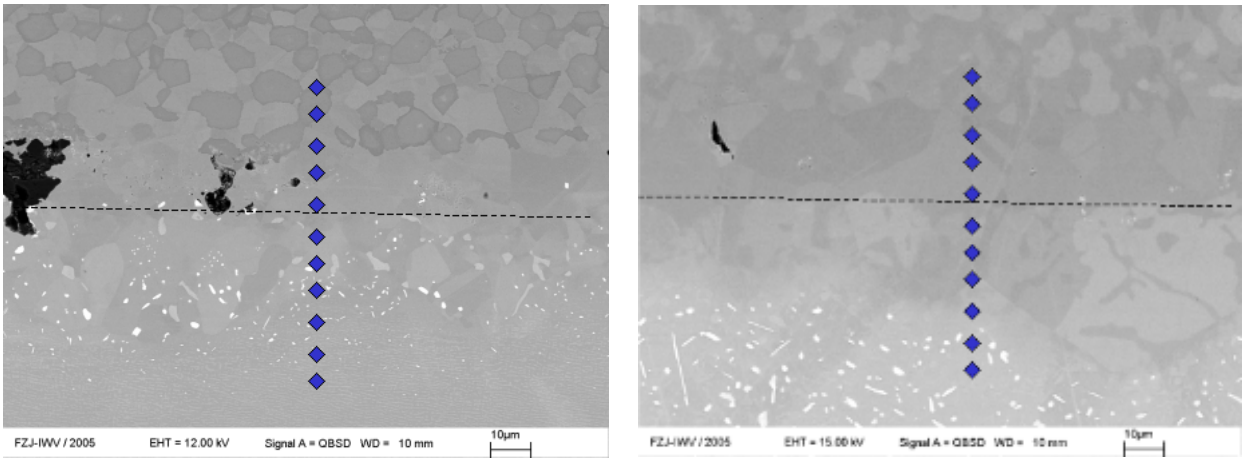

(a) (b)

Figure 5.64 – SEM image of interdiffusion zone after (a) OP TMF, (b) OP TMF with dwell time; dashed line represents original BC/superalloy interface

It is clear seen in Figure 5.64 that for longer exposure times at high temperature, precipitates in the substrate-affected zone occur deeper into the substrate. Furthermore, the number of precipitates beneath the γ- phase zone increased significantly with increasing exposure time at high temperature. Comparison of interdiffusion zone compositions (Figure 5.65 a and b) also revealed that γ formation at the expense of γ´ occurred with time in substrate. γ´-phase

destabilization is likely promoted by Cr diffusion from BC. Moreover, Co and Al also diffused from BC into the γ / γ′ zone. As a result of this diffusion processes, the diffusion front moved towards the substrate superalloy.

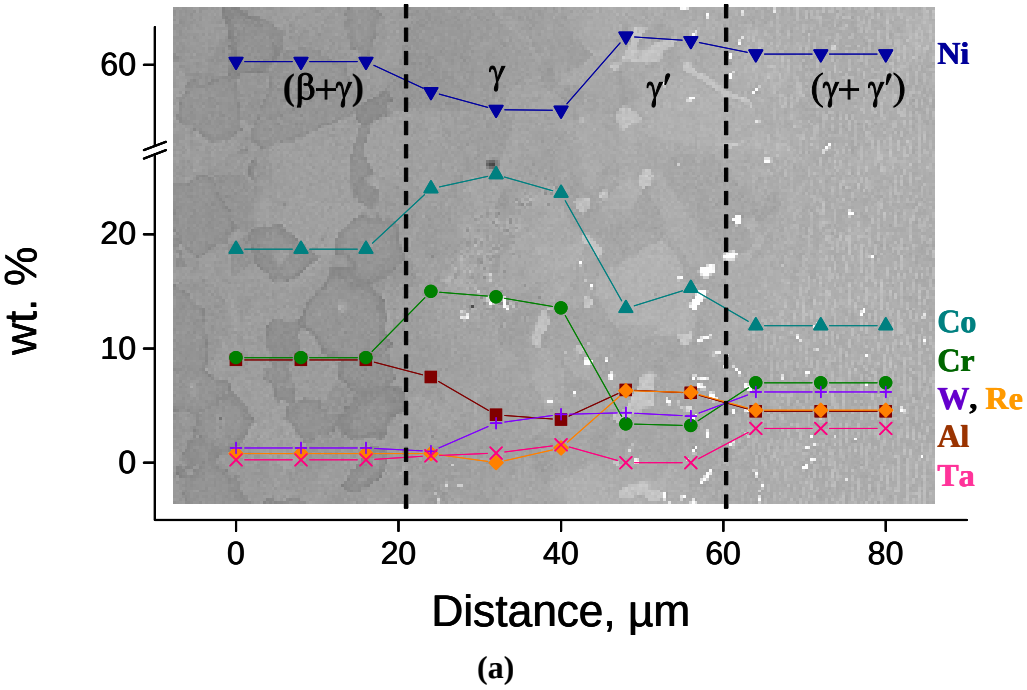

(a)

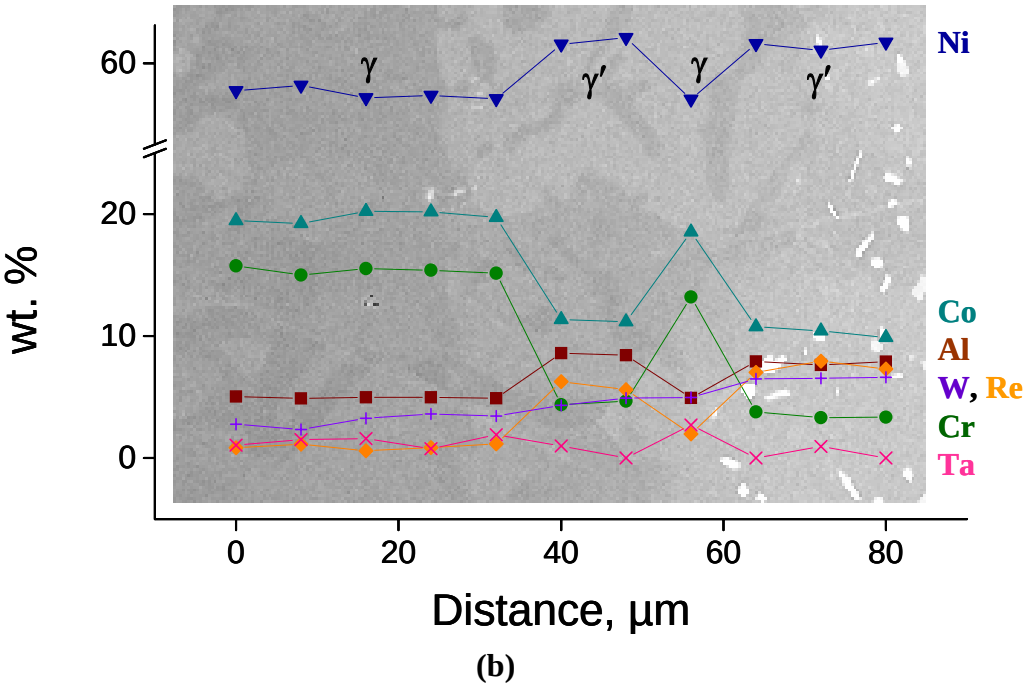

(b)

Figure 5.65 – Composition of interdiffusion zone after (a) OP TMF, (b) OP TMF with dwell time measured by EDX point analysis from Figure 5.64

The higher Al content results in a wider γ′-zone for the specimen after TMF with dwell time at high temperature. Because the solubility of elements such as Cr and W decreased with increase of aluminium content, Cr- and W-rich precipitates form deeper in the substrate.

Compositions of the μ phases presented (Figure 5.66) after TMF tests are given in Table 5.5. Compared to the as received state, the W content in the μ-phase decreased with increasing exposure time at 1050°C under TMF loading, while the Re content increased.

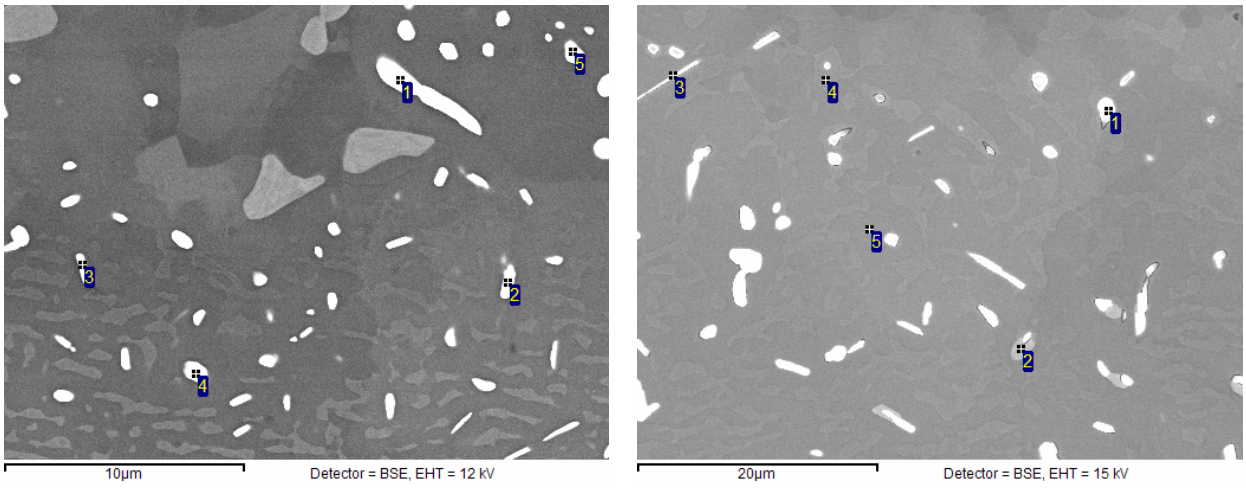

(a) **(b)**

Figure 5.66 - Detailed view of interdiffusion zone with precipitations after: a) OP TMF, b) OP TMF with dwell time

Table 5.5 - Chemical composition of precipitates, **wt%**

	Ni	Al	Co	Cr	W	Ta	Mo	Re	Ti
μ-phase as received	10		16,5	12	36,5	2		23	
μ-phase TMF	11		17,5	11,5	32		2	26	
μ-phase TMF with dwell time	12		10.5	11,5	30	2	2	32	

As a next step, EBSD was applied to image the orientation of the BC grains and single crystal nature of the substrate in the as received state, as well as its evolution under TMF with dwell time testing (Figure 5.67, 5.68).

EBSD-quality mappings in Figures 5.67.a and 5.68.a allowed the depiction of the scale structure. Small grains all over the thickness of the BC were found in the as received state. In contrast, the BC after TMF with dwell time exhibits coarse grains. The substrate affected zone lost the single crystal orientation and the recrystallization process can be clearly seen. Moreover, the orientation mappings presented in Figures 5.678.b-f and 5.68.b-f indicate that no preferred crystallographic growth direction exists for the grains in the interdiffusion zone.

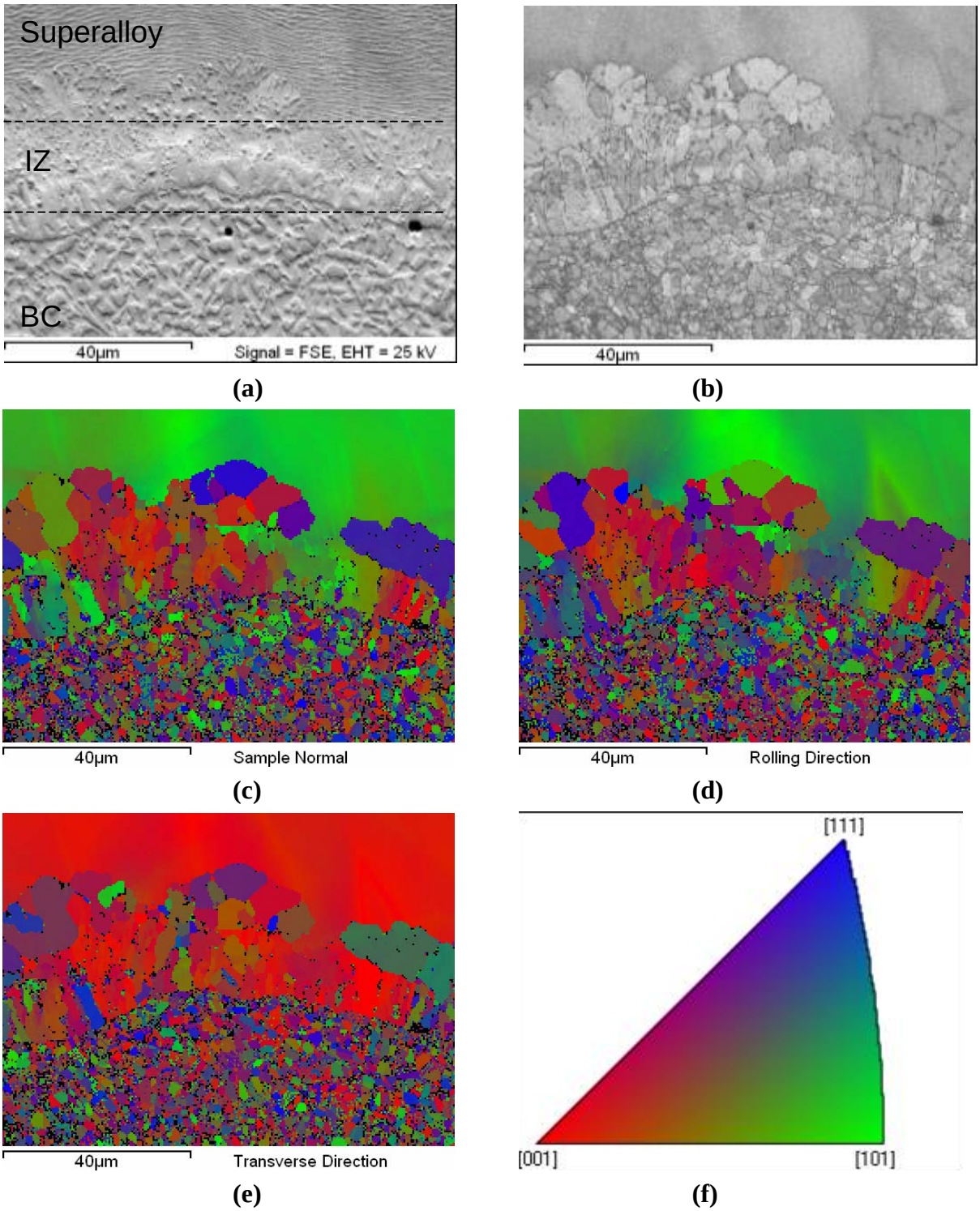

Figure 5.67 – (a) EBSD quality mapping and (b-f) orientation mapping of interdiffusion zone in TBC in as received state

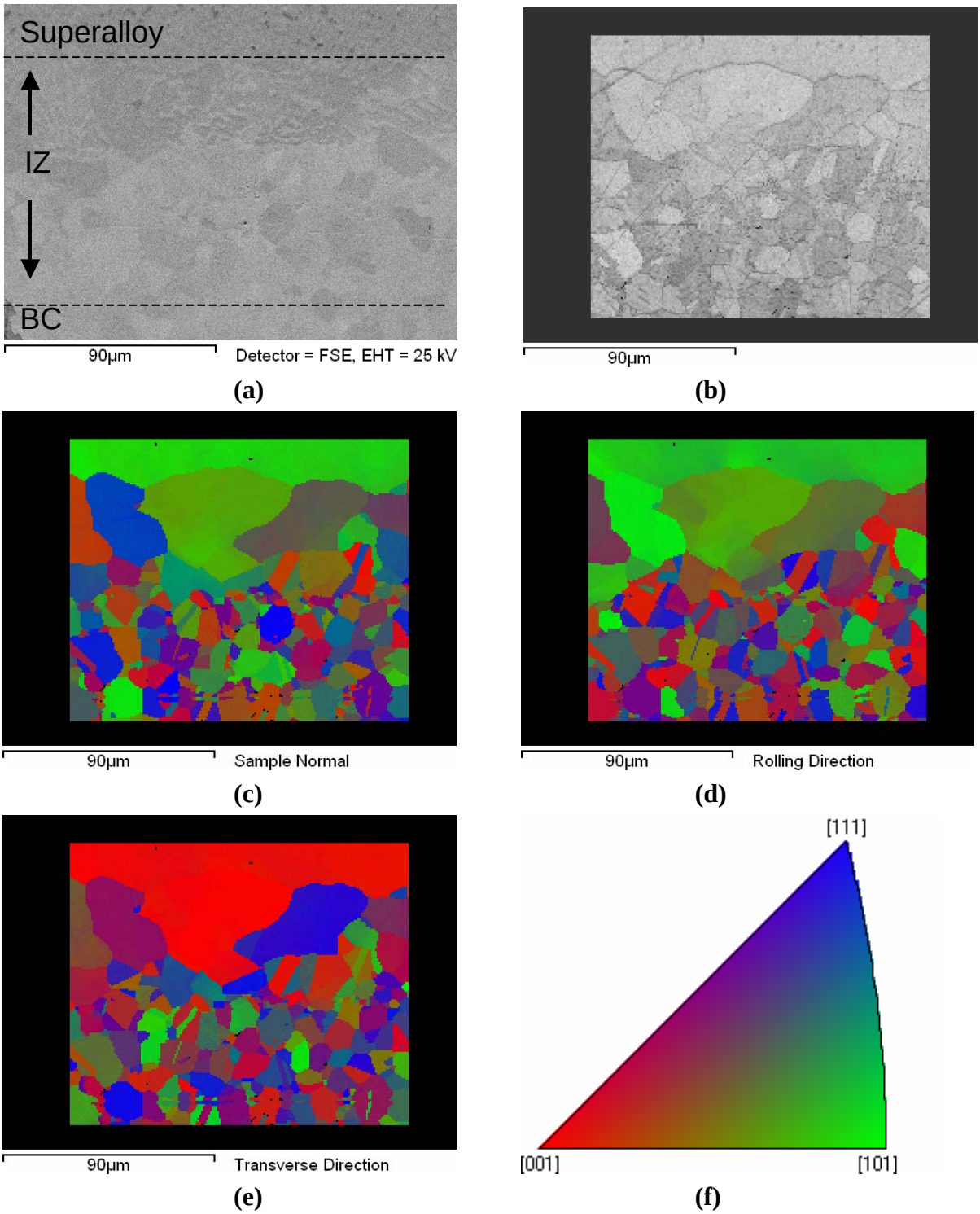

Figure 5.68 – (a) EBSD quality mapping and (b-f) orientation mapping of interdiffusion zone in TBC after OP TMF with dwell time

5.3.2.2 Cracking mechanism

Under OP TMF testing, the TBC specimen experiences high tensile stresses at lower temperatures and compressive stresses develop at the maximum temperature. However, the mechanical responses of the substrate and coatings differ significantly. The crack growth assumed to occur during the low temperature part of the cycle, when the BC shows brittle deformation behavior. The oxide scale formed during the high temperature part of the TMF cycle at the crack tip is ruptured under tensile stresses and the crack propagates. Eventually the stress intensity factor at the crack tip reaches a critical value and the sample fails within a few cycles. Thus, crack growth is controlled by both oxidation and fatigue damage.

A simple way to account for the interaction between fatigue and oxidation is to superimpose both kinds of damage, as proposed in [88]. The damage equations were derived assuming that the elementary crack advance results from an advance due to crack opening under fatigue and from an additional contribution due to oxidation at the crack tip. The damage equation can be written as follows:

$$\frac{da}{dN} = \left(\frac{da}{dN}\right)_{fat} + \left(\frac{da}{dN}\right)_{ox} \qquad \text{Eq. 5.1}$$

Thus, the cyclic to high temperature exposure ratio within the TMF cycle might be responsible for crack propagation mechanism, as shown below for the TMF test without and with dwell time at high temperature.

TMF without dwell time

Figure 5.69 shows the fatigue crack growth in the BC and the subsequent penetration of some cracks into the substrate material after OP TMF testing.

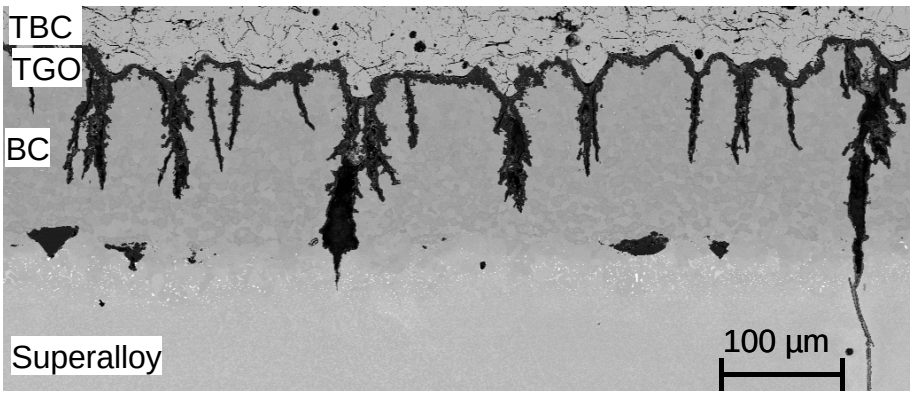

Figure 5.69 – Fatigue crack growth under OP TMF

The crack length was measured using 4 pictures with the same magnification, which resulted in an analysis of 21 mm of the axial specimen length and the respective distribution was elaborated, as shown in Figure 5.70. The bar graph is generated by counting the number of cracks, which belong to a pre-defined crack length interval of 10 µm.

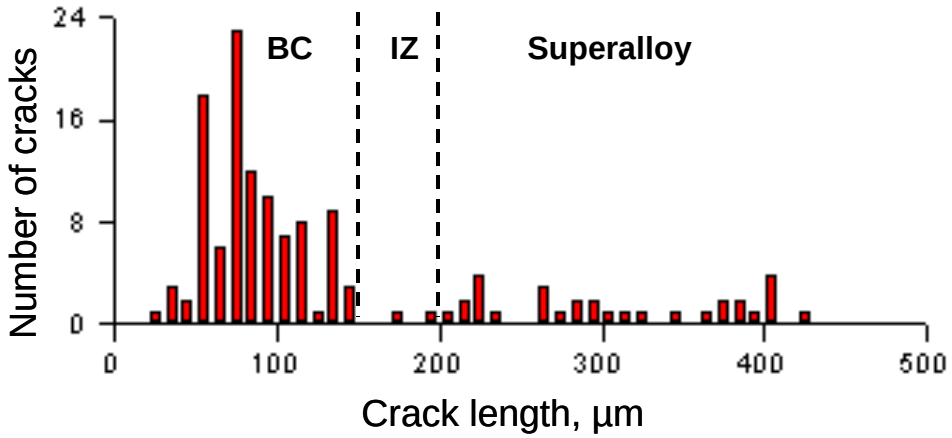

Figure 5.70 – Fatigue crack length distribution after OP TMF

Most of the fatigue cracks are stopped within BC, whereas only few of them stopped within the interdiffusion zone between the BC and base material (crack length <200µm). The minimum crack length was about 30 µm, which corresponds to the width of the β-depleted zone below the TGO/BC interface. Some cracks penetrated the base material and had a length of up to 430 µm. One such crack finally became of macroscopic size and caused the base material fracture.

The SEM pictures of cracks stopped within the BC and the high magnification images of the crack tips are presented in Figure 5.71. An important observation is that cracks within the two-phase BC were deflected many times into the direction of β-phase particles (Figure 5.71.b). Thus, crack growth in two-phase BC was decelerated by the presence of the β-phase.

Crack flanks were covered with oxide scales, with fine cracks at the crack tip (Figure 5.71.c). No crack penetration was found into the γ-phase. This proves suggestion that crack growth at this stage is controlled by oxidation when crack propagation occurs during the low temperature stage of the cycle by oxide rupturing at the crack tip under tensile stresses.

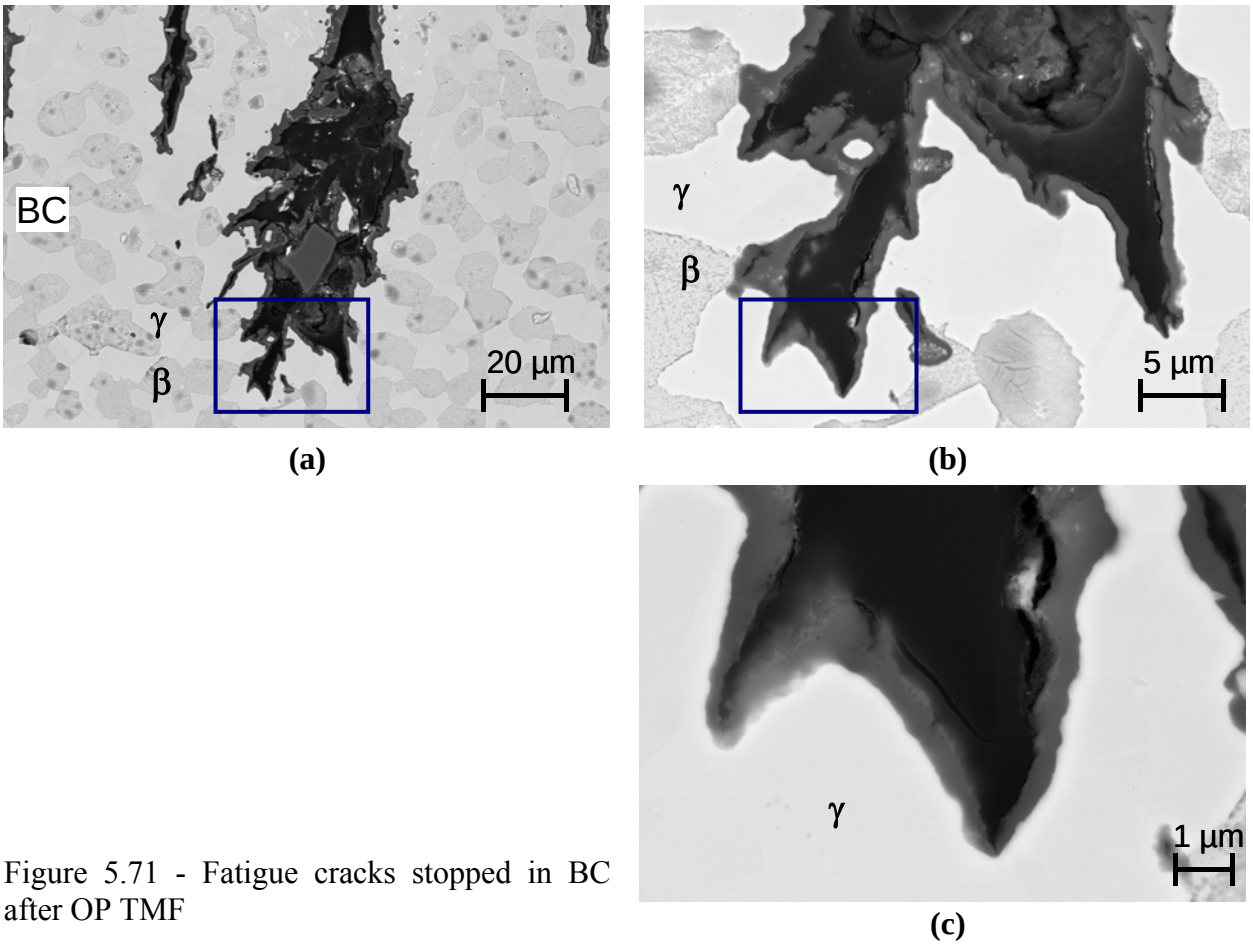

Figure 5.71 - Fatigue cracks stopped in BC after OP TMF

In order to get more information about the interaction between fatigue crack growth and β-phase depletion within BC, the crack length distributions for specimens pre-oxidized before TMF loading for 300, 1000 and 2000 hours were evaluated, as shown in Figure 5.72. Pre-oxidation treatment resulted in β-phase depletion zones in the BC of about 40 µm, 60 µm and 90 µm, respectively. This corresponded to an increasing minimum fatigue crack length. At the same time, no cracks stopped within the β-depleted zone below TGO were observed. Thus, it can be concluded that crack propagation within the β-phase depleted BC was faster than in the two-phase BC.

Furthermore, cracks were observed penetrating the interdiffusion zone between BC and superalloy and then into base material independent on pre-oxidation treatment. Thus, fatigue damage mechanism was predominant and affected the base material failure mode.

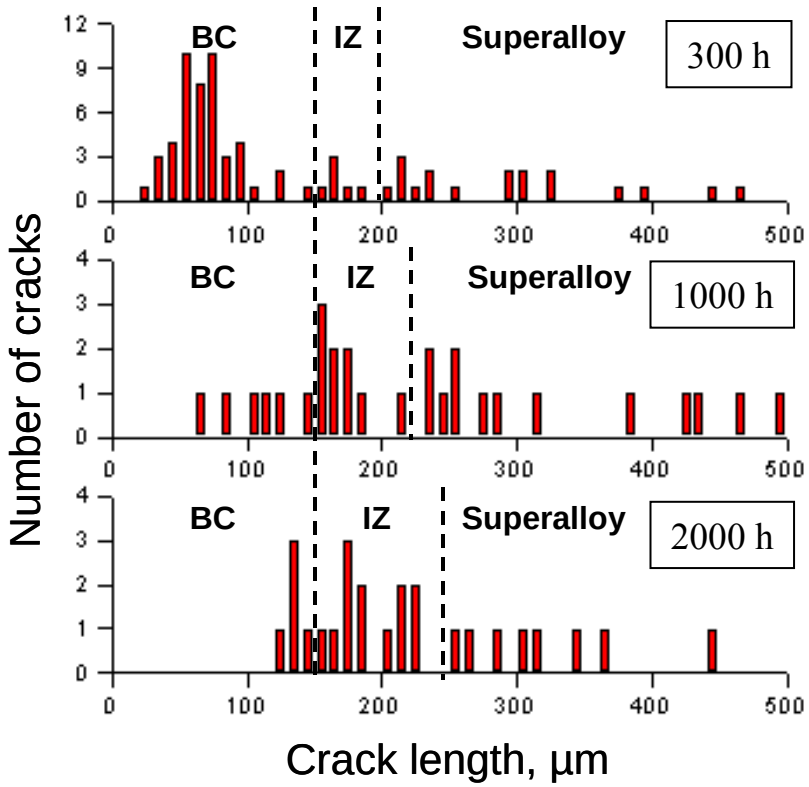

Figure 5.72 – Fatigue crack length distribution after OP TMF with different pre-oxidation treatments

With the aim to investigate the influence of high temperature exposure within the TMF cycle on the fatigue crack growth controlled mechanisms, more detailed analysis of crack propagation within interdiffusion zone was conducted.

TMF with dwell time

As already mentioned in section 5.4.1.2, all fatigue cracks after TMF with dwell time were stopped within the BC or in the interdiffusion zone. A quantitative analysis of crack length measured on a longitudinal section is presented in Figure 5.73.

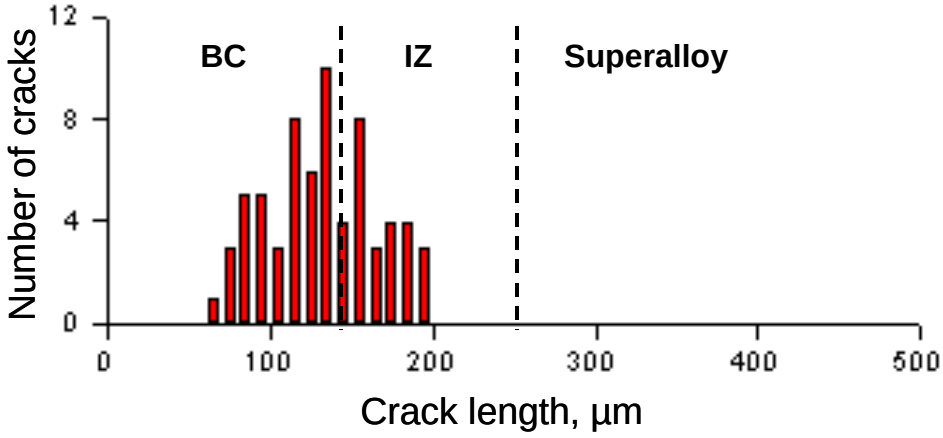

Figure 5.73 – Crack length distribution after OP TMF with dwell time

Some cracks were found to stop within BC, mainly where β-depletion was not complete. In this case, the minimum crack length corresponded to the width of β-depleted zone, as was also observed for TMF without dwell time after pre-oxidation treatments. Most of the cracks propagated to the BC/superalloy interface and stopped within the interdiffusion zone.

As was shown in the previous section, the interdiffusion zone developed under TMF with dwell time consisted of both γ and γ′ phase (Figure 5.74). The γ′-particles were found to act as obstacles for crack propagation.

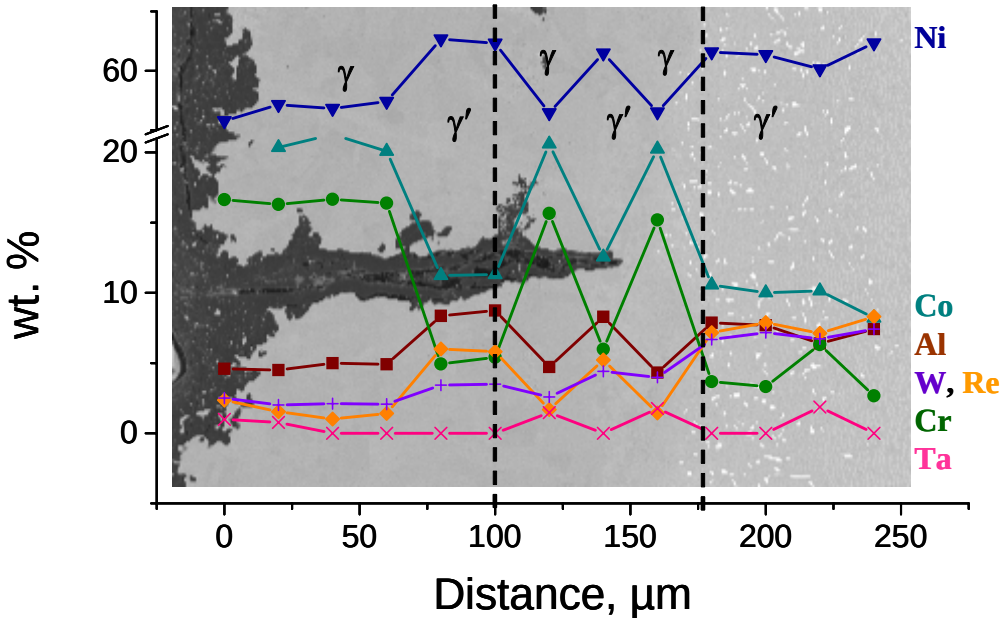

Figure 5.74– Composition of BC and interdiffusion zone after OP TMF with dwell time measured by EDX point analysis

Figure 5.75 displays detailed views of the crack tips with measured IZ phase composition using EDX-analysis. Fine cracks at the crack tips (Figure 5.75.c and f) did not penetrate into the γ′-particle for either represented fatigue cracks.

Moreover, from EBSD-quality mappings (Figure 5.76) it can be seen that γ′ particles were formed within the substrate-affected zone as a result of the recrystallization process in the single crystal base material.

Therefore the fatigue crack growth under TMF with dwell time is controlled predominantly by oxidation and interdiffusion kinetics.

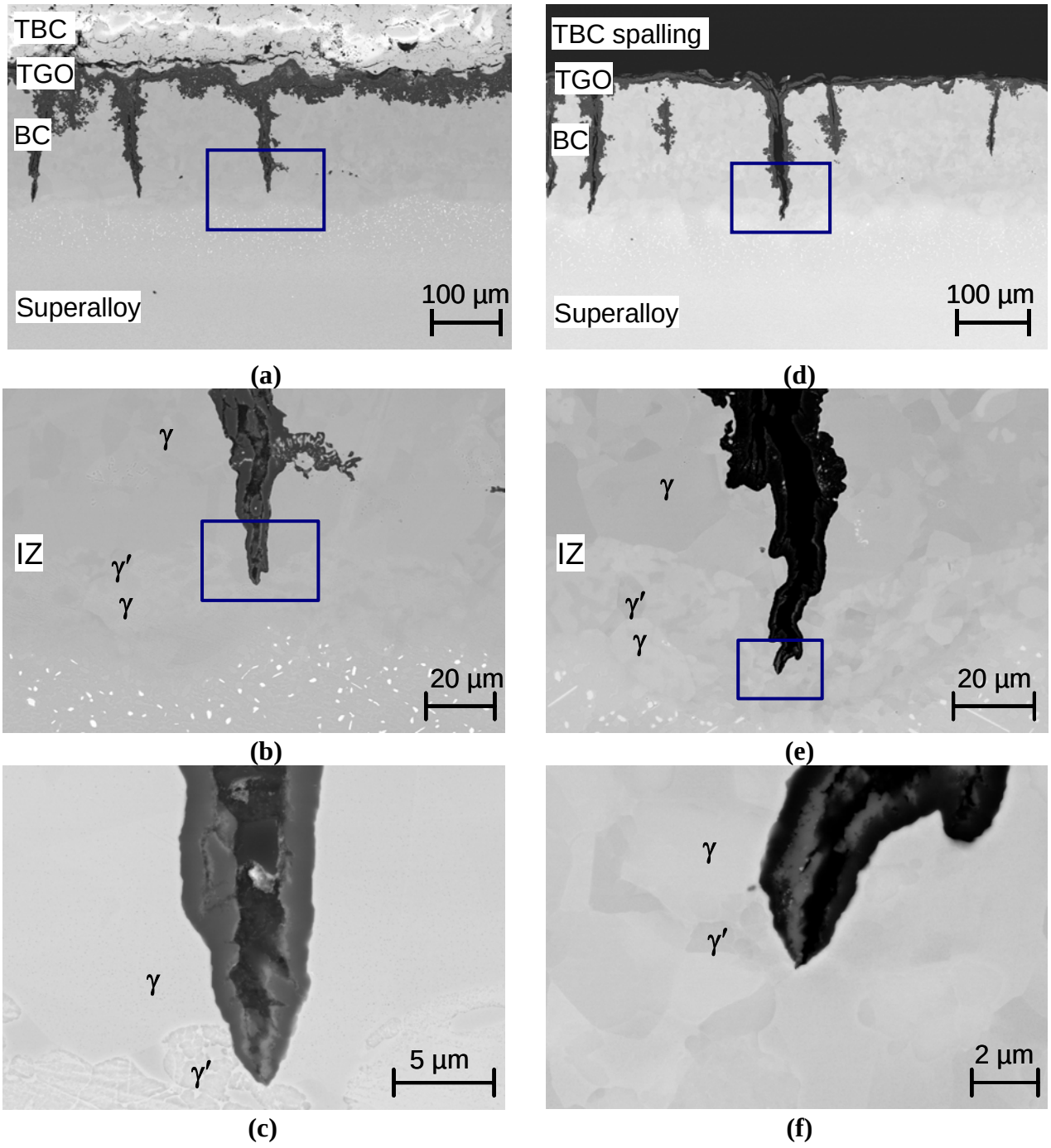

Figure 5.75 – Fatigue cracks stopped in interdiffusion zone after OP TMF with dwell time

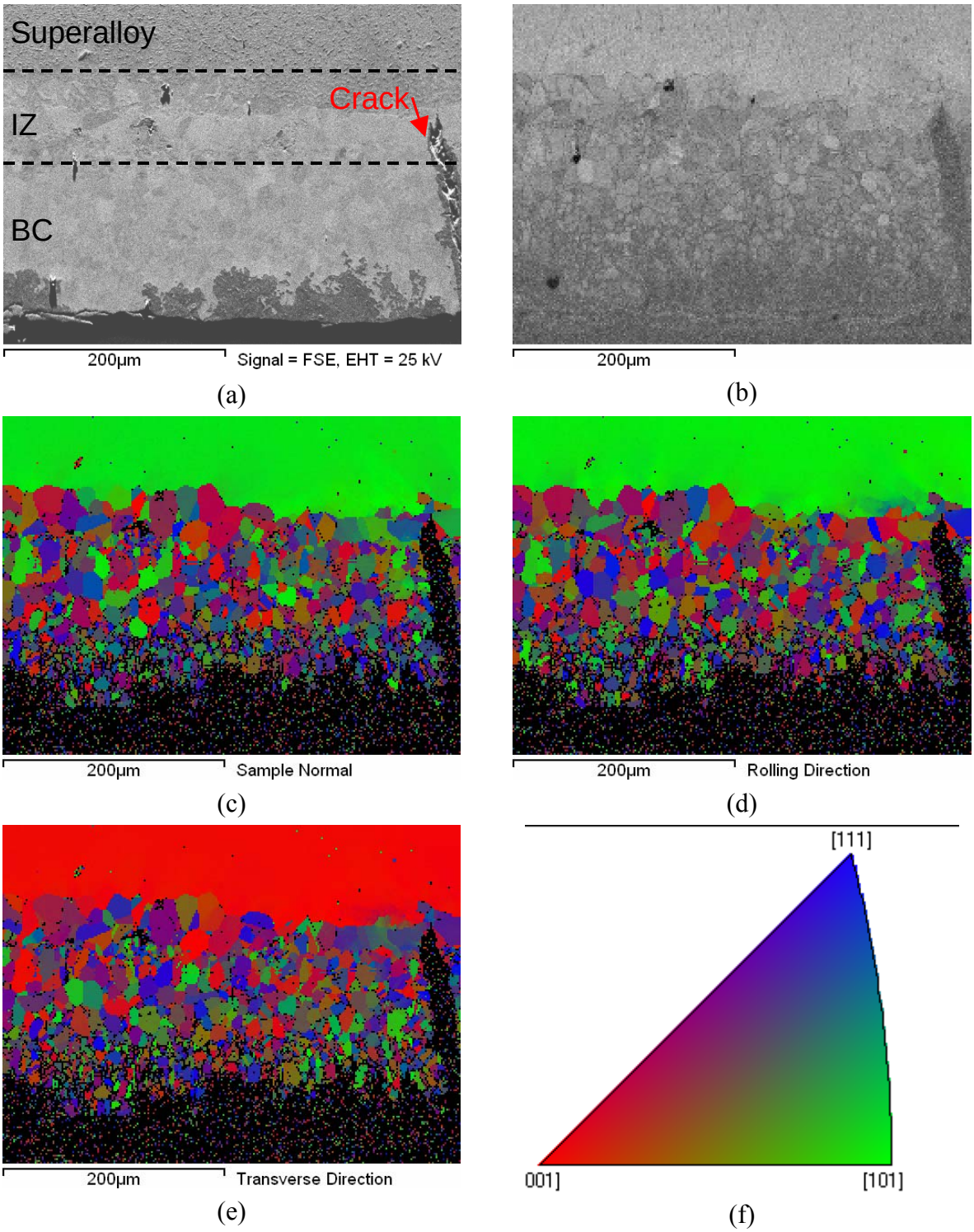

Figure 5.76 – (a) EBSD quality mapping and (b-f) orientation mapping of BC with crack stopped in interdiffusion zone after OP TMF with dwell time

The fatigue crack growth mechanisms under different TMF tests discussed above can be summarized as following:

1. TMF without dwell time: decelerated crack growth due to branching effect within two-phase BC, accelerated within superalloy;
2. TMF with dwell time: oxidation (β-depletion) kinetics controlled crack growth within BC, γ′-stopping effect within interdiffusion zone.

Influence of β-depletion kinetics was limited under TMF without dwell time, whereas no evidence for slower crack growth than β-depletion kinetics was found. Thus, crack growth under predominant fatigue or oxidation damage depending on the TMF loading can be distinguished, as shown schematically in Figure 5.77.a and b, respectively.

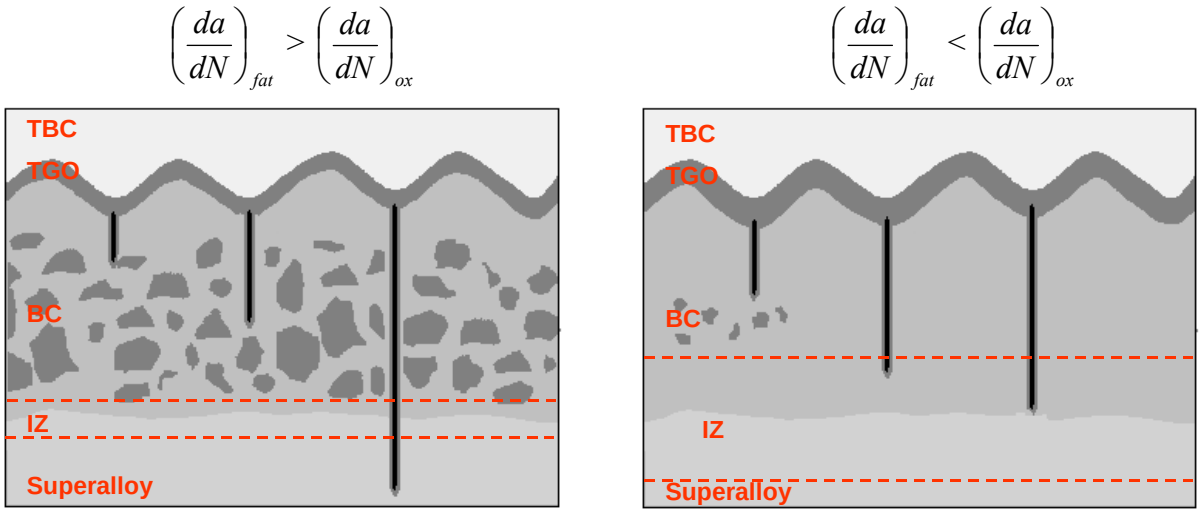

(a) (b)

Figure 5.77 - Schematic of fatigue crack growth under TMF loading: a) TMF without dwell time, b) TMF with dwell time

5.4 Damage mapping

In Table 5.6 the results for lifetime, TGO thickness and delamination crack observed for the main six load profiles are summarized.

It is clear that the lifetime is higher for one-component loading and that it decreases with the introduction of the second and third components. For example, the lifetime of TBC under isothermal exposure was 4490 hours. With the introduction of the cyclic component (cyclic oxidation), it decreased to 1400 hours and under cyclic oxidation with a temperature gradient, it was only 112 hours. The same tendency was observed for cyclic lifetime: failure of TBC under thermal cycling occurred after 23500 cycles, whereas under loading with additional oxidation component (cyclic oxidation) after 700 cycles. For TMF tests, where the mechanical cycling component was present together with thermal cycling, the introduction of the third load component (isothermal exposure) also led to a significant decrease in cyclic lifetime from 1620 to 619 cycles. In turn, if compared with cyclic oxidation in the same

temperature range, time at temperature decreased from 2900 to 1240 hours for three-component TMF loading.

Table 5.6 - Summary of experimental results for six main loading conditions

Nr.	Loading	ΔT, °C	t_f, h	N_f, cyc	d_{TGO}, µm	Failure/ delamination path
1	**Isothermal exposure**	1050	4490	-	13	Delamination in TGO/TBC
2	**Thermal cycling**	60 - 1050	-	>23500	3.5	Delamination cracks in TBC, (fatigue cracks in BC)
3	**Cyclic oxidation**	60 – 1050 350-1050	1400 2880	700 1440	10 12	Delamination in TGO/TBC
4	**Cyclic oxidation with temperature gradient**	60 – 1050 (BC) – 1150 (TBC)	112	56	5	Delamination in TBC
5	**TMF OP**	ΔT=350-1050°C Δε= 0.6 %	-	1620	4	Fatigue failure of base material, (delamination cracks in TBC)
6	**TMF OP with dwell time**	ΔT=350-1050°C Δε= 0.6 %	1240	619	12	Cracks in BC, delamination in TGO/TBC

The respective failure modes as well as crack paths where also found to be strongly dependent on the loading composition, as shown schematically in Figure 5.78. Increasing the cyclic component in the thermal loading profile led to a consistent shift of the delamination crack toward the TBC. This was accompanied with a decrease in the average TGO thickness formed from 13 µm for isothermal exposure to 10 µm for cyclic oxidation and only 3.5 µm for thermal cycling. Under thermal cycling in addition to delamination crack, thermal fatigue cracks were observed in the BC. Additionally imposed thermal gradient under cyclic oxidation also led to the delamination crack path shifting close to the TBC and more damages within the ceramic top coat. The average TGO thickness was about 5 µm.

For TMF loading, the same influence was found for an increase in the cyclic component as for thermal loading with regard to the delamination crack path. However, only in the case of TMF with dwell time the delamination failure occurred before the fatigue failure of base material. The average TGO thickness was 12 and 4 µm for TMF with dwell time and without, respectively.

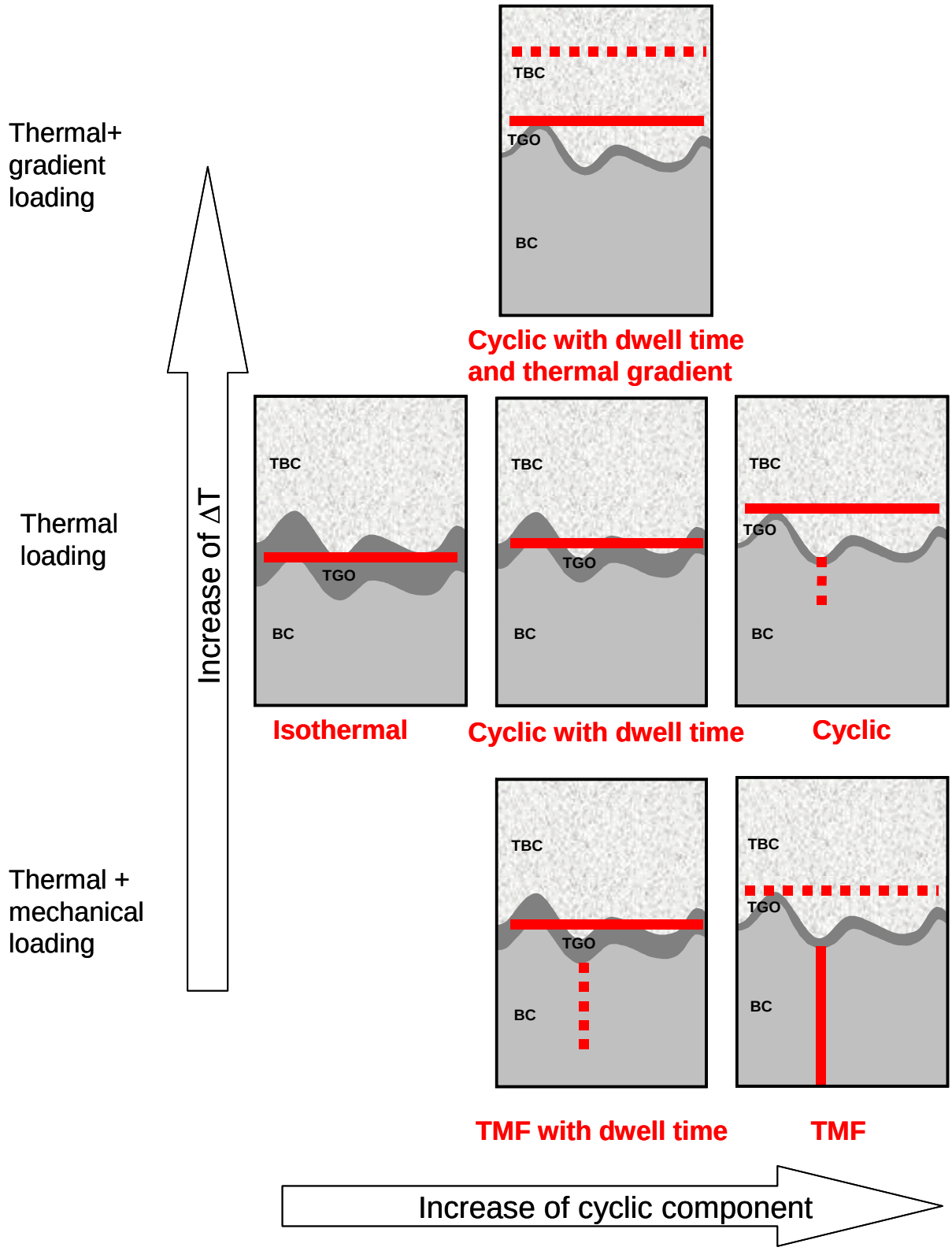

Figure 5.78 – Correlation between loading parameters and failure modes

5.5 Deformation properties of ceramic top coating

The stress state in the ceramic thermal barrier coatings (TBCs) during service is affected not only by elastic properties, but also by time dependent (creep) deformation and stress relaxation due to creep or creep-like processes at high temperatures. In order to investigate the deformation properties, free-standing plasma-sprayed TBCs consisting of zirconia doped with 7- 8 wt% yttria were manufactured as thin-walled, hollow cylindrical specimens. Compressive constant load and constant rate tests were carried out on these specimens. The work aimed at generating a deformation data set for plasma-sprayed TBCs with realistic structure and at clarifying the influence of the micro and defect structures on deformation.

5.5.1 Compressive deformation

Figure 5.79 displays examples of experimentally determined creep curves under constant compressive load at various temperatures. The time dependent increase of deformation was revealed to be fairly fast at 1150°C and 1050°C and even at 950°C. Total deformations of around 3% at 1150°C and 1050°C were observed within 10 and 230 hours, respectively. At 950°C, a total strain of approximately 0.8% was observed after 100 h, comprising an elastic strain and a time dependent permanent strain of more than 0.4 %. It should be noted that the low stiffness of approximately 25 GPa of the APS TBCs resulted in an elastic strain of approximately 0.4%.

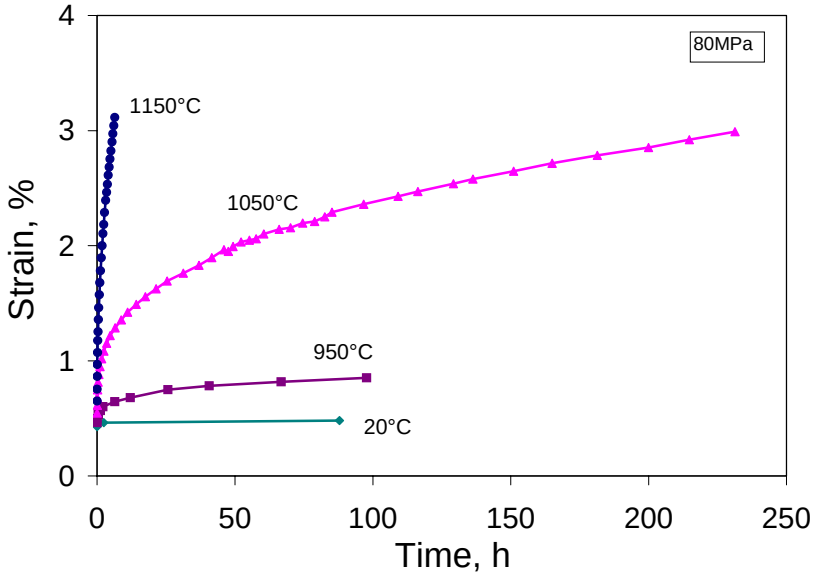

Figure 5.79 - Total compressive strain versus time at various temperatures for an initial stress of 80 MPa and various temperatures

Figure 5.80 represents deformation rates for a load of 80 MPa corresponding to the creep strain curves in Figure 5.79. Using this representation, as afore mentioned, fast deformation can be more directly noticed with concrete rate values. In the high temperature range (950-1150°C), the resulting deformation rates immediately after loading were between $4 \cdot 10^{-6} s^{-1}$ and $2 \cdot 10^{-5} s^{-1}$. Altogether, the rate values were above or close to $10^{-6} s^{-1}$ at 1150°C and above $10^{-8} s^{-1}$

at 1050°C. The values decreased continuously with increasing compressive deformation, typical for primary creep stages. At 1050°C and 1150°C, relatively small changes between 2 and 3% of total deformation were observed indicating a subsequent minimum or steady state. At 950°C the deformation rate decreased steeply from $4 \cdot 10^{-6} s^{-1}$ to values below $10^{-8} s^{-1}$ before 1% total strain was achieved. Surprisingly, even at room temperature the deformation response after load application revealed a time dependency.

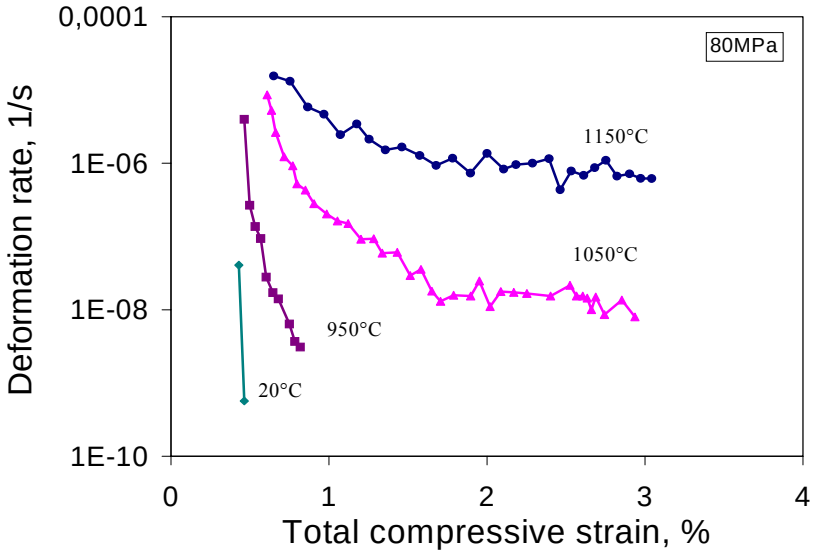

Figure 5.80- Deformation rate as a function of total compressive strain for an initial stress of 80 MPa and various temperatures

The stress dependence of the deformation rate at constant temperature is shown in Figure 5.81 for 40, 80 and 120 MPa at 1150°C. The rate at 3% total compressive strain increased by a factor of 50 when the stress was increased from 40 to 120 MPa.

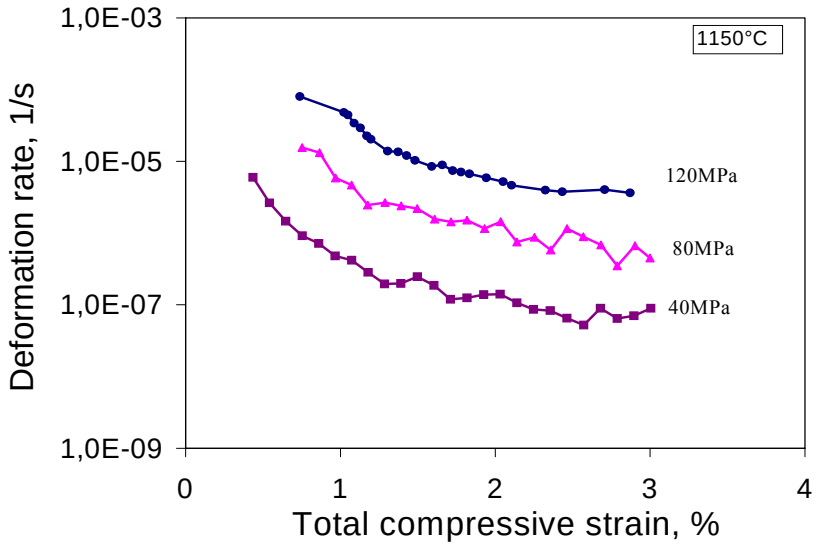

Figure 5.81 - Deformation rate as a function of total compressive strain for 40, 80 and 120 MPa at 1150°C

Figure 5.82 displays stress-strain curves resulting from constant rate tests at RT, 950°C, 1050°C and 1150°C. The fracture strain increased with increasing temperature. It was

approximately 1.2% at room temperature, 2.2% at 950°C, 2.5% at 1050°C and approximately 3% at 1150°C (all values as total compressive strain). The fracture strain showed only a weak dependence on deformation rate (between $10^{-6}s^{-1}$ and $10^{-4}s^{-1}$). In contrast, the maximum stresses revealed a strong rate dependency. At 1150°C, the beginning of a stress plateau is indicated at 3%.

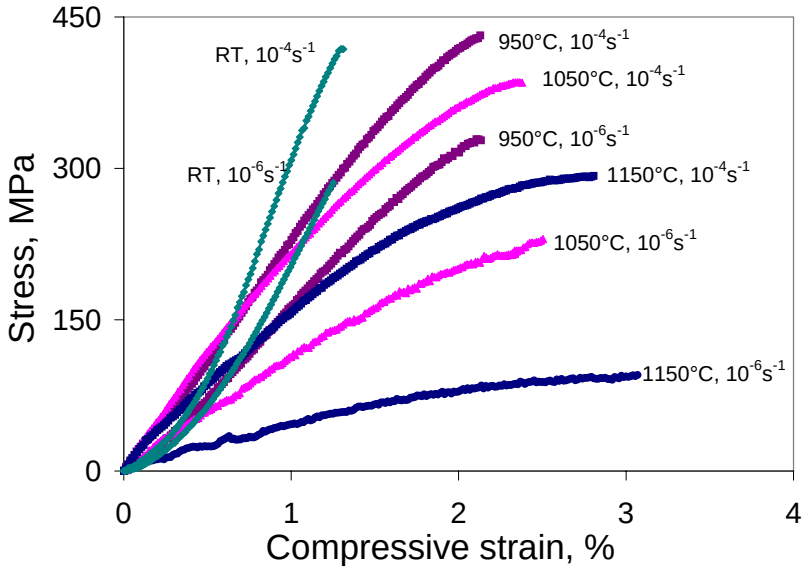

Figure 5.82 - Stress-strain curves determined with constant rate tests at RT, 950°C, 1050°C and 1150°C

Figure 5.83 represents the deformation rate as a function of time for (a) various temperatures at constant stress and (b) various stresses at constant temperature. The graphs correspond to the data plotted in Figure 5.80 and Figure 5.81. The current results are in general agreement with the formerly reported data. In the time representation, the variation of deformation rate with temperature at a constant stress for equal times, as well as the variation of stress at a constant temperature for equal times shows much smaller values than the strain representation.

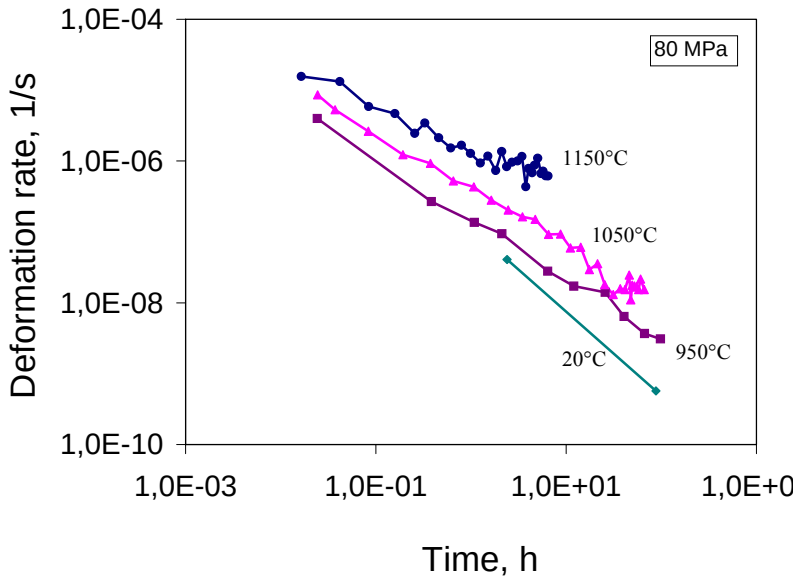

(a)

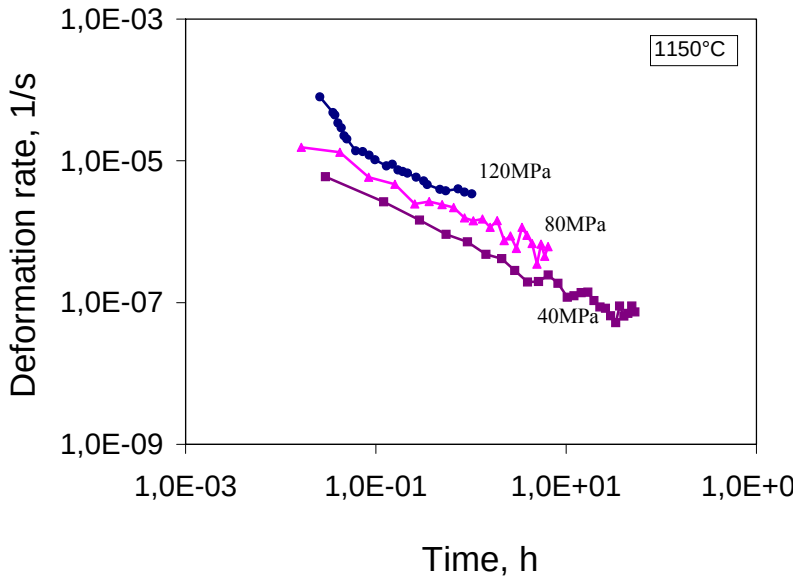

(b)

Figure 5.83 - Deformation rate as a function of time: a) for various temperatures at 80 Mpa; b) for various stresses at 1150°C

The deformation rate and stress values from all experiments in the temperature range 950-1150°C were used to derive a Norton diagram for the plasma-sprayed YSZ TBC (Figure 5.84). In the case of the constant load experiments, minimum deformation rates in the range of 2-3% total compression strain were taken together with the corresponding initial stress values. In the case of constant rate experiments, the maximum stress values in the range of 2-3% total compressive strain were taken together with the applied deformation rate.

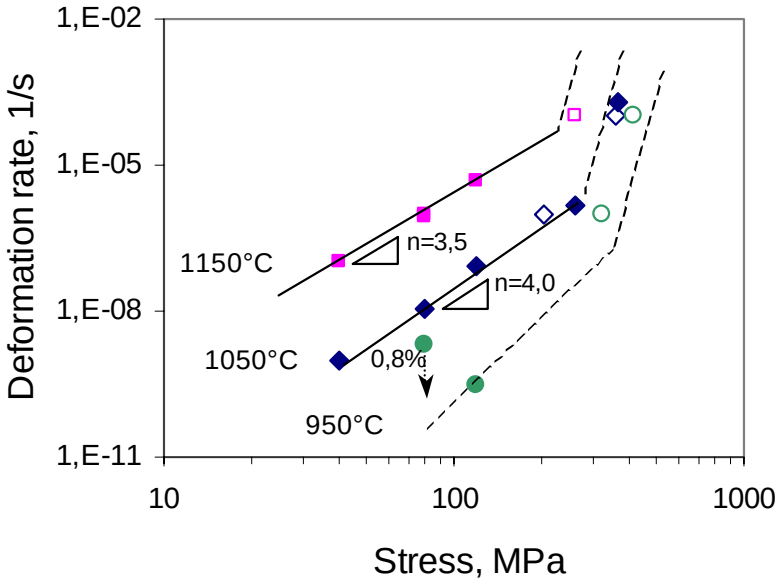

Figure 5.84 - Deformation rate vs. stress for 950, 1050 and 1150°C. Solid symbols represent minimum deformation rates from constant stress experiments. They were taken from the range of 2-3% total compression strain, where the rate revealed only a weak strain dependency. One data point at 950°C was taken at a total compressive strain of about 0.8%, at which the test was interrupted. Open symbols represent the deformation rate-stress data from constant rate experiments. The corresponding stress values are maximum values of the stress-strain curve from the range of 2-3% total compressive strain.

As indicated in Figure 5.84 by straight lines, the data at 1150°C and 1050°C follows a power law such as

$$\dot{\varepsilon} = A \cdot \sigma^n \qquad \text{Eq. 5.2}$$

for medium stresses. The evaluation of the stress exponent n resulted in values of 3.5 and 4.0 at 1150°C and 1050°C respectively. These values hold for stresses between 40 and approximately 200 MPa at 1150°C and 300 MPa at 1050°C. Larger stresses led to a stronger stress dependence of the deformation rate. The assumption of a power law breaks down in this regime would be consistent with experimental data.

The elastic modulus of TBCs or rather the stiffness determines the stress level in the ceramic top coat and is thus a major life-time parameter. In order to determine the influence of compressive deformation on macroscopic stiffness, a couple of creep tests were interrupted before the specimens failed. The stiffness was then determined from instantaneous strain changes during rapid unloading to a stress value of approximately 1 MPa. Tests were carried out at various temperatures after certain creep deformations, as well as for the initial state. Results are displayed in Figure 5.85.

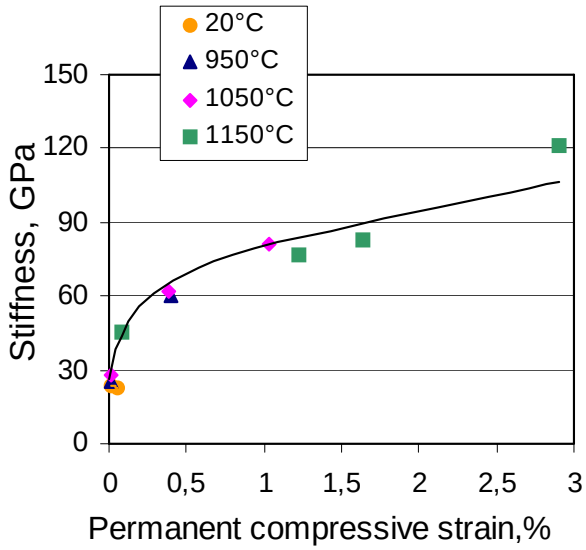

Figure 5.85 - Dependence of macroscopic TBC stiffness on permanent compressive strain after constant load deformation at various temperatures.

The stiffness of as sprayed material was about 25 GPa. After a relatively small constant load deformation at room temperature (100 h, 0.05% permanent compressive strain), the stiffness remained virtually unchanged. Compressive deformation in the range of 950°C-1150°C led in contrast to a large increase. The stiffness was approximately 60 GPa at 950°C after 100 h constant loading (0.4% permanent compressive strain) and increased by a factor of about five at 1150°C after creep deformation (2.8% permanent compressive strain). The curve indicated in Figure 5.85, which roughly fits all temperature data, suggests that the stiffness increase depends more on permanent strain than on temperature. In contrast to the large increase in stiffness at higher strain values, high temperature exposition without mechanical loading for 100 h at 1150°C resulted in an increase in stiffness of not more than 50% of the initial value [32]. Thus, permanent compressive deformation may affect the stiffness more than pure annealing. This result should be considered, when changes in the material properties of TBCs during service become a design issue, given that the TBC experiences high compressive strains during heating and at high temperatures.

5.5.2 Microstructural changes

In order to obtain more information about microstructural changes, which are linked with compressive deformation, two approaches were carried out: (i) in-situ observation of microstructure at room temperature and (ii) comparison of microstructure after high temperature deformation with the initial microstructure by means of SEM.

The first approach, in-situ observation of microstructure during compressive deformation at room temperature, was carried out using a micro-mechanical device, which was built in a SEM. The microstructural changes could be monitored at high magnifications. In the case of

high temperature deformation experiments, the micrographs were taken from the very same location before and after deformation.

5.5.2.1 As received microstructure

The typical plasma-sprayed microstructure consists of flat lamellar splats with spatial dimensions of about 10 (height) to more than 100 µm (lateral diameter) (see Figure 5.86). Grains within splats are oriented parallel to the spray direction and have an elongated columnar shape. They can be characterized by an average diameter of roughly 0.5 µm and an aspect ratio of >10:1. Defect population consists mainly of inter-splat cracks and intra-splat cracks. Inter-splat cracks are oriented mostly parallel to the coating plane (perpendicular to the spray direction) whereas intra-splat cracks are oriented mainly perpendicular to the coating plane.

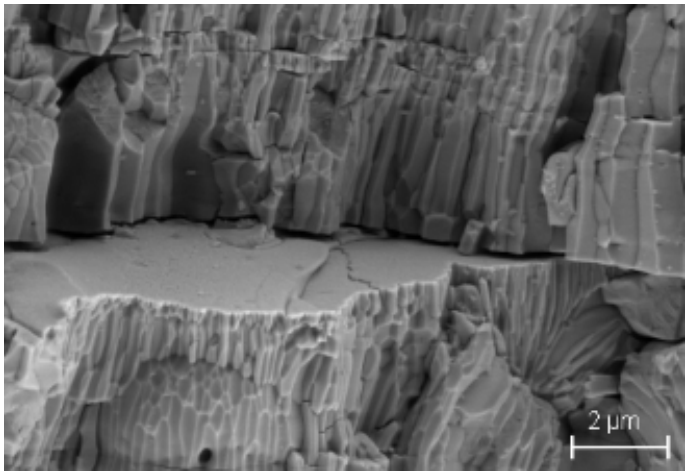

Figure 5.86 – Plasma-sprayed TBC microstructure in as received state

5.5.2.2 In-situ deformation in SEM at room temperature

In-situ observation of the microstructure during compressive deformation was carried out at room temperature using the micro-mechanical device, which was built in the SEM. The microstructural changes could be monitored at high magnifications. In the case of high temperature deformation experiments, the micrographs were taken from the very same location before and after deformation.

The free-standing coatings were deformed along the cylindrical axis, i.e. the applied stress was oriented parallel to the coating plane. Figure 5.87 represents the view of the polished cylinder surface during in-situ observation. The left image represents the structure before deformation and the right at about 2% compressive deformation. The upper area of the micrograph displays a splat from the side and the lower area presents the surface of another splat. As a consequence of the plasma-spraying process, the splat becomes less anisotropic in

orientation with increasing coating thickness and the splats themselves become bended in a complex manner. This led to the fact, that some splats at the cylinder surface can be seen from the top and the side simultaneously (see also Figure 5.88.a).

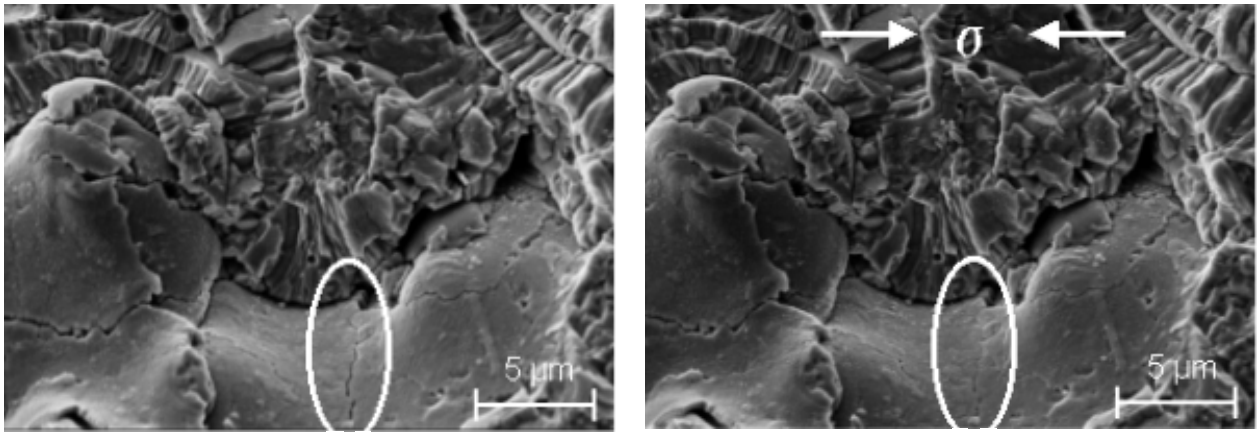

(a) (b)

Figure 5.87 - SEM micrographs of the surface of a free-standing TBC before (a) and after (b) a deformation of 2 % at room temperature

The arrows indicate that the material assimilates the macroscopic deformation partly by closing intra-splat microcracks, which are oriented perpendicular to the applied load direction.

5.5.2.3 Deformation under high temperature

Figure 5.88 demonstrates microstructural changes that are correlated with compressive deformation at high temperatures. Figure 5.88.a presents a view of the polished cylinder surface with a lower magnification, an enlarged cutaway view is shown in Figure 5.88.b and Figure 5.88.c shows the deformed structure. The direction of applied stress is indicated. Smaller intra-splat cracks are almost completely closed and healed. The larger intra-splat crack, which is diagonally oriented, is partly closed. Edges of the crack surfaces appear rounded after deformation. Some areas in the lower parts of the image indicate local volume deformation of the splat itself, perhaps in order to adapt geometrical restraints during crack closure. Besides, the grain structure within the splat became visible due to thermal edging.

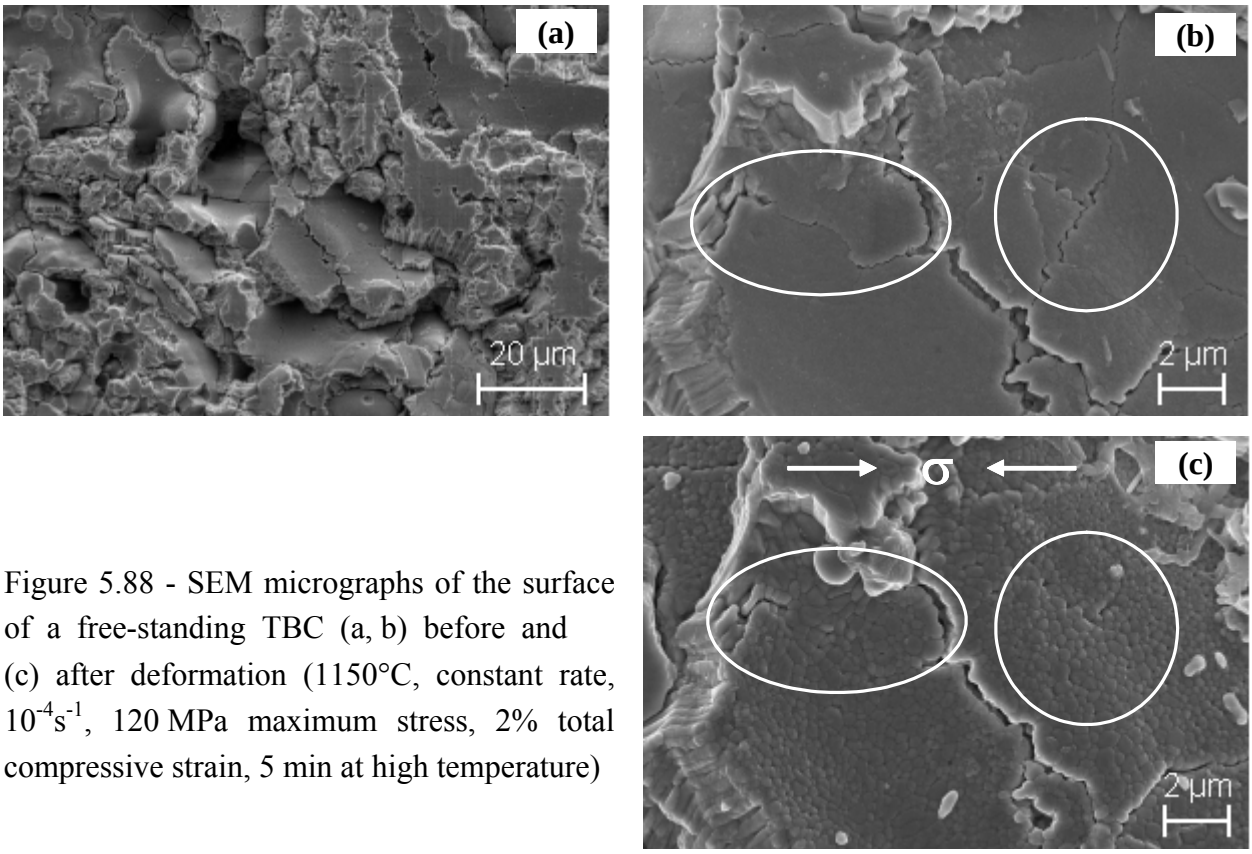

Figure 5.88 - SEM micrographs of the surface of a free-standing TBC (a, b) before and (c) after deformation (1150°C, constant rate, $10^{-4}s^{-1}$, 120 MPa maximum stress, 2% total compressive strain, 5 min at high temperature)

Figure 5.89 represents microstructural changes within a splat after deformation. Again, images (b) and (c) display the structure before and after deformation.

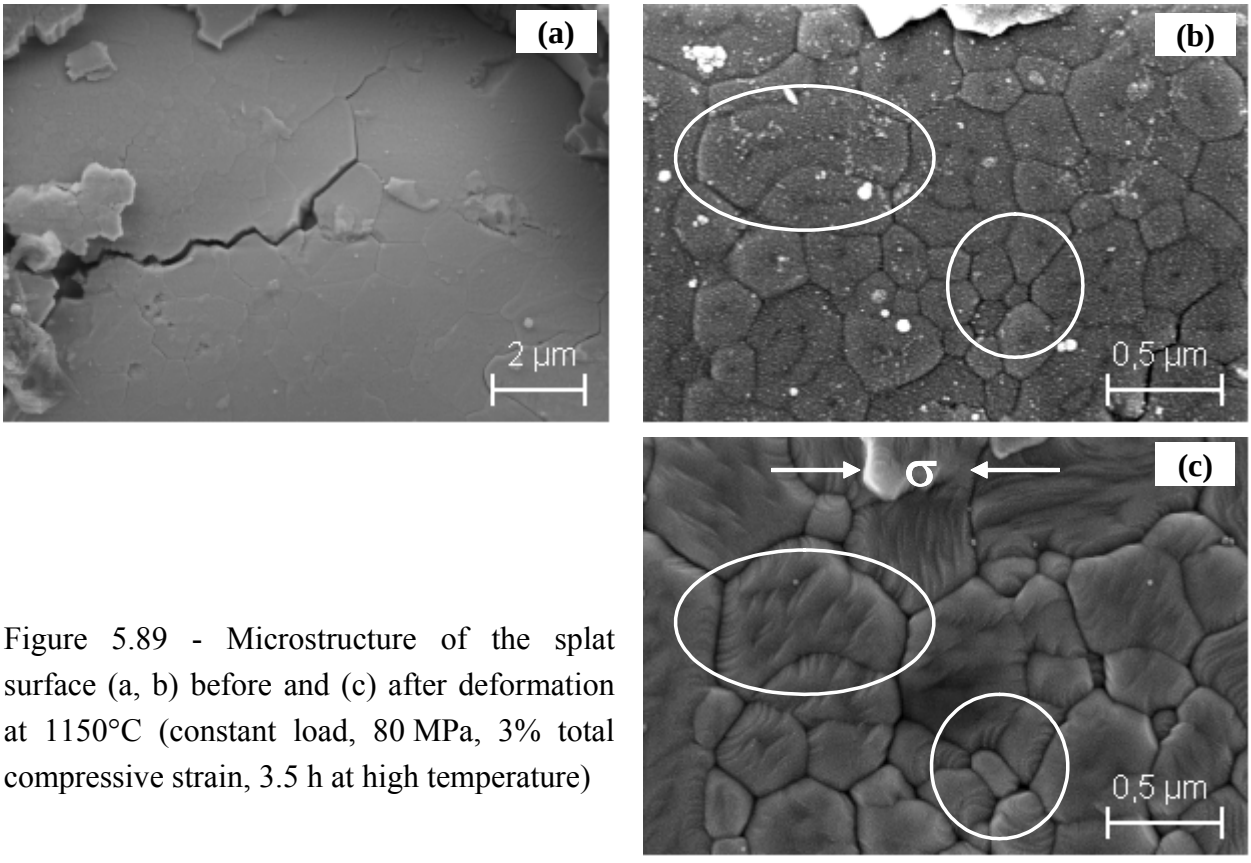

Figure 5.89 - Microstructure of the splat surface (a, b) before and (c) after deformation at 1150°C (constant load, 80 MPa, 3% total compressive strain, 3.5 h at high temperature)

A reduction in the number of grains can be observed. Some smaller grains disappeared in favour of larger grains. Some grains appeared smaller after deformation, however some grains seem to coagulate. Moreover, shape changes took place.

The microstructural changes revealed that the plasma-sprayed TBC assimilates the macroscopic deformation at room temperature partly by closing intra-splat microcracks, which are oriented perpendicular to the applied load direction. After high temperature deformation (1150°C), smaller intra-splat cracks were almost completely closed and healed. A larger microcrack was partly closed and the edges of the crack surfaces appeared to be round after deformation. Local volume deformation was indicated nearby the larger, partly closed intra-splat crack, perhaps in order to adapt geometrical restraints during crack closure. Moreover, a reduction in the number of grains was observed within the splats as well as their shape changes.

6 Conclusions

In order to systematically analyze the influence of the type of load profile on the damage and failure mode of the TBC composite, as well as on the time and number of cycles to failure, and in order to gain more information about the mechanisms and parameters, which control the durability of TBCs, a TBC system consisting of air plasma-sprayed partially stabilized zirconia (ZrO_2-7-8wt.%Y_2O_3) with NiCoCrAlY bond coat onto CMSX-4 substrate was subjected to six types of tests: (i) isothermal furnace tests, (ii) thermal cycling, (iii) cyclic oxidation, (iv) cyclic oxidation with temperature gradient, (v) thermomechanical fatigue, (vi) thermomechanical fatigue with dwell time at high temperature.

Analysis of the damage and failure modes of thermal barrier coatings was based on the representation of these six test types or load profiles as a combination of four basic load components: (i) HT exposure, (ii) thermal cycling, (iii) mechanical cycling, (iv) temperature gradient. The activation of the respective load component was found to have a strong influence on the time and number of cycles to failure and the damage and failure modes, which were distinguished by the particular crack paths along which the macroscopic spallation was developing.

Isothermal oxidation tests (one-component loading: HT exposure) at 1050°C revealed that the thermal exposure was sufficient for the initiation of microcracks within one heating and cooling step and for TBC spallation. Moreover, crack formation and crack propagation processes were developing at ambient temperatures after cooling down, which was monitored using non-destructive methods such as acoustic emission and infrared thermography. The damage evolution was investigated by a series of isothermal tests with increasing exposure times from 5% of lifetime until macroscopic failure occurred. Two stages of damage evolution were distinguished: (i) crack formation and initial crack growth (crack length below 40 µm, TGO thickness < ca 8-10 µm) and (ii) long-range crack growth and linking (TGO thickness > 8-10 µm). Complete TBC spallation after 300 hours at RT, so-called “desktop effect”, was observed for APS thermal barrier coatings exposed for 4490 hours at 1050°C. Damage accumulation at RT and “cold spallation” is assumed to be due to cooling stresses, which generally result from a combination of thermal mismatches and TGO growth, as well as from the humidity of the ambient air.

It was also shown that the longer the dwell time is at lower temperatures, the more damage is accumulated and thus the more lifetime of a TBC coated gas turbine component is consumed. Therefore, the delayed damage evolution in an externally stress free state at room temperature has a direct effect on the service lifetime, particularly for peak load operation of a gas turbine while the service operation of the gas turbine is interrupted.

Under another one-component loading profile - thermal cycling without a HT dwell time, damage occurred at the TBC/TGO interface mainly within the TBC. Minimum high temperature exposure caused the formation of a thin TGO (< 3.5 μm) even after 23500 cycles and thus limited the influence of degradation processes connected to the bond coat oxidation. The thermally-induced mismatch stresses became the major lifetime-limiting factor for thermal barrier coatings (TBCs). Thus, thermal cycling promotes delamination crack path in the TBC whereas high temperature exposure led to the shift of the final failure crack path towards the TGO.

The combination of both thermal cycling and HT exposure load components in cyclic oxidation tests with 2 hours of dwell time at high temperature resulted in the final failure crack path between that for pure cyclic and pure isothermal exposure. However, the lifetime (time at temperature) decreased significantly (by a factor of three) due to the concurrent effect of both bond coat oxidation and damage accumulation by thermally-induced mismatch stresses. It was furthermore shown that the temperature range had a strong influence on lifetime. An increase in the minimum temperature from 60 up to 350°C and thus a decrease in the amount of thermal stresses led to an increase in lifetime by a factor of about two.

Introducing the third load component – temperature gradient – additionally to cyclic oxidation loading, led to a shift of the failure mode into the “white failure” regime (the delamination crack propagates almost completely within the TBC) and a drastic decrease in lifetime (by factor of 10 in comparison to cyclic oxidation). The temperature gradient across the coating of about 100°C (1150°C at the TBC surface, 1050°C at the TBC/BC interface) led to the acceleration of sintering and stiffening processes within the ceramic top coating during high temperature exposure. Thus, sintering is assumed to contribute significantly to a decrease in lifetime.

Under TMF tests (temperature range 350-1050°C, strain range 0.6%), when the mechanical and thermal cyclic load components were superimposed with a phase angle of 180° (out-of-phase (OP) TMF), fatigue damage and the failure of base material typically occurred. During OP TMF, high tensile stresses applied at low temperatures led to earlier crack initiation in the valley region of the TGO/BC interface roughness due to enhanced stresses at those notch-like sites. Fatigue cracks propagated perpendicular to the loading direction into the bond coat and eventually penetrated the substrate, which led to failure of the base material before spallation failure of the TBC.

Activation of BC oxidation related degradation mechanisms by pre-oxidation treatment (for up to 2000 hours at 1050°C) before TMF testing did not cause delamination failure of TBCs before fatigue failure of base material. With an increasing pre-oxidation treatment, the fatigue crack density decreased due to TGO growth and consecutive changes in the interface shape, thus by a reduction in the number of crack initiation sites. However, the cyclic lifetime was

found to decrease by approx. 40% after 300 hours of pre-oxidation and almost 60% after 1000 and 2000 hours.

The application of a high temperature exposure time (2 hours at 1050°C) as dwell time in the TMF cycle led to delamination failure of the TBC before fatigue failure of the base material. The failure crack path was located partly within the TGO and partly in the TBC, similar to the damage after a cyclic oxidation test, whereas the lifetime decreased by approx. 60% compared to cyclic oxidation. Moreover, the lifetime of TBC systems under TMF with HT dwell time was strongly dependent on the total strain amplitude and the cycle shape. A decrease in the strain range to 0.3% led to an increase in lifetime by a factor of about 2.5, which was then similar to cyclic oxidation lifetime in the same temperature range. For in-phase TMF loading, when the thermal and mechanical strains were applied without a phase shift, an additional slight decrease in the lifetime was observed compared to out-of-phase loading.

Fatigue crack growth under TMF loading was found to be controlled by both oxidation and fatigue related processes. During OP TMF, crack growth occurred under the low temperature part of the cycle, when the BC saw tensile stresses. For TMF with limited exposure at high temperature cracks formed at the BC/TBC interface then penetrated the two-phase BC, where they tended to form oxidation fingers towards β-phase particles (directed oxidation). The oxidation fingers were cracked during cooling (branching) and due to dissipating energy, the crack growth in the two-phase BC was decelerated by the presence of β-phase. For TMF with high temperature dwell time, the activation of interdiffusion processes between the BC and base material led to γ′-phase particles formation within the interdiffusion zone, which also caused crack stopping.

TBC deformation properties were systematically determined at high temperatures (950-1150°C) as well as at room temperature using free-standing plasma-sprayed TBCs manufactured as thin-walled hollow cylindrical specimen. Constant compressive load (creep) tests revealed high primary deformation rates in the high temperature range 950-1150°C. The fracture strain at high temperatures was between 1.5 and 3% total compression strain. Between 2 and 3%, the deformation rate revealed only a weak strain dependency, perhaps indicating a subsequent minimum or steady state. At room temperature, the deformation response after load application also revealed a time dependency. The minimum deformation rates and corresponding stresses together with the results of the constant rate experiments were used to derive a Norton diagram. The minimum deformation rate follows a Norton-type power law for not too high stresses at 1050 and 1150°C (stress exponent was 4.0 and 3.5, respectively) and then the power-law broke down at stresses above 200-300MPa.

The effect of permanent compressive strain on macroscopic stiffness was additionally investigated. Compressive deformation in the temperature range of 950-1150°C led to a large increase in stiffness. It increased by a factor of almost five at 2.8% permanent compressive

strain at 1150°C in comparison to value of about 25 GPa for the as-sprayed condition. The effect was greater than after annealing without mechanical loading. The microstructural observations, particularly the closure of microcracks, could provide an explanation for the increase in stiffness.

The observations of microstructural changes revealed that the plasma-sprayed TBC assimilates macroscopic deformation at room temperature partly by closure of inter- and intra-splat microcracks, which are oriented perpendicular to the applied load direction. After high temperature deformation (1150°C), smaller intra-splat cracks were almost completely closed and healed. Moreover, a reduction in the number of grains was observed within splats. However, the shape of the creep curves (rate vs compression strain) suggests the existence of a steady state deformation in the temperature range of 1050-1150°C above 3% total compressive strain, which necessarily involves a weakening mechanism and not only crack closure processes. Observation of the grain structure within one splat after creep deformation showed growth of larger grains, shrinking of smaller grains and coagulation of neighbouring grains, as well as changes in their shapes.

7 References

1. http://www.eia.doe.gov/oiaf/forecasting.html
2. Miller, R.A., Thermal barrier coatings for aircraft engines – history and directions, in: Thermal Barrier Coating Workshop, NASA 3312, 17-34, 1995
3. Singheiser, L., Steinbrech, R., Quadakkers, W.J., Clemens, D., Siebert, B.: Thermal barrier coatings for gas turbine applications – failure mechanisms and life prediction, in: Materials for Advanced Power Engineering 1998, Vol. 5, Part II, 977-996, 1998
4. Stöver, D., Funke, C.: Directions of the development of thermal barrier coatings in energy applications, Journal of Materials Processing Technology, 92-93, 195-202, 1999
5. Beele, W., Marijnissen, G., van Lieshout, A.: The evolution of thermal barrier coatings– status and upcoming solutions for today´s key issues, Surface and Coating Technology, 39-40, 173-181, 1998
6. Padture, N.P., Gell, M., Jordan, E.H.: Thermal barrier coatings for gas-turbine engine applications, Science, 296, 2002, 280-284
7. Vaßen, R., Ahrens, M., Waheed, A.F., Stöver, D.: The influence of the microstructure of thermal barrier coatings systems on sintering and other properties, in: E.L. Lugscheider, C.C. Berndt (Eds.), Proceedings of International Thermal Spray Conference, Essen, Germany, 2002, DVS, Germany, 2002, p. 879
8. Funke, C., Siebert, B., Vaßen, R., Stöver, D.: The influence of plasma spraying parameters on the microstructure and the properties of ZrO_2 – 7wt.% Y_2O_3 thermal barrier coatings, Euromat 97; 1997
9. Rigney, D.V., Viguie, R., Wortmann, D.J., Shelly, D.W.: PVD thermal barrier coatings application and process development for aircraft engines, J. of Thermal Spray Techn., 6, 1997, 167-175
10. Guo, H.B., Vaßen, R., Stöver, D.: Thermophysical properties and thermal cycling behavior of plasma-sprayed thick thermal barrier coatings, Surface and Coatings Technology, 192, 48-56, 2005
11. Schwingel, D., Taylor, R., Haubold, T., Wigren, J., Gualko, C.: Mechanical and thermophysical properties of thick PYSZ thermal barrier coatings: correlation with microstructure and spraying parameters, Surface and Coatings Technology, 108-109, 1998, 99-106
12. Scott, G.: Phase relationships in the zirconia-yttria system, Journal of Materials Science, 10, 1975, 1527-1535
13. Ilavsky, J., Stalick, J.K.: Phase composition and its changes during annealing of plasma-sprayed YSZ, Surface and Coatings Technology, 127, 120-129, 2000
14. Steinbrech, R.: private communication.
15. Allen, A.J., Ilavsky, J., Long, G.G., Wallace, J.S., Berndt, C.C., Herman, H.: Microstructural characterization of yttria-stabilized zirconia plasma sprayed deposits using multiple small-angle neutron scattering, Acta mater., 49, 2001, 1661-1675

16. Steinbrech, R.: Thermomechanical behaviour of plasma sprayed thermal barrier coatings, Ceramic Engineering and Science Proceedings, 26th International Conference on Advanced Ceramics and Composites, Volume 23, Issue 4, 2002, p. 397-407
17. Alaya, M., Oberacker, R., Hoffmann, M.J., Krebs, R., Koch, R., Wittig, S.: Thermophysikalische Eigenschaften von CeO_2- und Y_2O_3 stabilisierten ZrO_2 Wärmedämmschichtsystemen und ihre Auswirkungen auf das thermozyklische Verhalten und den Strahlungsübergang; Werkstoffwoche '96, Symposium 3: Werkstoffe für die Energietechnik, Hrsg: Grünling, H.W.; 1996
18. Fredin, C.: Versagen von Plasmaspritzschichten aus Y_2O_3-stabilisiertem ZrO_2 zur Wärmedämmung im Motor unter Thermoschockbeanspruchung; Tech.wiss. Ber. MPA Stuttgart ; 1993; Heft 93/03
19. Mannsmann, W.: Keramische Wärmedämmschichtsysteme: Eigenschaften und Verhalten unter mechanischer, thermischer und thermomechanischer Beanspruchung; Dissertation; Universität Karlsruhe; 1995
20. Steffens, H.-D.: Herstellen dicker Wärmedämmschichten aus ZrO2 7Y2O3 mit optimierter Lebensdauer, Forschungsbericht des SFB 3156, Teilprojekt A3, Universität Dortmund, 1994, 423-451
21. Cruse, T.A., Johnsen, B.P., Nagy, A.: Mechanical Properties Testing and Results for Thermal Barrier Coatings; Journal of Thermal Spray Technology; 1997; Vol. 6 (1); 57-66
22. Wallace, J.S., Ilavsky, J.: Elastic modulus measurements in plasma sprayed deposits, Journal of Thermal Spray Technology; 1998; Vol. 7 (4); 521-526
23. Singh, J.P., Sutaria, M., Ferber, M.: Use of indentation technique to measure elastic modulus of plasma-sprayed zirconia thermal barrier coating; Ceramic engineering & science proceedings; 1997; Vol. 18 (4); 191-200
24. Pajares, A., Wei, L., Lawn, B.R., Padture, N.P., Berndt, C.C.: Mechanical characterization of plasma sprayed ceramic coatings on metal substrates by contact testing, Mat. Sci. Eng., A208, 1996, 158-165
25. DeMasi, J.T., Sheffler, K.D., Oritz, M.: Thermal barrier coating life prediction developement, Phase I, Final Report; NASA Contractor Report 182230; 1989
26. Beghini, M., Bertini, L., Frendo, F., Giorni, E.: Determination of thermal sprayed coatings elastic modulus using four point bending test; in: Surface Treatment III: Computer Methods & Experimental Measurements; 1997; Hrsg.: Aliabadi, M.H.; Brebbia, C.A.
27. Blandin, G.: Therrmomechanisches Verhalten von plasmagespritzten Schichtsystemen zur Wärmedämmung, Dissertation; RWTH Aachen; 2001
28. Thompson, J.A., Ji, W., Klocker, T., Clyne, T.W.: Sintering of the top coat in thermal spray TBC systems under service conditions; Superalloys 2000; Hrsg.: Pollock, et al.
29. Thurn, G.: Hochtemperatureigenschaften und Schädigungsverhalten plasmagespritzter ZrO_2-Wärmebarrieren; Dissertation; Universität Stuttgart; 1997
30. Allen, A.J., Long, G. G., Boukari, H., Ilavsky, J., Kulkarni, A., Sampath, S., Herman, H., Goland A. N.: Microstructural characterization studies to relate the properties of thermal-

spray coatings to feedstock and spray conditions, Surface and Coatings Technology, 146-147, 9/10, 2001, 544-552

31. Eaton, H.E.; Novak, R.C.: Sintering studies of plasma-sprayed zirconia; Surface and Coatings Technology; 1987; Vol. 32; 227-236
32. Basu, D.; Funke, C.; Steinbrech, R.W.: Effect of heat treatment on elastic properties of separated thermal barrier coatings; J. Mater. Res.; 1999; Vol. 14 (12); 4643-4650
33. Thompson, J.A., T. Clyne, T.W.: The effect of heat treatment on the stiffness of zirconia top coats in plasma-sprayed TBCs, Acta Mater., 49, 2001, 1565-1575
34. Thurn, G., Schneider, G.A., Aldinger, F.: High-temperature deformation of plasma-sprayed ZrO_2 thermal barrier coatings, Mat. Sci. Eng., A233, 1997, 176-182
35. Thurn, G., Schneider, G., Bahr, H-A., Aldinger, F.: Toughness anisotropy and damage behavior of plasma sprayed ZrO_2 thermal barrier coatings, Surface and Coatings Technology, 123, 147-158, 2000
36. Wesling, K.F., Darrell, F.S.: Fatigue of thick thermal barrier coatings, J. Am. Ceram. Soc., 77 (4), 1994, 1863-1868
37. Heckmann, S.: Ermittlung des Verformungs- und Schädigungsverhaltens von Wärmedämmschichtsystemen, Dissertation; RWTH Aachen; 2003
38. Quadakkers, W.J., Tyagi, A.K., Clemens, D., Anton, R., Singheiser, L.: The significance of bond coat oxidation for the life of TBC coatings, in: Elevated temperature coatings: Science and technology III, 119-130, 1999
39. Wright, I.G., Pint, B., Haynes, A.: Factors affecting the performance of bond coatings, TURBOMAT, 2002
40. Christensen, R.J., Tolpygo, V.K., Clarke, D.R.: The influence of the reactive element yttrium on the stress in alumina scales formed by oxidation, Acta mater., 45, No.4, 1761-1766, 1997
41. Gudmundsson, B., Jacobson, B.E.: Structure Formation and Interdiffusion in Vacuum Plasma Sprayed CoNiCrAlY Coatings on IN738LC, Materials Science and Engineering; 1988; Vol. 100; 207-217
42. Kowalewski, R.: Thermomechanische Ermüdung einer beschichteten, stengelkristallinen Nickelbasis-Superlegierung; Fortschr. Ber.; VDI Reihe 18; Nr. 212; 1997
43. Kerkhoff, G.:Vergleich zwischen experimentell beobachteten Versagensmustern und berechneten Spannungsverteilungen in thermisch belasteten ebenen und gekrümmten 8YSZ Wärmedämmschichten, Jül-3784, Forschungszentrum Jülich, 2000
44. Kirchner, H.: Mechanisches Verhalten des Schutzschicht-Grundwerkstoff-Verbundes von Gasturbinenschaufeln unter zyklischer Beanspruchung; Dissertation, TU Darmstadt; 1995
45. Meetham, G.W.: Use of protective coatings in aero gas turbine engines, Mat. Sci. technol. 2, 1986, 290-294
46. Hebsur, M.G.; Miner, R.V.: High Temperature Tensile and Creep Behaviour of Low Pressure Plasma-sprayed Ni-Co-Cr-Al-Y Coating Alloy; Materials Science and Engineering; 1986; Vol. 83; 239-245

47. Smith, R.W.: Mechanical properties of a low-pressure-plasma-applied Co-Cr-Al-Y coating; Thin Solid Films; 1981; Vol. 84; 59-72
48. Majerus, P.: Neue Verfahren zur Analyse des Verformungs- und Schädigungsverhaltens von MCrAlY-Schichten im Wärmedämmschichtsystem, Dissertation, RWTH Aachen, 2003
49. Brindley, W.J., Whittenberger, J.D.: Stress relaxation of low pressure plasma-sprayed NiCrAlY alloys, Materials Science and Engineering A163, 1993, 33-41
50. Metallurgy, Processing, and Properties of Superalloys, in ASM Speciality Handbook: Heat-Resistant Materials, ed. by J.R. Davis, 1997, 591
51. Bullough, C.K., Toulios, M., Oehl, M., Lukas, P.: The characterization of the single crystal superalloy CMSX-4 for industrial gas turbine blading applications, in: Materials for Advanced Power Engineering 1998, Vol. 5, Part II, 861-879
52. Schubert, F., Fleury, G., Stienhaus, T.: Modelling of the mechanical behaviour of the single-crystal turbine alloy CMSX-4 during thermomechanical loading, Modelling Simul. Mater. Sci. Eng. 8, 2000, 947-95
53. Fahrmann, M., Hermann, W., Fahrmann, E., Boegli, A., Pollock, T.M., Sockel, H.G.: Determination of matrix and precipitate elastic constants in (γ-γ′) Ni-base model alloys, and their relevance to rafting, Mater. Sci. Eng. A260, 1999, 212-221
54. Sengupta, A., Putatunda, S.K., Bartosiewicz, L., Hangas, J., Nailos, P.J., Peputapeck, M., Alberts, F.E.: Tensile behavior of a new single crystal nickel-based superalloy (CMSX-4) at room and elevated temperatures, J. Mater. Eng. Perf., 3 (5), 1994, 664-672
55. Beardmore, P., Davies, R.G., Johnston, T.L.: On the temperature dependence of the flow stresses of Nickel-base alloys, Trans. AIME, 245, 1969, 1537-1545
56. Sass, V., Glatzel, U., Feller-Kniepmeier, M.: Creep anisotropy in the monocrystalline nickel-base superalloy CMSX-4, Superalloys, 283-290, 1996
57. Fleury, E., Remy, L.: Low cycle fatigue damage in nickel-base superalloy single crystals at elevated temperature, Mater. Sci. Eng. A167, 1993, 23-30
58. Evans, A.G., Mumm D.R., Hutchinson, J.W., Meier, G.H., Pettit F.S.: Mechanisms controlling the durability of thermal barrier coatings, Progress in Material Science, 46, 505-553, 2001
59. Wright, P.K., Evans, A.G.: Mechanisms governing the performance of thermal barrier coatings, Current Opinion in Solid State and Materials Science, 4, 1999, 255-265
60. Haynes, J.A., Rigney E.D., Ferber, M.K., Porter, W.D.: Oxidation and degradation of a plasma-sprayed thermal barrier coating system, Surface and Coatings Technology, 86-87, 1996, 102-108
61. Tzimas, E., Müllejans, H., Peteves, S.D., Bressers, J., Stamm, W.: Failure of thermal barrier coating systems under cyclic thermomechanical loading, Acta mater., 48, 4699-4707, 2000
62. Schütze, M.: Protective oxide scales and their breakdown, ed. by D.R. Holmes, published by John Wiley&Son

63. Rabiei, A., Evans, A.G.: Failure mechanisms associated with the thermally grown oxide in plasma-sprayed thermal barrier coatings, Acta mater., 48, 3963-3976, 2000
64. Quadakkers, W.J.: Lecture course, Introduction to Oxidation of Alloys
65. Brandl, W., Grabke, H. J., Toma, D., Krüger, J.: The oxidation behaviour of sprayed MCrAlY coatings, Surface and Coatings Technology, 86-87, 1996, 41-47
66. Giggins, C.S., Pettit, F.S.: Oxidation of Ni-Cr-Al alloys between 1000 and 1200°C, Solid State Science, 118, 1971, 1782-1790
67. Shillington, E.A.G., Clarke D.R.: Spallation failure of a thermal barrier coating associated with aluminium depletion in the bond coat, Acta mater., 47, No.4, 1297-1305, 1999
68. Wagner, C.: Beitrag zur Theorie des Anlaufsvorganges, Zeitschrift für Physicalische Chemie, Abt.B., Band 21, Heft 1/2, 1933, 25-41
69. Clemens, D., Quadakkers, W.J., Schubert, F., Nickel, H.: Einfluß von Si and Ti auf das Oxidationsverhalten von McrAlY-Legierungen, Report Forschungszentrum Jülich, Jül-3444, ISSN 0944-2952, 1997
70. Anton, R.: Untersuchungen zu den Versagensmechanismen von Wärmedämmschicht-Systemen im Temperaturbereich von 900°C bis 1050°C bei zyklischer Temperaturbelastung; Dissertation; 2002; RWTH Aachen
71. Clarke, D.R., Sergo, V., He, M.-Y.: Precursor to TBC failure by constrained phase transformation in the thermally grown oxide, in: Elevated temperature coatings: Science and technology III, 1999, 67-78
72. Wang, J.C., Evans, A.G.: Effects of strain cycling on buckling, cracking and spallation of a thermally grown alumina on a nickel-based bond coat, Acta mater., 47, No.2, 699-710, 1999
73. Zhu, D.; Miller, R.A: Sintering and creep behavior of plasma-sprayed zirconia- and hafnia-based thermal barrier coatings. Surface and Coatings Technology, 108-109; 1998, 114-120
74. Vaßen, R., Czech, N., Mallener, W., Stamm, W., Stöver, D.: Influence of impurity content and porosity of plasma-sprayed yttria-stabilized zirconia layers on the sintering behaviour, Surface and Coatings Technology, 141, 135-140, 2001
75. Siebert, B., Funke, C., Vaßen, R., Stöver, D.: Changes in porosity and Young's modulus due to sintering of plasma sprayed thermal barrier coatings, J. Mat. Proc. Tech., 92-93, 1999, 217-223
76. Kaden, U., Leyens, C., Peters, M., Kaysser, W.A.: Thermal stability of an EB-PVD thermal barrier coating system on a single crystal Nickel-base superalloy, in: Elevated temperature coatings: Science and technology III, 1999, 27-38
77. Pint, B.A., Wright, I.G., Lee, W.Y., Zhang, Y., Prüßner, K., Alexander, K.B.: Substrate and bond coat compositions: factors affecting alumina scale adhesion, Mat. Sci. Eng., A245, 201-211, 1998
78. Czech, N., Schmitz, F., Stamm, W.: Microstructural analysis of the role of rhenium in advanced McrAlY coatings, Surface and Coatings Technology, 76-77, 1995, 28-33

79. Zhang, Y.H., Knowles, D.M., Withers, P.J.: Microstructural development in Pt-aluminide coating on CMSX-4 superalloy during TMF, Surface and Coatings Technology, 107, 1998, 114-120
80. Pessahsimonetti, M., Caron, P., Khan, T.: Effect of a long-term prior aging on the tensile behaviour of a high-performance single crystal superalloy, J.Phys., 3, 1993, 347-350
81. Nychka, J.A., Xu, T., Clarke, D.R., Evans, A.G.: The stresses and distortions caused by formation of a thermally grown alumina: comparison between measurements and simulations, Acta mater., 52, 2561-2568, 1997
82. Wright, P.K.: Influence of cyclic strain on life of a PVD TBC, Mat. Sci. Eng., A245, 191-200, 1998
83. Rejda, E.F., Socie, D.F., Beardsley, B.: Fatigue behavior of a plasma-sprayed 8%Y_2O_3-ZrO_2 thermal barrier coating, Fatigue Fract. Engng. Mater. Struct., 20, No.7, 1997, 1043-1050
84. Wood, M.I.: Mechanical interactions between coatings and superalloys under conditions of fatigue; Surface and Coatings Technology; 1989; Vol. 39-40; 29-42
85. Itoh, Y., Saitoh, M., Ishiwata, Y.: Influence of high-temperature protective coatings on the mechanical properties of nickel-based superalloys; Journal of Materials Science; 1999; Vol. 346; 3957-3966
86. Gayda, J., Gabb, T.B., Miner, R.V.: Low cycle fatigue behaviour of a plasma-sprayed coating material; Int J Fatigue; 1986; Vol. 8 (4); 217-223
87. Zhu, D., Miller, R.A.: Investigation of thermal high cycle and low cycle fatigue mechanisms of thick thermal barrier coatings; Materials Science and Engineering, A245; 212-223, 1998
88. Chataigner, E., Remy, L.: Thermomechanical fatigue behaviour of coated and bare Nickel-based superalloy single crystals, in: Thermomechanical Fatigue Behaviour of Materials, Second volume, 1997
89. Kraft, A.S., Mughrabi, H.: Thermo-mechanical fatigue behaviour of the monocrystalline Nickel-base superalloy CMSX-6, in: Thermomechanical Fatigue Behaviour of Materials, Second volume, 1997
90. Zhang, Y.H., Withers, P.J., Fox, M.D., Knowles, D.M.: Damage mechanisms of coated systems under thermomechanical fatigue, Materials Science and Technology, 15, 1031-1036, 1999
91. Tzimas, E., Müllejans, H., Peteves, S.D., Bressers, J., Stamm, W.: Failure of thermal barrier coating systems under cyclic thermomechanical loading, Acta mater., 48, 4699-4707, 2000
92. Baufeld, B., Tzimas, E., Hähner, P., Müllejans, H., Peteves, Moretto, P.: Phase-angle effects on damage mechanisms of thermal barrier coatings under thermomechanical fatigue, Scripta Materialia, 45, 859-865, 2001
93. Heinecke, B., Scholz, A, Berger, C.: Thermomechanical experiments and microstructural observation of thermal barrier coatings, TURBOMAT, 2002

94. DeMasi, J.T., Sheffler, K.D., Oritz, M.: Thermal barrier coating live Prediction Developement, Phase I, Final Report; NASA Contractor Report 182230; 1989
95. Miller, R.A.: Oxidation-based model for thermal barrier coating life; J. Amer. Ceram. Soc., Vol. 767, 1984, 517-521
96. , Schlichting, K. W., Padture, N. P., Jordan, E.H., Gell, M.: Failure modes in plasma-sprayed thermal barrier coatings, Materials Science & Engineering, Elsevier, 2003, pp. 120-130
97. Herzog, R.; Heckmann, S.; Steinbrech, R.W.; Sebold, D.; Quadakkers, W.J.; Schubert, F.; Singheiser, L.; Echsler, H.; Schütze, M.: Contribution to Life Prediction of Thermal Barrier Coatings: A Concept of Accumulated Damage; Proceedings of Materials Week 2001; 2001
98. Chang, G.C., Phucharoen, W., Miller, M.: Behaviour of thermal barrier coatings for advanced gas turbine blades, Surface and Coatings Technology, 30, 1987, p.13-28
99. Freborg, A. M., Ferguson, B.L., Brindley, W.J., Petrus, G.J.: Modeling oxidation induced stresses in thermal barrier coatings, Material science & Engineering A, Elsevier, 1998, 182-190
100. Vassen, R., Kerkhoff, G., Stoever, D.: Development of a micromechanical life prediction modelfor plasma sprayed thermal barrier coatings, Materials Science & Engineering A3 03, Elsevier, 1985, 100-109
101. Renusch, D., Echsler, H., Schütze, M.: Progress in Life Time Modeling of APS-TBC Part I: Residual, Thermal and Growth Stresses Including the Role of Thermal Fatigue; eingereicht bei: Materials Science and Engineering; 2002
102. Renusch, D., Echsler, H., Schütze, M.: Progress in Life Time Modeling of APS-TBC Part II: Critical Strains, Macro-cracking and Thermal Fatigue; eingereicht bei: Materials Science and Engineering; 2002
103. Roesler, J., Backer M., Volgmann, M.: Stress state and failure mechanisms of thermal barrier coatings: role of creep in thermally grown oxide, Acta Materialia, 2001, 3659-3670
104. Roesler, J., Backer, M., Aufzug, K.: A parametric study of the stress state of thermal barrier coatings Part I: creep relaxation, Acta Materialia, 2004, 4809-4817
105. Bednarz, P., Herzog, R., Trunova, E., S., Steinbrech, R.W., Echsler, H., Quadakkers, W.J., Schubert, F., Singheiser, L.: Stress distribution in APS-TBCs under thermal cycling loading conditions, Ceramic Engineering and Science Proceedings, 29th International Conference on Advanced Ceramics and Composites, Volume 26, Issue 3, 2005, p. 73-80
106. Sergo, V., Clarke, D.R.: Observation of subcritical spall propagation of a thermal barrier coating, J. Am. Ceram. Soc., 81, No.12, 1998, 3237-3242
107. Voyer, V.; Gitzhofer, F.; Boulos, M.I.: Study of the Performance of TBC under Thermal Cycling Conditions using an Acoustic Emission Rig; Journal of Thermal Spray Technology; 1998; Vol. 7 (2); 181-190

108. Voyer, V.; Gitzhofer, F.; Boulos, M.I., Durham, S.: Thermally Induced Acoustic Emission in Thermal Barrier Coatings; Proceedings of the 8th National Thermal Spray Conference; 1995; Houston, TX, USA
109. Echsler, H., Shemet, V., Schütze, M., Singheiser, L., Quadakkers, W.J.: Cracking in and around the thermally grown oxide in thermal barrier coatings: a comparison of isothermal and cyclic oxidation, J. Mater. Sci., to be published.

Acknowledgments

First of all, I would like to express my sincere gratitude to my advisors, Prof. Dr. L. Singheiser and Dr. R. Herzog, for making my doctoral research possible, and for their continued support, guidance and encouragement during these last three years.
I would also like to thank all my colleagues from the “Neue Halle” group, especially Mr. B. Werner and Mr. H. Reiners for their technical assistance and support during the experimental part of my research. I would like to give special thanks to Prof. Dr. Schubert and Dr. R.W. Steinbrech for fruitful discussions. Thanks are also due to the metallography lab, including Mr. V. Gutzeit, Mr. J. Bartsch and Mrs. M. Felden, for their patience and guidance during the microstructural analysis. For his assistance, patience, and long evenings spent working SEM, I would like to thank Dr. E. Wessel.
I wish to thank all my friends for their friendship, support, and encouragement.
Last, but not least, thanks to my family for their permanent support and understanding throughout the preparation of this work.

Lebenslauf

Persönliche Daten:

Name:	Olena Trunova
Geboren am:	16.12.1973 in Kiew, Ukraine
Staatsangehörigkeit:	ukrainisch
Familienstand:	verheiratet

Schulausbildung:

09/1980-06/1990	Mittelschule Nr. 185 in Kiew

Studium:

09/1991-02/1997	Pulvermetallurgie an der Nationalen Technischen Universität der Ukraine „KPI“, Kiew, Universitätsabschluss mit Auszeichnung
09/1996-02/1997	Diplomarbeit am Institute für Probleme der Werkstoffkunde der Nationalen Akademie der Wissenschaften der Ukraine, Kiew

Berufspraxis:

1997-2002	Wissenschaftliche Mitarbeiterin am Institute für Probleme der Werkstoffkunde der Nationalen Akademie der Wissenschaften der Ukraine, Kiew
05/2001-01/2002	Aufenthalt am LTm, IUT, in Le Creusot, Frankreich
02/2002-07/2002	Aufenthalt am ENISE, in St.-Etienne, Frankreich
seit 08/2002	Wissenschaftliche Mitarbeiterin am Institut für Werkstoffe und Verfahren der Energietechnik (IWV-2) des Forschungszentrums Jülich GmbH